

INVESTIGATION OF HIGH PERFORMANCE MULTICOLOR  
QUANTUM WELL INFRARED PHOTODETECTORS AND  
4 X 4 THREE-COLOR FOCAL PLANE ARRAY FOR  
MID- AND LONG-WAVELENGTH APPLICATIONS

BY

JUNG HEE LEE

A DISSERTATION PRESENTED TO THE GRADUATE SCHOOL  
OF THE UNIVERSITY OF FLORIDA IN PARTIAL FULFILLMENT  
OF THE REQUIREMENTS FOR THE DEGREE OF  
DOCTOR OF PHILOSOPHY

UNIVERSITY OF FLORIDA

2000

## ACKNOWLEDGMENTS

I wish to express my deepest gratitude to my advisor and the chairman of my committee, Dr. Sheng S. Li, for his guidance, patience, encouragement, and support of my research efforts. I would also like to thank Dr. Gijs Bosman, Dr. Arnost Neugroschel, and Dr. Timothy J. Anderson for serving on my supervisory committee.

I am very grateful to Drs. Jung-Chi Chiang, Jerome Chu, and Xudong Jiang for their assistance and valuable discussion in device fabrication and design. Special thanks are extended to my laboratory colleagues, Chia-Hua Huang, Junhee Moon, Lin Jiang, Jiyon Song, and Seung-Hwan Kim for their friendship and support in semiconductor processing and measurements.

I am greatly indebted to my father, my parents-in-law, my wife, my dear son, and my dear daughter for their emotional support, understanding, and unconditional love during all the years of my life. Last, but not least, I cordially thank my late mother for her devotion and endless love.

Finally, the financial support of ARPA, US Air Force Material Command, and Advanced Device Technology, INC. is gratefully acknowledged.

## TABLE OF CONTENTS

	Page
ACKNOWLEDGMENTS .....	ii
TABLE OF CONTENTS.....	iii
ABSTRACT.....	v
1       INTRODUCTION .....	1
2       THEORETICAL STUDY ON QUANTUM WELL INFRARED PHOTODETECTOR (QWIP) .....	10
2.1 Introduction.....	10
2.2 Calculation of Energy States in Quantum Well and Superlattice .....	11
2.3 Transfer Matrix Method (TMM) for the Transmission Coefficient .....	13
2.4 Strain Effect on the Band Structure of QWIP.....	14
2.5 Absorption Coefficient on Intersubband Transition in Quantum Wells .....	16
2.6 QWIP Figures of Merit .....	19
3       A THREE-STACK INGAAS/ALGAAS/INGAAS BROADBAND TRIPLE-COUPLED QUANTUM WELL INFRARED PHOTODETECTOR..	26
3.1 Introduction.....	26
3.2 Device Design and Fabrication.....	27
3.3 Results and Discussion .....	28
3.4 Conclusions.....	30
4       AN INGAAS/INALAS/INGAAS TRIPLE-COUPLED QUANTUM WELL INFRARED PHOTODETECTOR FOR MWIR DETECTION .....	37
4.1 Introduction.....	37
4.2 Device Design and Fabrication.....	38
4.3 Results and Discussion .....	39
4.4 Conclusions.....	40

5	AN ALAS/INGAAS/ALAS/INALAS DOUBLE-BARRIER QUANTUM WELL INFRARED PHOTODETECTOR OPERATING AT 205K AND 3.4 $\mu$ m.....	47
	5.1 Introduction.....	47
	5.2 Device Design and Fabrication .....	48
	5.3 Results and Discussion .....	49
	5.4 Conclusions.....	51
6	QUANTUM WELL INFRARED PHOTODETECTORS WITH DIGITAL GRADED SUPERLATTICE BARRIER FOR LONG WAVELENGTH AND BROADBAND DETECTION .....	58
	6.1 Introduction.....	58
	6.2 Device Design and Fabrication .....	59
	6.3 Results and Discussion .....	62
	6.4 Conclusions.....	65
7	HIGH SENSITIVITY QUANTUM WELL INFRARED PHOTODETECTORS WITH LINEAR GRADED BARRIER .....	74
	7.1 Introduction.....	74
	7.2 Device Design and Fabrication .....	75
	7.3 Results and Discussion .....	77
	7.4 Conclusions.....	80
8	THREE-COLOR THREE-STACK QUANTUM WELL INFRARED PHOTODETECTORS 4 x 4 FOCAL PLANE ARRAYS.....	92
	8.1 Introduction.....	92
	8.2 Device Design and Fabrication .....	93
	8.3 Results and Discussion .....	96
	8.3.1 LW/LW/MW QWIP 4 x 4 FPA .....	97
	8.3.2 LW/MW/SW QWIP 4 x 4 FPA .....	98
	8.4 Conclusions.....	100
9	SUMMARY AND CONCLUSIONS .....	123
	REFERENCES .....	130
	BIOGRAPHICAL SKETCH .....	137

Abstract of Dissertation Presented to the Graduate School  
of the University of Florida in Partial Fulfillment of the  
Requirements for the Degree of Doctor of Philosophy

INVESTIGATION OF HIGH PERFORMANCE MULTICOLOR  
QUANTUM WELL INFRARED PHOTODETECTORS AND  
4 X 4 THREE-COLOR FOCAL PLANE ARRAY FOR  
MID- AND LONG-WAVELENGTH APPLICATIONS

By

Jung Hee Lee

December 2000

Chairman: Sheng S. Li

Major Department: Electrical and Computer Engineering

In this work, several novel high performance n-type quantum well infrared photodetectors (QWIPs) and two three-color, three-stack QWIP 4 x 4 focal plane arrays (FPAs) have been developed for 1-3  $\mu\text{m}$  short-wavelength infrared (SWIR), 3-5  $\mu\text{m}$  mid-wavelength infrared (MWIR), and 8-14  $\mu\text{m}$  long-wavelength infrared (LWIR) detection. Multi-color, high-sensitivity, and broadband detection have been achieved by using different QWIP device structures and material systems.

The first QWIP for LWIR detection is a high performance broadband InGaAs/AlGaAs/InGaAs triple-coupled (TC-) QWIP grown on semi-insulating (SI) GaAs substrate. The full-width half-maximum (FWHM) of this QWIP was two times larger than that of the normal QWIP structure. The second QWIP was a new MWIR TC-QWIP using lattice-matched  $\text{In}_{0.53}\text{Ga}_{0.47}\text{As}/\text{In}_{0.52}\text{Al}_{0.48}\text{As}/\text{In}_{0.3}\text{Ga}_{0.7}\text{As}$  material systems grown on InP substrate for 3-5  $\mu\text{m}$  detection with operating temperature up to 116K. The

third QWIP structure was a new dual-mode (PV and PC mode) n-type AlAs/InGaAs/AlAs/InAlAs double-barrier (DB-) QWIP grown on InP substrate with peak detection wavelength at 3.4  $\mu\text{m}$  and operating temperature up to 205K for mid-wavelength infrared (MWIR) detection.

The fourth QWIP devices were two novel high performance InGaAs/AlGaAs/GaAs QWIPs using digital graded superlattice barrier (DGSLB) grown on the GaAs substrates. These new structures enable the broadband detection (54 ~ 62 %) and significantly improve the device performance under positive bias operation. The fifth QWIPs were a high performance QWIP using InGaAs/AlGaAs linear graded barrier (LGB) QWIP structure for the broadband (BB-) detection (6.5 ~ 16  $\mu\text{m}$ ) and a high-sensitivity AlGaAs/InGaAs/AlGaAs double-barrier (DB-) LGB QWIP with peak responsivity of 4.38 A/W at 9.1  $\mu\text{m}$  and 35K.

Finally, two three-color, three-stack QWIP 4 x 4 focal plane arrays (FPAs) with a pixel size of 100 x 100  $\mu\text{m}^2$  were fabricated and characterized for the first time. Each stack can detect unique peak so that three-color detection can be obtained through the three-stack structure. These two FPAs were designed to detect the LW/LW/MW and LW/MW/SW regimes, respectively. The excellent multi-color detection with three identical peaks was successfully achieved.

## CHAPTER 1 INTRODUCTION

Since a physical object emits its energy into infrared (IR) spectrum radiation under nature's normal environment, the IR radiation detectors are most useful devices to observe the motions of the lives, the objects, and the surroundings without light. The IR spectrum can be divided into short-wavelength infrared (SWIR, 1-3  $\mu\text{m}$ ), mid-wavelength infrared (MWIR, 3-5  $\mu\text{m}$ ), long-wavelength infrared (LWIR, 8-14  $\mu\text{m}$ ), and very long-wavelength (VLWIR,  $>14 \mu\text{m}$ ). The IR detectors can be grouped into two-type [1]: thermal-type and photon-type. The thermal-type detectors are called uncooled thermal detectors because most thermal detectors do not require the cryogenic cooling system while liquid helium, liquid nitrogen or thermo-electric cooler are needed to operate the photon-type detectors. Three different thermal detectors have been studied, which are the bolometer, the pyroelectric, and the thermopile. These thermal detectors can observe changes in some physical property such as the temperature increase and the electrical resistance by the heating effect due to the absorption of the incident IR radiation, and usually respond equally to all wavelengths. However, the time constant of a thermal detector is not short enough so that the applications are significantly limited. For photon detectors, the spectral response results from the direct interaction between photons and carriers in material. The response time of the photon detectors is very short and sensitivity is one or two orders higher than thermal detectors.

A wide variety of detector materials such as HgCdTe, InSb, InGaAs, and PtSi have been used to detect desirable optical absorption, which have various band gap energies ( $E_g$ ). In general, IR detectors require very high quality material to improve the device performance. Therefore, the detector materials should keep stability, uniformity, and high operability. The detection wavelength regions of IR detectors using interband transition rely on the bandgaps of the detector materials so that the detection wavelength flexibility will be largely compromised.

In recent years, quantum well infrared photodetectors (QWIPs) have been developed for MWIR and LWIR detection. The quantum well (QW) can be formed due to the conduction or the valence band offset when a smaller band gap material was grown between two larger band gap materials. The quantized energy levels are formed inside the quantum well so that the infrared radiation can be detected due to the optical transitions from the ground state to the upper excited states. The quantum well must be doped with donor (i.e., n-type QWIP) and the electrons, which occupied the ground state of the quantum well by doping, can be photoexcited to an unoccupied excited state to generate photocurrent for IR radiation detection. The separation of energy levels in the quantum well can be varied by changing the well thickness and the mole fractions of the quantum well and barrier. Therefore, the detection wavelength of QWIP is comparatively not dependent on the device material but rather the layer structure. The rapid progress of the III-V material device growth technique such as molecular beam epitaxy (MBE) [2] and metalorganic chemical vapor deposition (MOCVD) has extensively encouraged the development of a number of QWIP devices. The QWIP has a lot of advantages: high uniformity, high yield, low cost, wavelength flexibility, multicolor capability, radiation

hardness, low 1/f noise, and large size staring arrays. Although the photovoltaic (PV) mode IR detector under zero bias is attractive for some applications due to the low dark current, low power dissipation, excellent noise property, and fast integration time for focal plane array (FPA), the photoconductive (PC) mode under biased operation is still practical because the responsivity of the PC mode detector is much higher than the PV mode operation.

Since West and Eglash [3] first observed the strong optical intersubband transition in GaAs/AlGaAs multi quantum well (MQW) and Levine *et al.* [4] demonstrated the first GaAs QWIP, various intersubband transition schemes and material systems have been widely studied. For example, bound-to-bound (BTB) [4], bound-to-quasi-bound (BTQB) [5], bound-to-miniband (BTM) [6], and bound-to-continuum (BTC) [7] transition schemes were chosen to improve the device performance in the past ten years. Figures 1.1 and 1.2 show the schematic energy band diagram for n-type and p-type QWIPs, respectively. The p-type QWIPs can allow the normal incident IR detection due to the linear combination of p-like valence Bloch states without the grating coupler [8,9]. However, the n-type QWIP is more interesting than the p-type QWIP because the performance of the n-type QWIP is much better and the grating coupler is no longer an issue due to the advanced processing technology.

The multi-color detection for the MWIR and LWIR dual band detection is more important to determine thermal feature on a target object because the absolute temperature can be uniquely determined by the ratio of radiance measured at the two-wavelength band. Therefore, the multiple wavelength IR detector can improve the device performance including better discrimination and tracking. This multi-color detection can

be obtained by several structures, which are the multi-stack structure with one MWIR stack and one LWIR stack [10,11], asymmetrical QWIP structure for voltage tunability, and QWIP structure with two occupied energy levels [12]. Figure 1.3 shows the different structures for multi-color detection.

The excellent QWIP performance makes it possible to develop the large area, high sensitive, high-speed, and low cost QWIP staring focal plane arrays (FPAs) which are useful in some practical applications: the remote sensing of earth/atmosphere, infrared astronomy, night vision, tracking, medical thermal imaging, temperature measurement, and weather watch [13]. Until recently, 128 x 128, 256 x 256, and 640 x 480 FPAs [14-17] have been demonstrated with higher uniformity and higher yield and a 1024 x 1024 format FPA is possible at the present time. In addition, the multi-color QWIP FPA for MWIR and LWIR dual band detection has been successfully demonstrated. Readout circuitry is needed to transfer signals from the detector pixels to the output of the chip. The Si-CMOS MUX is usually hybridized to the QWIP FPA for the imaging camera. The readout integrated circuit (ROIC) with high-resolution and low-noise for all QWIP FPA technologies is necessary to convert the photoresponse efficiently into digital form for signal processing. Development of multi-color QWIP with high performance is of prime interest for FPAs and other image applications.

In chapter 2, we will describe the basic principles of the quantum well infrared photodetectors, which include the calculation of the energy levels in the quantum well and superlattice, the strain effect on bandstructure, the transfer matrix method (TMM) for the calculation of the transmission coefficient, the absorption coefficient on the

intersubband transition in the quantum wells, and the QWIP figures of merit for device performance characterization.

Chapter 3 will give a demonstration of an InGaAs/AlGaAs/InGaAs broadband (BB) triple-coupled (TC-) QWIP for voltage tunable multicolor detection in the LWIR region. This BB TC-QWIP was formed by using a three-stack structure without contact layers between the stacks in which each stack has a different period to appropriately distribute the applied bias.

Chapter 4 will report a new MWIR triple-coupled quantum well infrared photodetector (TC-QWIP) using an  $\text{In}_{0.53}\text{Ga}_{0.47}\text{As}/\text{In}_{0.52}\text{Al}_{0.48}\text{As}/\text{In}_{0.3}\text{Ga}_{0.7}\text{As}$  material system grown on InP substrate for 3-5  $\mu\text{m}$  detection. The peak wavelengths for this device were  $\lambda_{p1} = 4.6 \mu\text{m}$  and  $\lambda_{p2} = 3.7 \mu\text{m}$ , which were due to the BTB and BTC transitions, respectively.

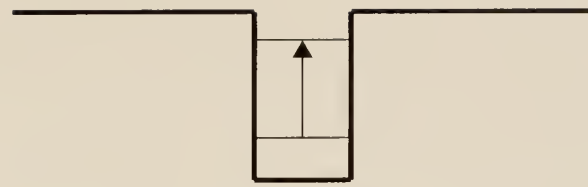
Chapter 5 will show the characterization of a new dual-mode (i.e., PV and PC mode) operation *n*-type AlAs/InGaAs/AlAs/InAlAs double-barrier (DB-) QWIP with peak detection wavelength at 3.4  $\mu\text{m}$  for mid-wavelength infrared (MWIR) detection. This device can be operated up to 205K with excellent performance.

In chapter 6, we first report two novel high performance InGaAs/AlGaAs/GaAs QWIPs using a digital graded superlattice barrier (DGSLB) to achieve the staircase-like graded barrier across the barrier region of the QWIP. The broadband detection was achieved under positive bias and the normal photoresponse with very high responsivity was observed under negative bias.

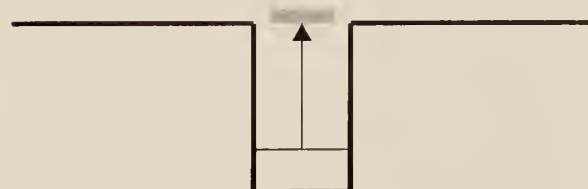
Next, the broadband (BB-) linear graded barrier (LGB) QWIP and the double-barrier (DB-) LGB QWIP are presented in chapter 7. The spectral responsivity was measured at

T = 35, 60, and 77K. The broadband detection was obtained under positive bias conditions in both LGB QWIPs in which the detection wavelength of the BB-LGB QWIP was much broader than the DB-LGB QWIP. Under a negative bias condition, the peak responsivity of the DB-LGB QWIP was found to be as high as 4.38 A/W.

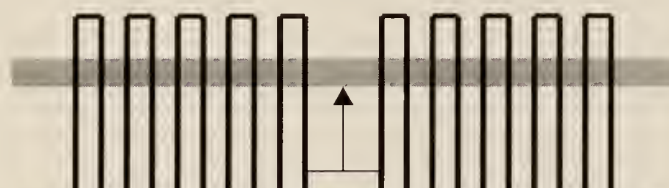
Finally, two 4 x 4 focal plane array (FPA) three-color, three-stack QWIP structures with a pixel size of  $100 \times 100 \mu\text{m}^2$  were grown on a semi-insulating (SI) GaAs substrate in which each stack can cover LWIR, MWIR, or SWIR regime, respectively. These 4 x 4 FPAs consist of three stacks with a buffer layer between the middle-stack and the bottom-stack for multicolor detection. The first FPA (LW/LW/MW) has three distinct peaks of 12, 8.8, and 4.2  $\mu\text{m}$  while the second FPA (LW/MW/SW) is sensitive to three bands with corresponding peaks of 7.9, 3.7, and 2.4  $\mu\text{m}$ , respectively. These devices are demonstrated in chapter 8.



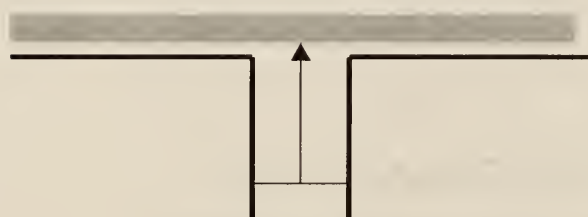
(BTB N-QWIP)



(BTQB N-QWIP)



(BTM N-QWIP)



(BTC N-QWIP)

Figure 1.1. The schematic conduction band diagrams of n-type QWIPs.

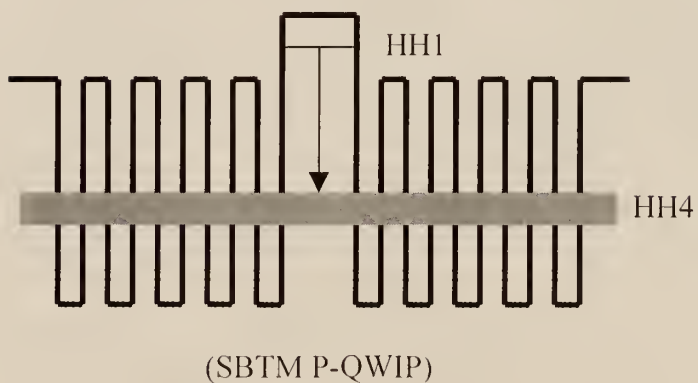
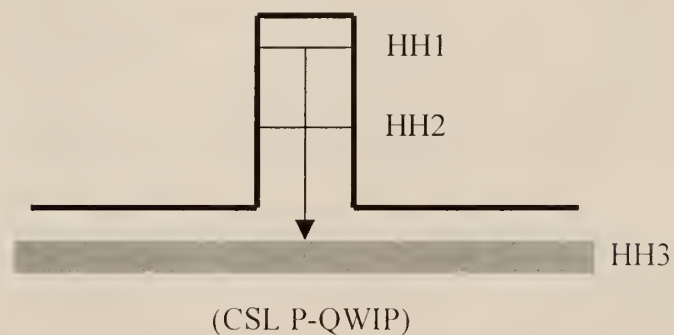
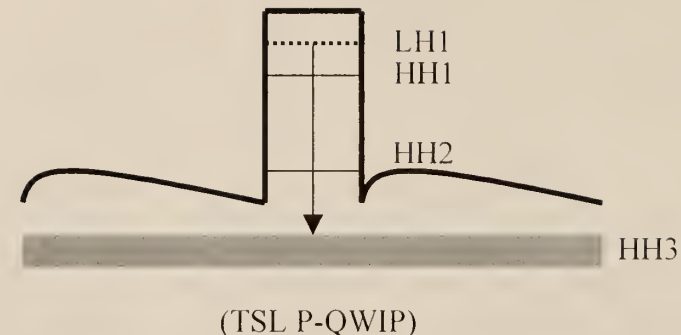
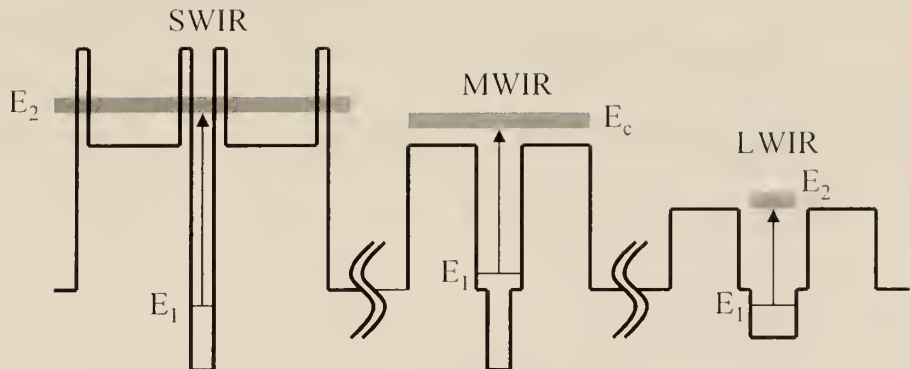
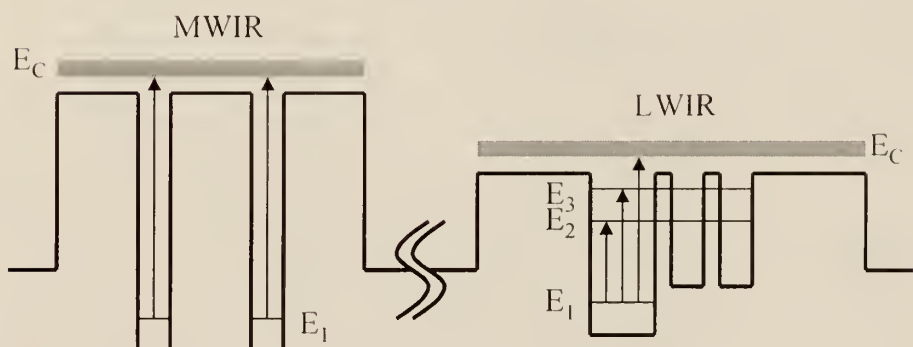


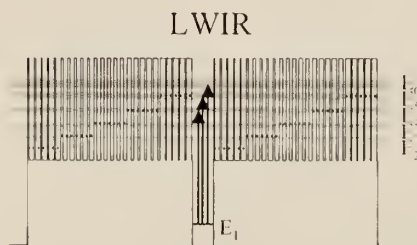
Figure 1.2. The schematic valence band diagrams of p-type QWIPs.



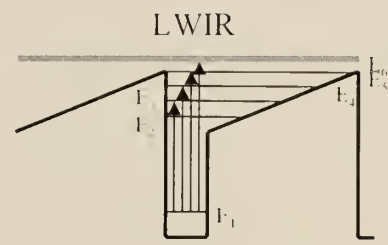
(three-color three-stack DB/BTC/BTQB QWIP)



(two-stack two-color BTC/TC QWIP)



(BB-DGSLB QWIP)



(BB-LGB QWIP)

Figure 1.3. The schematic conduction band diagrams of n-type multicolor QWIPs.

## CHAPTER 2

### THEORETICAL STUDY ON QUANTUM WELL INFRARED PHOTODETECTOR (QWIP)

#### 2.1 Introduction

The quantum well infrared photodetectors (QWIPs) based on intersubband transition are composed of several periods of the doped quantum wells (QWs) and the undoped barriers. The maturity of the QWIP growth technology such as molecular beam epitaxy (MBE) technique make it the rapid progress of QWIPs with high performance in the past decades. Since the first GaAs/AlGaAs QWIP was developed, various QWIP structures with different material systems and transition schemes have been studied. For an optimized QWIP device, the materials, the light coupling scheme, operating temperature, and readout electronics must be significantly considered. The great success in the single QWIPs has led the development of the focal plane array (FPA) and in recent years the large (640 x 480) FPA with high uniformity has been successfully demonstrated [17]. In addition, It is well known that it is important to understand the design and analysis of infrared focal plane array readout circuitry with low-noise and high-resolution. The QWIP (<30 %) has much lower quantum efficiency than HgCdTe ( $\approx$ 60 %). However, the QWIP has a number of advantages on wavelength flexibility, multi-color capability, high uniformity, lower cost and so on. In order to improve the QWIP device performance, it is motivated to understand the basic QWIP detector physics. In this chapter, the fundamental principles on QWIP are described.

## 2.2 Calculation of Energy States in Quantum Well and Superlattice

Using the effective mass approximation, the motion of the electrons in quantum well structure can be written by Schrödinger wave equation as

$$\left[ -\frac{\hbar^2}{2m^*} \nabla^2 + V(z) \right] \Psi = E \Psi, \quad (2.1)$$

where the  $m^*$  is the effective mass,  $V(z)$  is the potential profile along  $z$ -direction, and  $z$  is the growth direction of the QW structure. When the wave function was divided into two components of the  $z$ -direction and  $x-y$  plane, the solution of Schrödinger equation can be simplified as [18]

$$\Psi(x, y, z) = e^{ik_x x} e^{ik_y y} \psi(z), \quad (2.2)$$

By substituting (2.2) into (2.1), and we can get

$$\left[ -\frac{\hbar^2}{2m^*} \frac{\partial^2}{\partial z^2} + V(z) \right] \psi(z) = E \psi(z). \quad (2.3)$$

Here, when we first consider the quantum well structure with infinite barriers, the normalized wave function using the boundary conditions at  $-l/2$  and  $l/2$  with quantum well thickness of  $l$  can be given as

$$\psi(z) = \sqrt{\frac{2}{l}} \cos\left(\frac{n\pi z}{l}\right), \quad n \text{ odd} \quad (2.4)$$

$$= \sqrt{\frac{2}{l}} \sin\left(\frac{n\pi z}{l}\right), \quad n \text{ even} \quad (2.5)$$

For the quantum well structure with finite barrier height ( $V_c$ ), the condition of the allowed bound energy states can be obtained as

$$\alpha \tan\left(\frac{\alpha l}{2}\right) = \beta, \quad (2.6)$$

$$\alpha \cot\left(\frac{\alpha l}{2}\right) = -\beta, \quad (2.7)$$

where

$$\alpha = \sqrt{\frac{2m^* E}{\hbar^2}}, \quad (2.8)$$

$$\beta = \sqrt{\frac{2m^*(V_c - E)}{\hbar^2}}, \quad (2.9)$$

These equations can be solved by numerical technique.

When the quantum wells and thin barriers are alternatively and periodically repeated, it is called superlattice. In a quantum well structure with thick and finite height barriers, the bound states are localized into the quantum well region, which can also be exponentially decayed into the barrier region. Therefore, there is no overlapping of bound state wave functions between the adjacent wells. However, when the barrier thickness is decreased, those bound state wave functions can be overlapped, which results in a miniband. The Kronig-Penney model can be employed to calculate the dispersion relation of the minibands. When the superlattice has a quantum well width of  $a$ , barrier width of  $b$ , barrier height of  $V_c$ , and period of  $d (= a+b)$ , the solution of the Schrödinger equation for this superlattice can be given as a Bloch theorem;

$$\psi(z + d) = e^{ik_z d} \psi(z), \quad (2.10)$$

In a period,

$$\psi(z) = A e^{i\delta z} + B e^{-i\delta z}, \quad \text{in the barrier} \quad (2.11)$$

$$= C e^{i\omega z} + D e^{-i\omega z}, \quad \text{in the well} \quad (2.12)$$

Then, in the following period,

$$\psi(z) = e^{ik_z d} \left[ A e^{i\delta(z-d)} + B e^{-i\delta(z-d)} \right], \text{ in the barrier} \quad (2.13)$$

$$= e^{ik_z d} \left[ C e^{i\alpha(z-d)} + D e^{-i\alpha(z-d)} \right], \text{ in the well} \quad (2.14)$$

where  $\delta$  is  $i\beta$  in which  $\alpha$  and  $\beta$  are shown in (2.8) and (2.9), respectively. A, B, C, and D constants can be obtained by the boundary conditions and the dispersion relations for the bound and unbound states are given as [19]

$$\cos(k_z d) = \cos(a\alpha) \cosh(b\beta) - \frac{\alpha^2 - \beta^2}{2\alpha\beta} \sin(a\alpha) \sinh(b\beta), \text{ for } 0 < E < V_c \quad (2.15)$$

$$= \cos(a\alpha) \cos(b\delta) - \frac{\alpha^2 + \delta^2}{2\alpha\delta} \sin(a\alpha) \sin(b\delta), \text{ for } E > V_c \quad (2.16)$$

Therefore, the minibands can be calculated from the above Eqs. (2.15) and (2.16).

### 2.3 Transfer Matrix Method (TMM) for the Transmission Coefficient

The energy levels and the corresponding wave functions in a multi-quantum well structure can be obtained by different methods [20-23] such as the standard analytical method, Wentzel-Kramers-Brillouin (WKB) approximation, Kronig-Penney model, and the variational principle, which are however not suitable for general purposes. Recently, the transfer matrix method (TMM) [24], which involves the straightforward multiplication of  $2 \times 2$  matrices with no iterations, has been developed to analyze exactly the multi-quantum well structures. When we consider an arbitrary multi-quantum well structure with  $N+1$  layers, the solution of the Schrödinger wave equation can be given as

$$\psi_n = A_n e^{-i\Delta_n z} e^{ik_n z} + B_n e^{i\Delta_n z} e^{-ik_n z}, \quad (2.17)$$

where

$$\Delta_1 = \Delta_2 = 0, \quad (2.18)$$

$$\Delta_n = k_n(d_2 + d_3 + \dots + d_{n-1}), \quad n = 3, 4, 5, \dots, N+1 \quad (2.19)$$

$$k_n = \left[ \frac{2m_n^*}{\hbar^2} (E - V_n) \right]^{1/2}. \quad (2.20)$$

where  $A_n$  and  $B_n$  are the amplitudes of the wave function in  $+z$  and  $-z$  directions, respectively, and  $d_n$ ,  $m_n^*$ , and  $V_n$  are the thickness, the effective mass, and the potential of the  $n^{\text{th}}$  layer, respectively. Applying the boundary conditions at each interface gives as follows

$$\begin{pmatrix} A_1 \\ B_1 \end{pmatrix} = S_1 \begin{pmatrix} A_2 \\ B_2 \end{pmatrix} = S_1 S_2 \begin{pmatrix} A_3 \\ B_3 \end{pmatrix} = \dots = S_1 S_2 \dots S_N \begin{pmatrix} A_{N+1} \\ B_{N+1} \end{pmatrix}, \quad (2.21)$$

where  $N$  is the total number of the layers and

$$S_n = \frac{1}{t_n} \begin{pmatrix} e^{-ik_n d_n} & r_n e^{-ik_n d_n} \\ r_n e^{ik_n d_n} & e^{ik_n d_n} \end{pmatrix}, \quad r_n = \frac{k_n - k_{n+1}}{k_n + k_{n+1}}, \quad t_n = \frac{2k_n}{k_n + k_{n+1}}. \quad (2.22)$$

Here, we can set  $B_{N+1} = 0$  since there is no reflection wave in  $N+1^{\text{th}}$  layer. Therefore, the transmission coefficients can be calculated by  $|A_{n+1}/A_1|^2$  as a function of  $E$  and then each energy states can be obtained.

## 2.4 Strain Effect on the Band Structure of QWIP

In order to grow the strain structure without misfit dislocations, the layer thickness cannot be more than a certain threshold, which is called critical thickness. If the layer thickness exceeds the critical thickness, misfit dislocations are created in the structure. Matthews and Blakeslee expressed the critical layer thickness as [25,26]

$$h_c = \left( \frac{b}{\varepsilon} \right) \frac{1 - \nu \cos^2 \theta}{8\pi(1+\nu)\cos \lambda} \left[ 1 + \ln \left( \frac{d}{b} \right) \right], \quad (2.23)$$

where  $b = a/\sqrt{2}$  and  $a$  is the lattice constant grown on the substrate,  $\theta$  is the angle between the dislocation line and the Burges vector,  $\lambda$  is the angle between the slip direction and the layer plane direction,  $v$  is the Poisson ratio,  $d$  is the layer thickness.  $\varepsilon = (a_2 - a_1)/a_1$  is the biaxial strain parameter in which  $a_1$  and  $a_2$  are the lattice constants of the epilayer and the substrate, respectively. The value of the in-plane lattice constant ( $a_{\parallel}$ ) due to straining is obtained by minimizing the total elastic strain energy of the barrier and the well. The in-plane lattice constant ( $a_{\parallel}$ ) is intermediate between the unstrained lattice constants of the layers, then [26]

$$a_{\parallel} = a_1 \left[ 1 + \varepsilon / \left( 1 + \frac{S_1 d_1}{S_2 d_2} \right) \right], \quad (2.24)$$

where  $S_i$  are the shear moduli,  $d_i$  is the layer thickness, and  $\varepsilon$  is the lattice mismatch between layers. Figure 2.1 (a) shows the unstrained lattice layers having different constants ( $a_2 > a_1$ ) and the strained layers with in-plane lattice constant ( $a_{\parallel}$ ). In an unstrained condition, the heavy and light holes have the same potential and the first heavy hole energy level is always the first valence band level because of the effective mass difference between heavy and light holes. After straining, the splitting of the heavy hole and light hole at the valence band zone center ( $\Gamma$ ) occurs in every band structure; that is, under biaxial compression, the heavy hole band is higher than the light hole band, and the interval between the first heavy and light holes is increased by splitting while the light hole band is pushed to a higher level than that of the heavy hole under biaxial tension. In addition, the conduction band is changed due to the strain in which the conduction band can be moved upward and downward depending on biaxial compression and biaxial tension, respectively. Figure 2.1 (b) shows the energy band shift by strain in

detail. The energy band gaps due to strain for the heavy hole and light hole are given as follows [27]

$$E_{ohh} = E_o + \Delta E_{ohh}, \quad (2.25)$$

$$E_{olh} = E_o + \Delta E_{olh}, \quad (2.26)$$

where  $E_o$  is the unstrained band gap and  $\Delta E_{ohh}$ , and  $\Delta E_{olh}$  are the strained band gap shifts for the heavy hole and light hole, respectively,

$$\Delta E_{ohh} = \left[ 2a\left(\frac{C_{11} - C_{12}}{C_{11}}\right) - b\left(\frac{C_{11} + 2C_{12}}{C_{11}}\right) \right] \varepsilon, \quad (2.27)$$

$$\Delta E_{olh} = \left[ 2a\left(\frac{C_{11} - C_{12}}{C_{11}}\right) + b\left(\frac{C_{11} + 2C_{12}}{C_{11}}\right) - \varepsilon b^2 \left(\frac{C_{11} + 2C_{12}}{C_{11}}\right)^2 / (2\Delta_o) \right] \varepsilon, \quad (2.28)$$

where  $\varepsilon$  can be a negative sign for compressive strain or a positive sign for tensile strain,  $a$  is the hydrostatic deformation potential,  $b$  is the shear deformation,  $\Delta_o$  is the spin-orbit splitting energy, and  $C_{ij}$  is the stiffness coefficient of the material.

When the quantum wells are highly doped, the electrons interact with each other so that the energy level shift due to the many-body effects on quantum well structure can be observed, which are direct Coulomb interaction, electron-electron interaction, electron-phonon interaction and so on [28-33]. Therefore, those effects should be taken into account in calculating the energy levels in the quantum well structure.

## 2.5 Absorption Coefficient on Intersubband Transition in Quantum Wells

The calculation of the energy states and the corresponding peak detection wavelength in a QW structure was described in the previous subsections. In addition, the calculation

of the absorption coefficient on intersubband transition in a QW structure is needed to determine the absorption strength and the absorption lineshape. The absorption coefficient as a function of the photon energy,  $\hbar\omega$ , can be defined as [5]

$$\alpha(\hbar\omega) = \hbar\omega \frac{\text{Net number of transition per unit cell volume and time}}{\text{incident energy flux}}. \quad (2.29)$$

When we consider the intensity of the radiation field ( $I$ ) and the optical intersubband transition rate between the initial and final states ( $W_{fi}$ ), the absorption coefficient can be also given as

$$\alpha(\hbar\omega) = \frac{\hbar\omega W_{fi} (f_f - f_i)}{\Omega I}, \quad (2.30)$$

where  $f_f$  and  $f_i$  are the Fermi-Dirac distribution function for the final and initial energy states, respectively,  $\Omega$  is the volume of the QW, and  $W_{fi}$  can be expressed as [34]

$$W_{fi} = \frac{2\pi}{\hbar} \left| \langle \Psi_f | V_p | \Psi_i \rangle \right|^2 \delta(E_f - E_i - \hbar\omega), \quad (2.31)$$

where  $E_f$  and  $E_i$  are the final and initial energy states, respectively, and  $V_p$  is the interaction potential for the photon absorption, which can be written as [34]

$$V_p = -\frac{e}{m^*} \mathbf{A} \cdot \mathbf{p} = -\frac{e}{m^*} |\mathbf{A}_0| \cos(\mathbf{k} \cdot \mathbf{r} - \omega t) \hat{\varepsilon} \cdot \mathbf{p} \cong -\frac{e}{2m^*} |\mathbf{A}_0| e^{i\mathbf{k} \cdot \mathbf{r} - \omega t} \hat{\varepsilon} \cdot \mathbf{p}, \quad (2.32)$$

where  $\hat{\varepsilon}$  is the polarization vector,  $m^*$  is the effective mass of the electron, and  $\mathbf{p}$  is momentum vector of the electron in the QW. In a simple one-band model, the wave function for a quantum well structure is given as [35]

$$\Psi_n(\mathbf{r}) = \frac{1}{\sqrt{A_d}} e^{i\mathbf{k} \cdot \rho} \psi_n(\varepsilon) u(\mathbf{r}), \quad (2.33)$$

where  $A_d$  is the QW area,  $\mathbf{k} = (k_x, k_y)$  is 2-D in-plane wavevector,  $\rho = (x, y)$  is 2-D

coordinate space vector,  $\mathbf{r} = (\rho, z)$ ,  $u(\mathbf{r})$  is the period part of the Bloch function, and  $\psi_n(z)$  is an envelop function in the growth direction ( $z$ ) for the  $n^{th}$  energy state. Therefore, the transition rate can be rewritten by

$$\begin{aligned} W_{fi} &= \frac{2\pi}{\hbar} \left| \left\langle \Psi_f \left| \frac{e}{2m^*} |\mathbf{A}_0| e^{i\mathbf{k} \cdot \mathbf{r} - \omega t} \hat{\mathbf{e}} \cdot \mathbf{p} \right| \Psi_i \right\rangle \right|^2 \delta(E_f - E_i - \hbar\omega), \\ &\cong \frac{2\pi}{\hbar} \frac{e^2}{4m^{*2}} |\mathbf{A}_0|^2 \left| \left\langle \psi_f \left| -i\hbar \frac{\partial}{\partial z} \right| \psi_i \right\rangle \right|^2 \delta(E_f - E_i - \hbar\omega), \end{aligned} \quad (2.34)$$

where  $\langle \Psi_f | V_p | \Psi_i \rangle \cong \langle \psi_f | V_p | \psi_i \rangle$  for the intersubband case,  $\hat{\mathbf{e}} \cdot \mathbf{p} = p_z = -i\hbar \frac{\partial}{\partial z}$ , and  $e^{i\mathbf{k} \cdot \mathbf{r}} \cong 1$  for the QW scale [5].

The monochromatic radiation field impinging on the QWIP structure can be described by [36]

$$\mathbf{A}(\mathbf{r}, t) = |\mathbf{A}_0| \cos(\mathbf{k} \cdot \mathbf{r} - \omega t), \quad (2.35)$$

where  $\mathbf{A}_0$  is the complex polarization vector and  $\mathbf{k}$  is the wavevector. The electric field,  $\mathbf{E}(\mathbf{r}, t)$ , and the magnetic field,  $\mathbf{B}(\mathbf{r}, t)$ , can be calculated by

$$\mathbf{E}(\mathbf{r}, t) = -\frac{1}{c} \frac{\partial \mathbf{A}(\mathbf{r}, t)}{\partial t} = -\frac{\omega}{c} |\mathbf{A}_0| \sin(\mathbf{k} \cdot \mathbf{r} - \omega t), \quad (2.36)$$

$$\mathbf{B}(\mathbf{r}, t) = \nabla \times \mathbf{A} = -\mathbf{k} \times |\mathbf{A}_0| \sin(\mathbf{k} \cdot \mathbf{r} - \omega t), \quad (2.37)$$

With these two  $\mathbf{E}(\mathbf{r}, t)$  and  $\mathbf{B}(\mathbf{r}, t)$ , the intensity of the radiation field can be described by averaging the Poynting vector ( $\mathbf{S}$ ) as follows

$$I = |\overline{\mathbf{S}}| = \frac{c}{4\pi} |\overline{\mathbf{E} \times \mathbf{B}}| = \frac{n\omega^2 |\mathbf{A}_0|^2}{8\pi c}, \quad (2.38)$$

where  $n$  is the refractive index and  $c$  is the speed of the light.

Finally, by substituting (2.34) and (2.38) into (2.30), the absorption coefficient can be expressed as [37]

$$\begin{aligned}\alpha(\hbar\omega) &= \frac{4\pi^2 e^2}{cn\omega \Omega_{BZ}} \int \frac{2d\mathbf{k}}{(2\pi)^2} M_{fi}^2 (f_f - f_i) \delta(E_f - E_i - \hbar\omega), \\ &\approx \frac{4\pi^2 e^2}{cn\omega} \int_{BZ} \frac{2d\mathbf{k}}{(2\pi)^2} M_{fi}^2 (f_f - f_i) \frac{1}{\pi} \frac{\Gamma/2}{(E_f - E_i - \hbar\omega)^2 + (\Gamma/2)^2},\end{aligned}\quad (2.39)$$

where  $M_{fi} = (-i\hbar/m^*) \langle \psi_f | (\partial/\partial z) \psi_i \rangle$  and  $\Gamma$  is the broadening factor.

## 2.6 QWIP Figures of Merit

In order to design and characterize the QWIP device, the figures of merit such as dark current, spectral responsivity, noise, and detectivity must be highly considered. Moreover, these figures of merit can be controlled by the doping density in QW, the number of QW, and the barrier profile for the optimization of QWIP performance.

It is well known that under a dark condition there are three electron transport mechanisms, which are thermionic emission, thermally assisted tunneling, and direct or trap-assisted tunneling. The thermionic emission due to the electrons transferred out of the quantum wells is dominant at low biases and high temperatures while the thermally generated carriers tunneling through the barriers are more important at high biases and low temperatures. The dark current models for QWIP have been analyzed in the published papers [38-47]. The dark current was calculated by assuming a constant electric field across the QWIP active layer and thermodynamic carrier equilibrium in which the dark current calculation was performed using WKB approximation including image charge effect and it was compared with calculations using the Transfer Matrix

Method (TMM) [41]. The dark current calculation in Liu et al. [42] shows the good agreement with the measured dark current at a range of temperature from 65 to 105K. The dark current of QWIP due to the thermionic emission is given by [48]

$$I_d = A_d e v_d n, \quad (2.40)$$

where  $A_d$  is the detector area,  $e$  is the electronic charge,  $v_d$  is the average drift velocity, and  $n$  is the density of mobile carriers, which can be expressed as

$$v_d = \mu F / [1 + (\mu F / v_s)^2]^{1/2}, \quad (2.41)$$

$$n = (m^* / \pi \hbar^2 L_p) \int_{E_l}^{\infty} f(E) T(E, F) dE, \quad (2.42)$$

where  $\mu$  is the electron mobility,  $F$  is the average electric field,  $v_s$  is the electron saturation velocity,  $m^*$  is the electron effective mass in the QW,  $L_p (=L_w+L_b)$  is the QWIP length, and the  $f(E)$  is the Fermi-factor given by  $f(E) = [1 + \exp(E - E_l - E_F)/kT]^{-1}$ . respectively.  $T(E, F)$  is the bias-dependent tunneling current transmission coefficient for a single barrier and can be obtained by WKB approximation, which is given by [42]

$$T(E, F) = 1, \text{ for } E > E_b - eFL_w, \quad (2.43)$$

$$T(E, F) = \exp \left[ \left( -\frac{4}{3\hbar eF} \right) (2m_b^*)^{1/2} (E_b - E - eFL_w)^{3/2} \right],$$

for  $E_b - eFL_p < E < E_b - eFL_w,$  (2.44)

$$T(E, F) = \exp \left[ \left( -\frac{4}{3\hbar eF} \right) (2m_b^*)^{1/2} \left\{ (E_b - E - eFL_w)^{3/2} - (E_b - E - eFL_p)^{3/2} \right\} \right],$$

for  $E_l < E < E_b - eFL_p,$  (2.45)

where  $L_w$ ,  $L_b$ , and  $m_b^*$  are QW width, barrier thickness, and electron effective mass in the barrier, respectively. Finally, the dark current can be expressed as follows.

$$I_d = \frac{Aem^*}{\pi\hbar^2 L_p} \frac{\mu F}{\sqrt{1 + (\mu F / v_s)^2}} \int_{E_b}^{\infty} f(E) T(E, F) dE. \quad (2.46)$$

For the sake of simplicity, we can assume that  $T(E) = 0$  for  $E < E_b$  and  $T(E) = 1$  for  $E > E_b$ .

Therefore,  $n$  and  $I_d$  can be given by,

$$n = (m^* kT / \pi\hbar^2 L_p) \exp[-E_{ac} / kT], \quad (2.47)$$

$$I_d = A_d \left( \frac{m^* kT}{\pi\hbar^2 L_p} \right) \left( \frac{\mu F}{\left[ 1 + (\mu F / v_s)^2 \right]^{1/2}} \right) \exp\left[ -\frac{E_{ac}}{kT} \right]. \quad (2.48)$$

where  $E_{ac}$  ( $= E_b - E_I - E_F$ ) is the activation energy and  $E_b$ ,  $E_I$ , and  $E_F$  are the barrier energy, the ground state energy, and Fermi energy, respectively. The Fermi energy ( $E_F$ ) can be calculated from

$$N_d = \frac{m^* kT}{\pi\hbar^2 L_w} \ln \left[ 1 + \exp\left( \frac{E_F}{kT} \right) \right]. \quad (2.49)$$

As a result, the dark current ( $I_d$ ) is exponentially related to the doping density and the activation energy ( $E_{ac}$ ) as follows,

$$I_d \propto \exp\left[ \frac{N_d}{kT} \right] \propto \exp\left[ -\frac{E_{ac}}{kT} \right]. \quad (2.50)$$

Therefore, the activation energy ( $E_{ac}$ ) can also be obtained from the slope of the normalized dark current ( $I_d/T$ ) versus the inverse temperature straight line on a semilog scale.

The absolute spectral responsivity ( $R_i$ ) can be given by quantum efficiency ( $\eta$ ) and photoconductive gain ( $g$ ) as [49]

$$R_i = \frac{e\lambda\eta}{hc} g = \frac{e}{hv} \eta_c = \frac{\lambda}{1.24} \eta g, \quad (2.51)$$

where  $e$  is the electronic charge,  $\lambda$  is the wavelength of the incident photon,  $h$  is the Plank constant,  $c$  is the speed of the light,  $v$  is the incident frequency, and  $\eta_c$  is the collection efficiency ( $\eta g$ ). The quantum efficiency ( $\eta$ ) [49] is the average number of optical transitions per each photon incident into the detector and described as  $\eta = (1/2)(1 - R_c)(1 - e^{-m\alpha l})$ , where  $R_c$  is the reflection coefficient,  $m$  is the number of the absorption pass,  $\alpha$  is the absorption coefficient of the QW layers, and  $l$  is the total thickness of the QWIP layer. The photoconductive gain ( $g = v_d \tau / L$ ) can be expressed as the ratio of the electron mean free path ( $v_d \tau$ ) to the QWIP thickness ( $L$ ) or the ratio of photo-generated electron lifetime ( $\tau$ ) to the transit time ( $L/v_d$ ) across the QWIP layer, where  $v_d$  is the drift velocity of the photo-generated electrons. In general, the photoconductive gain ( $g$ ) is not required less than one, which can be more than one when a photo-generated electron can circulate the circuit several times until it is recombined. The spectral responsivity can also be calculated by

$$R_t = \frac{I_p}{P_{in}}, \quad (2.52)$$

where  $I_p$  is the photocurrent output (A), and  $P_{in}$  is the input IR radiation power (W), which can be expressed as

$$I_p = \frac{V_p}{R_f}, \quad (2.53)$$

$$P_{in} = A_d H_{in}, \quad (2.54)$$

where  $V_p$  is the photovoltage of the photodetector,  $R_f$  is the gain of the transimpedance amplifier (TIA),  $A_d$  is the photodetector area ( $\text{cm}^2$ ), and  $H_{in}$  is the input irradiance ( $\text{W/cm}^2$ ), which is given by

$$H_m = \frac{V_{pyro} T_w T_d}{R_p A_p}, \quad (2.55)$$

where  $V_{pyro}$  is the photovoltage of the pyroelectric detector,  $T_w$  is the transmissivity of the entrance window of the cryogenic system,  $T_d$  is the transmissivity of the photodetector,  $R_p$  is the responsivity of the pyroelectric detector (V/W), and  $A_p$  is the active area of the pyroelectric detector ( $\text{cm}^2$ ), respectively. The pyroelectric detector is used to calibrate the input power of the infrared radiation from the blackbody IR source onto the photodetector.

The noise in QWIP devices are due to the fluctuations in the velocity of the carriers and in carrier density, which are called Johnson noise and generation-recombination (*g-r*) noise, respectively, and given as follows [50]

$$\text{Johnson noise : } i_n^2 = \frac{4kT\Delta f}{R}, \quad (2.56)$$

$$\text{g-r noise : } i_n^2 = 4egI_d\Delta f, \quad (2.57)$$

where  $\Delta f$  is noise bandwidth and  $R$  is the resistance of the detector.

Finally, the spectral detectivity ( $D^*$ ) is useful figure of merit in comparing different detectors. The non-BLIP (background limited performance) detectivity,  $D^*$ , can be shown as [49]

$$D^* = R_i \sqrt{\frac{A_d \Delta f}{i_n^2}}, \quad (2.58)$$

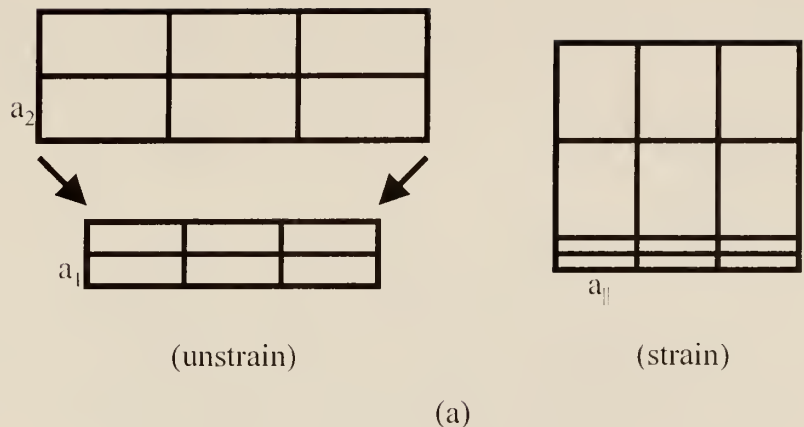
Under BLIP condition, which requires  $I_b$  (background photocurrent detected in QWIP)  $> I_d$ , it is well known that the BLIP detectivity ( $D_{BLIP}^*$ ) is independent of the photoconductive gain and dark current, and it can be expressed as [51]

$$D_{BLIP}^* = \frac{\lambda}{2hc} \left( \frac{\eta_\gamma}{Q_b} \right), \quad (2.59)$$

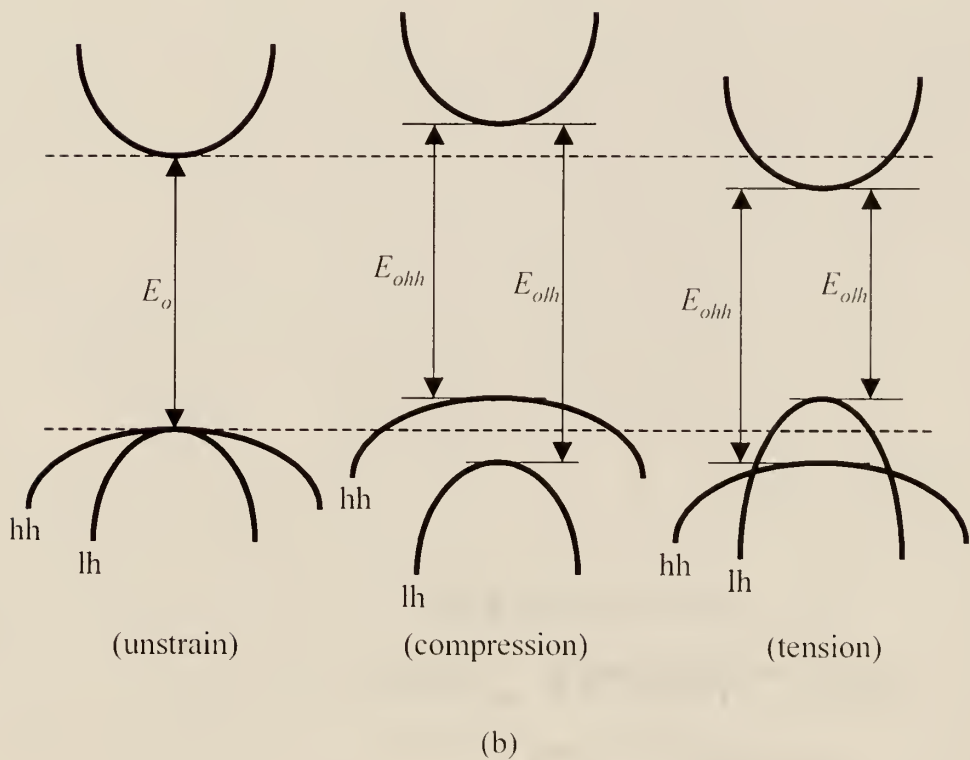
where  $\lambda$  is the wavelength;  $h$  is the Plank constant;  $c$  is the velocity of light;  $\eta_\gamma$  is the net quantum efficiency, and  $Q_b$  is the incident photon flux density from the background for a given spectral bandwidth at peak wavelength, which can be calculated from

$$Q_b = \int_0^{\lambda_c} \frac{2\pi c}{\lambda^4} \frac{1}{e^{hc/\lambda kT_b} - 1} d\lambda, \quad (2.60)$$

where  $\lambda_c$  is the cutoff wavelength,  $k$  is the Boltzmann constant, and  $T_b$  is the background temperature.



(a)



(b)

Figure 2.1. (a) Unstrained and strained two-layer schematic and (b) Energy band gap shifts under strain.

# CHAPTER 3

## A THREE-STACK INGAAS/ALGAAS/INGAAS BROADBAND TRIPLE-COUPLED QUANTUM WELL INFRARED PHOTODETECTOR

### 3.1 Introduction

Multi-color quantum well infrared photodetectors (QWIPs) using different transition schemes and structures have been widely investigated in recent year [12]. Theoretical studies of quantum-confined Stark effect in two- and three-coupled-quantum-well (TCQW) structures have been reported for voltage tunable infrared detection [52,53], and voltage-tunable multicolor triple-coupled QWIPs (TC-QWIPs) using InGaAs/GaAs/AlGaAs and high-strain (HS) InGaAs/AlGaAs/InGaAs material systems grown on GaAs for 8-12  $\mu\text{m}$  long-wavelength detection have been demonstrated recently [54,55]. The high-strain InGaAs/AlGaAs/InGaAs TC-QWIP has shown excellent performance and wavelength tunability in the LWIR spectral range [54]. Most QWIP devices were developed with sensitivity in the 3-5  $\mu\text{m}$  mid-wavelength infrared (MWIR) or 8-12  $\mu\text{m}$  long-wavelength infrared (LWIR) region. The multi-color QWIPs were also investigated by using multi-stack quantum well structure for both the mid-wavelength and long-wavelength detection or voltage tuning of peak wavelength such as TC-QWIP, which usually has narrow bandwidth due to bound-to-bound state transition [54,55]. In order to broaden the detection bandwidth, the bound-to-miniband (BTM) QWIP [56] and asymmetrical quantum well structure with graded barrier [57] were proposed. Recently, several broadband (BB-) QWIPs have been demonstrated using three- or four-well

structure in a unit cell that has different well widths and barrier heights by varying the barrier layer composition [58].

In this chapter, we report a high performance InGaAs/AlGaAs/InGaAs broadband triple-coupled quantum well infrared photodetector (BB TC-QWIP) for voltage tunable multicolor detection in the 7-12  $\mu\text{m}$  long-wavelength band. This BB TC-QWIP was formed by using three-stack structure without contact layers between the stacks.

### 3.2 Device Design and Fabrication

This BB TC-QWIP device was formed by using a three-stack structure without contact layers between the stacks. The device structure of each stack consists of an asymmetrical triple coupled quantum wells (TCQWs) with one deep  $\text{In}_{0.25}\text{Ga}_{0.75}\text{As}$  quantum well Si-doped to  $N_d = 7.0 \times 10^{17} \text{ cm}^{-3}$  and two undoped  $\text{In}_{0.12}\text{Ga}_{0.88}\text{As}$  shallow quantum wells separated by two 20Å thin inner barriers ( $\text{Al}_x\text{Ga}_{1-x}\text{As}$ ) between the 500Å thick barriers ( $\text{Al}_x\text{Ga}_{1-x}\text{As}$ ). Each TC-QWIP stack has different quantum well widths, periods, and barrier heights by varying Al composition so that each stack has different peak detection wavelengths. The different periods were used to evenly distribute the bias voltage drop across each stack, which are 3 periods for the bottom stack, 5 periods for the middle stack, and 6 periods for the top stack, respectively. The quantum well widths and barrier material of the TC-QWIP stacks are given as 55/40/35Å and  $\text{Al}_{0.11}\text{Ga}_{0.89}\text{As}$  for the bottom stack, 55/40/40Å and  $\text{Al}_{0.08}\text{Ga}_{0.92}\text{As}$  for the middle stack, and 50/40/40Å and  $\text{Al}_{0.06}\text{Ga}_{0.94}\text{As}$  for the top stack, respectively. Two 0.1  $\mu\text{m}$  thick undoped GaAs layers were grown on both sides of this TC-QWIP to reduce the dark current. Finally, the TC-QWIP surrounded by the top and bottom ohmic contact layers (Si-doped to  $n = 2.0 \times 10^{18} \text{ cm}^{-3}$ ) was grown on the semi-insulating GaAs substrate. Table 3.1 shows the layer

structure of the stacked TC-QWIP. A mesa structure with  $216 \times 216 \mu\text{m}^2$  active area was fabricated to characterize the device performance by using standard wet chemical etching. AuGe/Ni/Au was evaporated on the top and bottom of the mesa structure for ohmic contacts. The  $45^\circ$  polished facet was processed for the back-illumination and IR radiation coupling. The device was mounted at the edge of the hole on the 16-pin TO-8 socket. The silver-filled epoxy with low thermal resistance was used to bond the device onto the package.

### 3.3 Results and Discussion

Figure 3.1 shows the schematic conduction band diagram and the calculated intersubband transition energy levels of this stacked TC-QWIP at zero bias voltage. Each TC-QWIP stack can detect specific peak wavelength and then the whole three-stack TC-QWIP structure can cover the broad wavelength range by overlapping the detection wavelength of each stack. The  $E_1 \rightarrow E_c$  bound-to-continuum (BTC) transition was mainly detected at lower bias voltages while both  $E_1 \rightarrow E_c$  and  $E_1 \rightarrow E_3$  bound-to-bound (BTB) transitions were observed at higher bias voltages.

Figure 3.2 shows the dark current versus bias voltage (I-V) measured at  $T = 40, 52, 60$ , and  $77\text{K}$  with a  $180^\circ$  field of view (FOV)  $300\text{ K}$  background photocurrent of the device. The dark current curves show the asymmetric behavior due to the asymmetric layer structure and the normal feature of n-type QWIPs. The device is under background limited performance (BLIP) between  $-5.5\text{V}$  and  $4.2\text{V}$  at  $T = 40\text{K}$ , and between  $-1.8\text{V}$  and  $1.2\text{V}$  at  $T = 77\text{K}$ .

The photo response was measured at  $T = 40$  and  $77\text{K}$  by using a  $1/8$  monochromator and blackbody light source ( $T = 1273\text{K}$ ) at a chopped frequency (200 Hz). Figure 3.3

shows the spectral responsivity of the TC-QWIP at  $T = 40\text{K}$ , (a) lower bias, and (b) higher bias voltages. The applied bias voltage was first distributed across the bottom TC-QWIP because of the highest resistance by the highest barrier. When the applied bias voltage was further increased the middle stack and the top stack can be biased one after another. As clearly shown in Fig. 3.3, only  $E_1 \rightarrow E_c$  transitions of the bottom and middle stacks were observed at lower bias voltages ( $V_b \leq -3.75\text{V}$ ). The  $E_1 \rightarrow E_c$  transition of the top stack can also be observed with the increasing bias voltage ( $V_b \geq -4\text{V}$ ). The peak responsivity and full-width half-maximum (FWHM) at  $\lambda_p = 8.7 \mu\text{m}$  and  $V_b = -3.75\text{V}$  were  $0.48 \text{ A/W}$  and  $\Delta\lambda/\lambda_p = 21 \%$ , respectively. When a higher bias voltage ( $V_b \geq -4\text{V}$ ) was applied to the device, the thick AlGaAs barrier was tilted to the thin triangle barrier so that the  $E_1 \rightarrow E_3$  transitions can be detected by the tunneling through  $E_3$  bound state. At the bias voltage of  $-4.5\text{V}$ , the spectral responsivities at  $\lambda_{p1} = 8.4 \mu\text{m}$  and  $\lambda_{p2} = 10.8 \mu\text{m}$  were almost the same ( $0.82 \text{ A/W}$  and  $0.81 \text{ A/W}$ , respectively). Therefore, a very broad responsivity curve was achieved with  $\Delta\lambda/\lambda_{p1} = 21 \%$  and  $\Delta\lambda/\lambda_{p2} = 20 \%$  for this stacked TC-QWIP. It is noted that this  $\Delta\lambda/\lambda_{p2} = 20 \%$  is much broader than that of the one stack high-strain TC-QWIP ( $\Delta\lambda/\lambda_p = 10 \%$ ). The  $E_1 \rightarrow E_3$  transition becomes the dominant response peak at  $V_b = -4.75\text{V}$ . In particular, the peak spectral responsivity at  $\lambda_p = 10.6 \mu\text{m}$  and  $V_b = -5.2\text{V}$ , which was primarily due to the  $E_1 \rightarrow E_3$  transition of the bottom stack, was found to be  $2.75 \text{ A/W}$ . The tunable wavelength for  $E_1 \rightarrow E_3$  transition was  $10.6\text{-}10.8 \mu\text{m}$  between  $-5.2\text{V}$  and  $-4.75\text{V}$ . Figure 3.4 shows the measured and the calculated  $300\text{K}$  background window current I-V curves with  $180^\circ$  field of view (FOV), which was in good agreement with each other. Figure 3.5 shows the spectral responsivity of the BB TC-QWIP measured at  $T = 77\text{K}$  and different bias voltages. The peak

responsivity at  $T = 77\text{K}$  and  $V_b = -4.25\text{V}$  was  $0.62 \text{ A/W}$  at  $\lambda_p = 10.3 \mu\text{m}$ . The  $T = 40\text{K}$  and  $77\text{K}$  spectral responsivity curves were different at the same bias voltage. For example, the  $E_1 \rightarrow E_3$  transition at  $V_b = -4.25\text{V}$  and  $T = 77\text{K}$  was more dominant than that at  $T = 40\text{K}$ , that is, the spectral responsivity by  $E_1 \rightarrow E_3$  transition was larger than that of  $E_1 \rightarrow E_c$  transition at  $T = 77\text{K}$ , but this was reversed at  $T = 40\text{K}$ , which was attributed to the more dominant thermionic-assisted tunneling (TAT) conduction through  $E_3$  bound state at higher temperature.

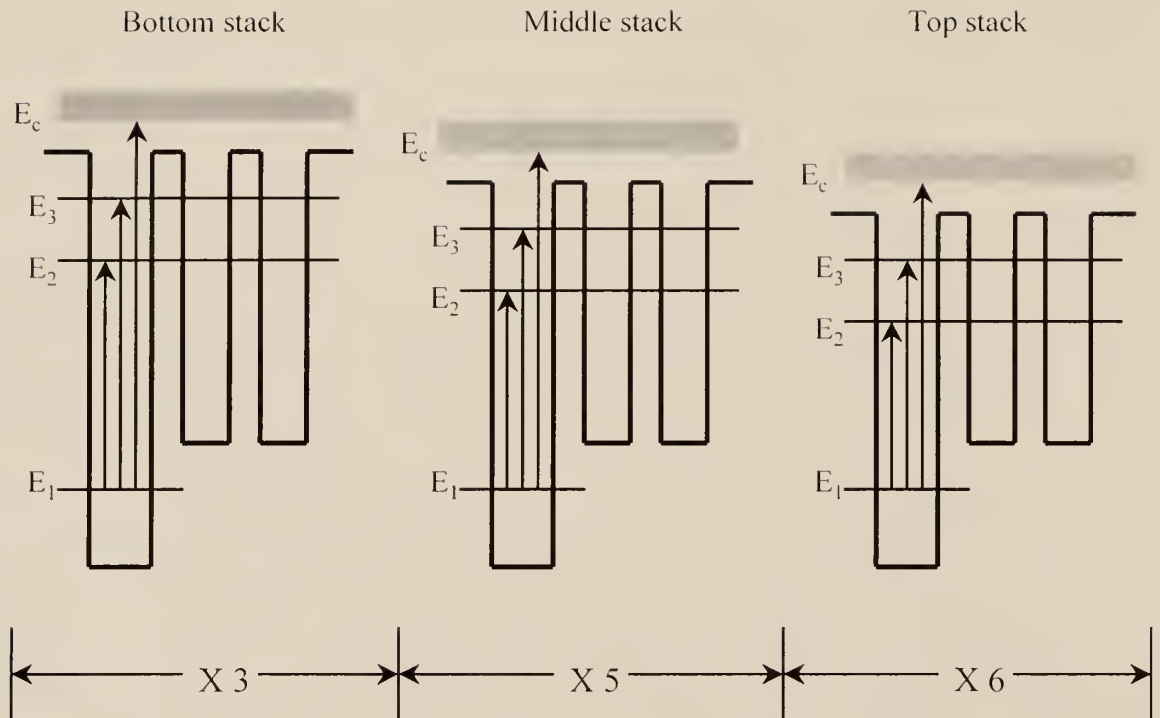
We have calculated the detectivity for the BB TC-QWIP at  $T = 40\text{K}$  and  $77\text{K}$  by using our noise model. The background limited performance (BLIP) detectivity ( $D^*_{\text{BLIP}}$ ) at  $\lambda_p = 10.6 \mu\text{m}$  was found to be  $1.98 \times 10^{10} \text{ cm-Hz}^{1/2}/\text{W}$  at  $T = 40\text{K}$  and  $V_b = -5.2\text{V}$ . The peak detectivity ( $D^*$ ) under non-BLIP condition was  $5.54 \times 10^9 \text{ cm-Hz}^{1/2}/\text{W}$  at  $T = 77\text{K}$ ,  $\lambda_p = 10.3 \mu\text{m}$ , and  $V_b = -4.25\text{V}$ .

### 3.4 Conclusions

We have fabricated and characterized a new InGaAs/AlGaAs/InGaAs broadband triple-coupled quantum well infrared photodetector (BB TC-QWIP) for  $8\text{-}14 \mu\text{m}$  long-wavelength detection. In order to detect the broad wavelength range, the three-stack structure that has three different peak wavelengths was created as a three-color QWIP. The  $E_1 \rightarrow E_c$  transition was obtained at lower bias voltages ( $V_b < -3.75\text{V}$ ) and both  $E_1 \rightarrow E_3$  and  $E_1 \rightarrow E_c$  transitions were detected simultaneously at higher bias voltages ( $V_b \geq -4\text{V}$ ). The broader wavelength range can be detected by modifying the layer structure. The positive temperature dependence of the responsivity was found from the measured results at  $T = 40$  and  $77\text{K}$ .

Table 3.1. The layer structure of the BB TC-QWIP.

Layer	Thickness (Å)	Dopant	Concentration (cm <sup>-3</sup> )
n GaAs (top contact)	5000	Si	2x10 <sup>18</sup>
i GaAs	1000	none	none
i Al <sub>0.06</sub> Ga <sub>0.94</sub> As	500	none	none
i In <sub>0.12</sub> Ga <sub>0.88</sub> As	X 6	40	none
i Al <sub>0.06</sub> Ga <sub>0.94</sub> As		20	none
i In <sub>0.12</sub> Ga <sub>0.88</sub> As		40	none
i Al <sub>0.06</sub> Ga <sub>0.94</sub> As		20	none
n In <sub>0.25</sub> Ga <sub>0.75</sub> As		50	Si
i Al <sub>0.06</sub> Ga <sub>0.94</sub> As		500	none
i In <sub>0.12</sub> Ga <sub>0.88</sub> As	X 5	40	none
i Al <sub>0.08</sub> Ga <sub>0.92</sub> As		20	none
i In <sub>0.12</sub> Ga <sub>0.88</sub> As		40	none
i Al <sub>0.08</sub> Ga <sub>0.92</sub> As		20	none
n In <sub>0.25</sub> Ga <sub>0.75</sub> As		55	Si
i Al <sub>0.08</sub> Ga <sub>0.92</sub> As		500	none
i In <sub>0.12</sub> Ga <sub>0.88</sub> As	X 3	35	none
i Al <sub>0.11</sub> Ga <sub>0.89</sub> As		20	none
i In <sub>0.12</sub> Ga <sub>0.88</sub> As		40	none
i Al <sub>0.11</sub> Ga <sub>0.89</sub> As		20	none
n In <sub>0.25</sub> Ga <sub>0.75</sub> As		55	Si
i Al <sub>0.11</sub> Ga <sub>0.89</sub> As		500	none
i GaAs	1000	none	none
n GaAs (bottom contact)	10000	Si	2x10 <sup>18</sup>
S.I. GaAs substrate	625 ± 25 μm	none	none



Bottom stack ( $\text{In}_{0.25}\text{Ga}_{0.75}\text{As}/\text{Al}_{0.11}\text{Ga}_{0.89}\text{As}/\text{In}_{0.12}\text{Ga}_{0.88}\text{As}$ )

Middle stack ( $\text{In}_{0.25}\text{Ga}_{0.75}\text{As}/\text{Al}_{0.08}\text{Ga}_{0.92}\text{As}/\text{In}_{0.12}\text{Ga}_{0.88}\text{As}$ )

Top stack ( $\text{In}_{0.25}\text{Ga}_{0.75}\text{As}/\text{Al}_{0.06}\text{Ga}_{0.94}\text{As}/\text{In}_{0.12}\text{Ga}_{0.88}\text{As}$ )

< intersubband transition energy at zero bias voltage >

Bottom stack :  $E_1 - E_c$  ( 140 meV ),  $E_1 - E_3$  ( 114 meV )

Middle stack :  $E_1 - E_c$  ( 123 meV ),  $E_1 - E_3$  ( 104 meV )

Top stack :  $E_1 - E_c$  ( 106 meV ),  $E_1 - E_3$  ( 98 meV )

Figure 3.1. The schematic conduction band diagram and the intersubband transition energy of the BB TC-QWIP.

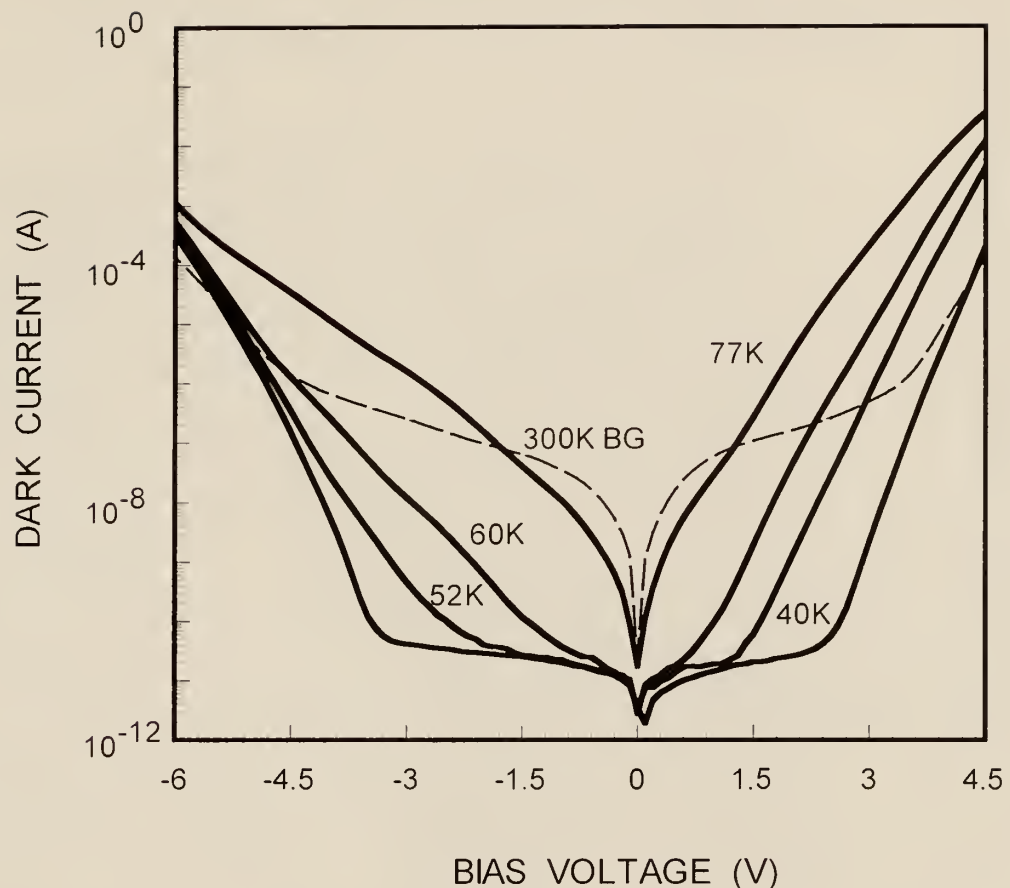


Figure 3.2. The dark current versus bias voltage (I-V) measured at  $T = 40, 52, 60$  and  $77\text{K}$  with the  $180^\circ$  field of view (FOV)  $300\text{K}$  background window current of the BB TC-QWIP.

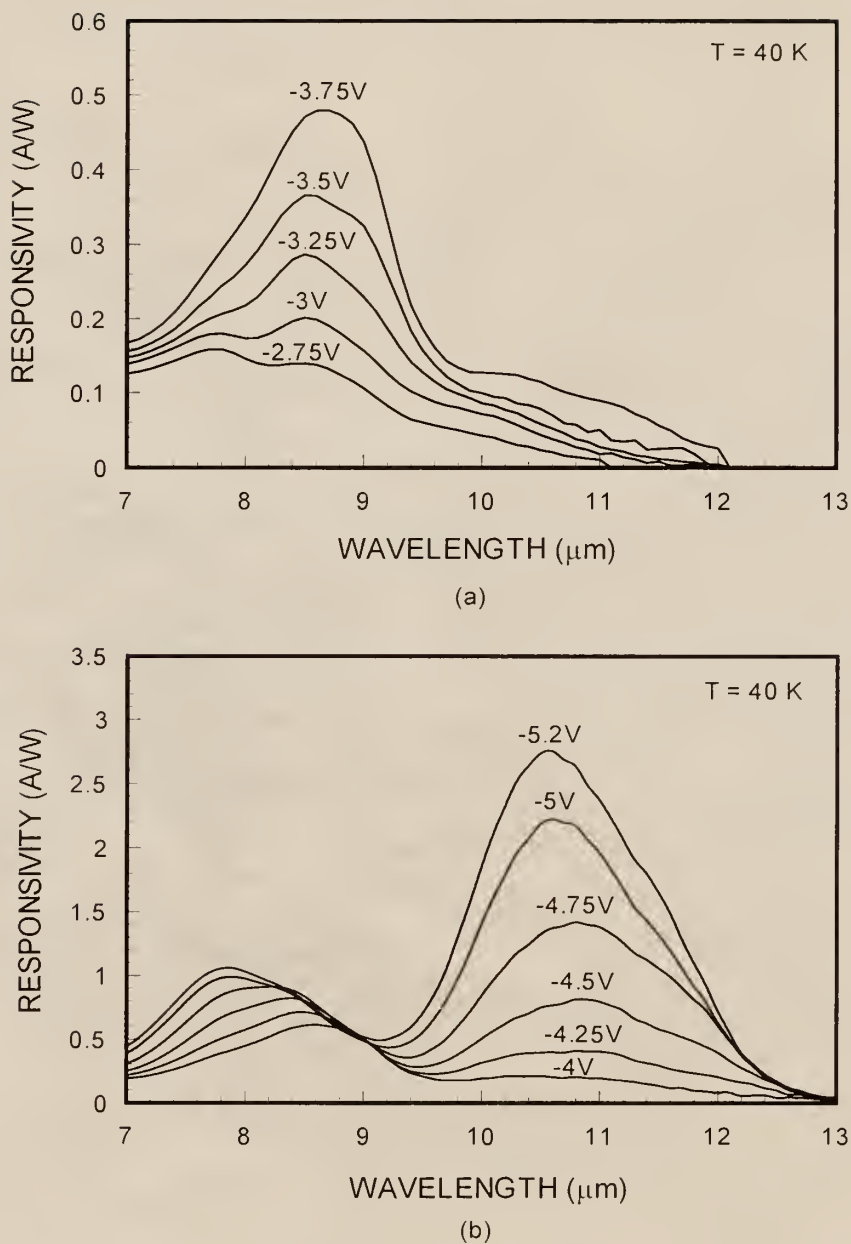


Figure 3.3. The spectral responsivity of the BB TC-QWIP measured at  $T = 40\text{K}$ : (a) lower bias voltage and (b) higher bias voltage.

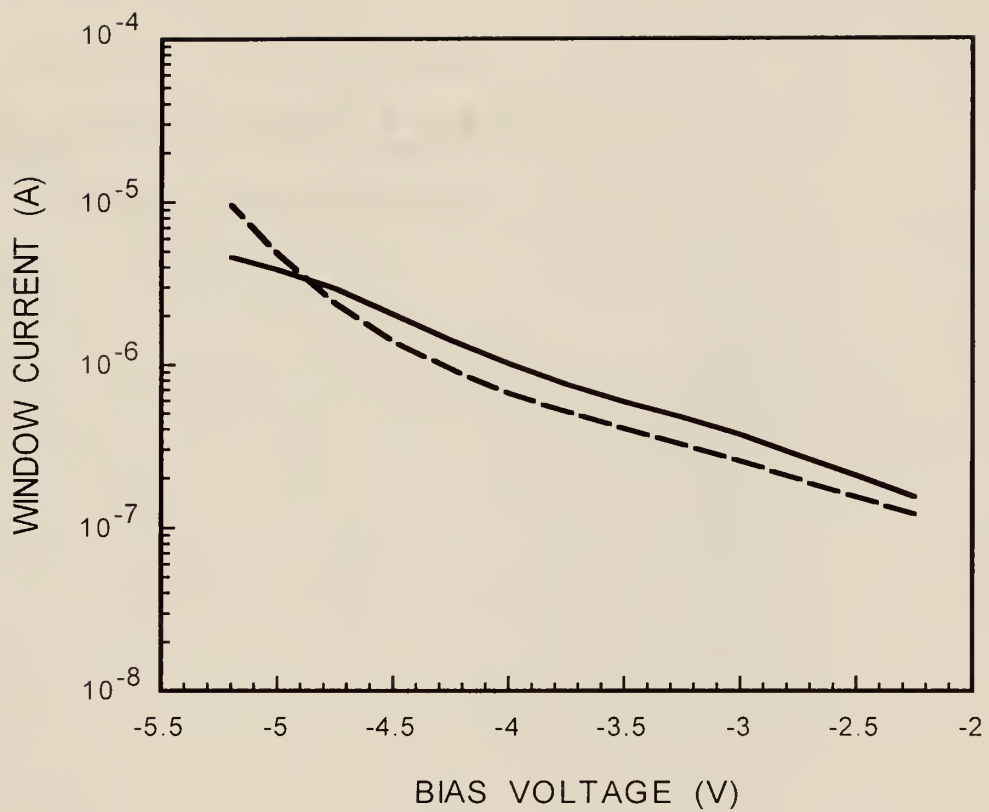


Figure 3.4. The 300K background window current with 180° field of view (FOV) of the BB TC-QWIP; the solid line (calculated) and the dashed line (measured).

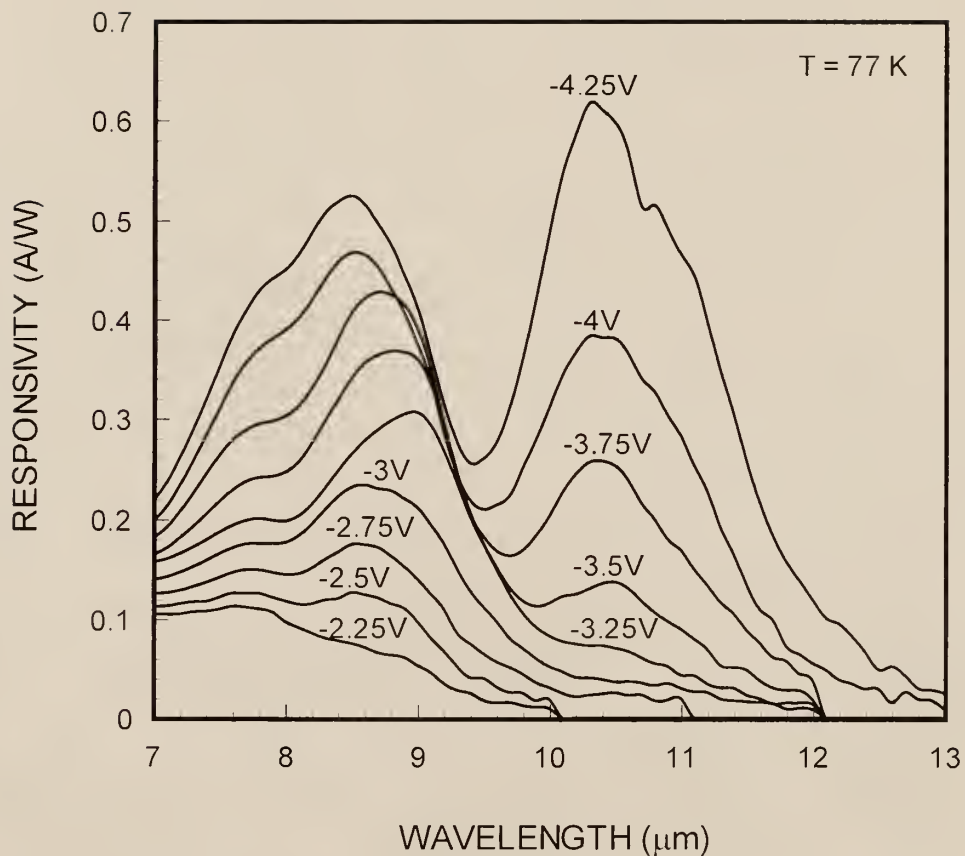


Figure 3.5. The spectral responsivity of the BB TC-QWIP measured at  $T = 77\text{K}$ .

## CHAPTER 4

### AN INGAAS/INGAAS/INGAAS TRIPLE-COUPLED QUANTUM WELL INFRARED PHOTODETECTOR FOR MWIR DETECTION

#### 4.1 Introduction

The performance of the quantum well infrared photodetectors (QWIPs) have been enhanced by various intersubband transition schemes and material systems with the maturity of the molecular beam epitaxy (MBE) technology [12]. Different intersubband transition schemes such as bound-to-bound (BTB), bound-to-quasi-bound (BTQB), bound-to-miniband (BTM), and bound-to-continuum (BTC) can be chosen to improve the device performance. For example, the BTC transition can contribute to more sensitive QWIP by aligning the final state above the barrier and the BTQB transition mechanism can reduce the dark current because the dark current due to thermionic emission is exponentially decreased with the increasing barrier height. The asymmetrical QWIP structures such as the step well, the linear graded barrier, and the coupled quantum well can affect the device performance and detection wavelength due to the voltage tunable wavelength shift for multicolor detection and the broadband detection on bias polarity. Theoretical studies of the double- and the triple-coupled quantum well structures have been reported [52,53]. The strong quantum Stark shift by the applied bias is predicted in the triple- coupled quantum well (TCQW) structure for long wavelength infrared detection. Recently, the triple-coupled quantum well infrared photodetectors (TC-QWIPs)

[54,55] using AlGaAs/InGaAs material systems grown on S.I. GaAs substrate have been demonstrated for 7-14  $\mu\text{m}$  long-wavelength infrared (LWIR) detection in which a large voltage tunable wavelength shift and high responsivity were obtained. In addition to GaAs/AlGaAs, InGaAs/GaAs, and InGaAs/AlGaAs material systems grown on GaAs substrate,  $\text{In}_{0.53}\text{Ga}_{0.47}\text{As}/\text{In}_{0.52}\text{Al}_{0.48}\text{As}$  lattice-matched QWIP structures grown on InP substrate [55,59,60] have been extensively studied, which allows the shorter wavelength detection due to the large conduction band offset. The short- and mid-wavelength infrared regions are of important for imaging and communication applications [61-67]. In this chapter, we present a new mid-wavelength infrared triple-coupled quantum well infrared photodetector (MWIR TC-QWIP) using  $\text{In}_{0.53}\text{Ga}_{0.47}\text{As}/\text{In}_{0.52}\text{Al}_{0.48}\text{As}/\text{In}_{0.3}\text{Ga}_{0.7}\text{As}$  material systems grown on InP substrate for 3-5  $\mu\text{m}$  detection.

#### 4.2 Device Design and Fabrication

The basic device structure of the MWIR TC-QWIP consists of a 40Å  $\text{In}_{0.45}\text{Ga}_{0.55}\text{As}$  quantum well Si-doped to  $N_d = 2.5 \times 10^{18} \text{ cm}^{-3}$  and two undoped 25 and 20Å shallow  $\text{In}_{0.3}\text{Ga}_{0.7}\text{As}$  quantum wells separated by two 12Å thin  $\text{In}_{0.52}\text{Al}_{0.48}\text{As}$  inner barriers, which were sandwiched by the 300Å thick  $\text{In}_{0.52}\text{Al}_{0.48}\text{As}$  barriers to form the unit cell. Ten periods of the unit cell were grown to form the absorber layer. Finally, InGaAs contact layers ( Si-doped to  $2.0 \times 10^{18} \text{ cm}^{-3}$  ) on both the top and bottom of the 10- period QWIP structure were grown on the semi-insulating InP substrate. Table 4.1 shows the layer structure of this MWIR TC-QWIP. Figure 4.1 shows the schematic conduction band diagram and the intersubband transition schemes (a) at zero and (b) negative bias

voltages. The first ( $E_2$ ) and second ( $E_3$ ) excited states were aligned due to the strong asymmetrical coupling effect of the three  $\text{In}_x\text{Ga}_{1-x}\text{As}$  quantum wells and two thin  $\text{In}_{0.52}\text{Al}_{0.48}\text{As}$  inner barriers. As clearly shown in Figure 4.1(b), the thick  $\text{In}_{0.52}\text{Al}_{0.48}\text{As}$  barrier turns into the thin triangle barrier at higher bias voltages so that the  $E_1$ - $E_3$  transition can be detected by tunneling mechanism of the photo-excited electrons through the  $E_3$  excited state.

The test mesa structure with an active area of  $216 \times 216 \mu\text{m}^2$  was created to characterize the device performance through the top contact layer and device active region down to the bottom contact layer by standard wet chemical etching. The AuGe/Ni/Au was evaporated for electrical metalization. The test device was annealed at  $T = 450^\circ\text{C}$  for two minutes after E-beam evaporation. The  $45^\circ$  facet was polished on the InP substrate for back-illumination IR radiation coupling. The silver-filled epoxy cement was used to attach the device to a package, which provides a low thermal resistance between the device and the package. The device can be mounted on a round TO-type package with 16 pins, which is one of the earliest IC packages. The ultrasonic wire-bonding through a combination of pressure and rapid mechanical vibration was used with gold wires for making electrical connection between the device and the package.

### 4.3 Results and Discussion

Figure 4.2 shows the dark current versus bias voltage (I-V) curves measured at  $T = 77$ ,  $97$ , and  $116\text{K}$  with a  $180^\circ$  field of view (FOV)  $300\text{K}$  background photocurrent of MWIR TC-QWIP. The device is under background limited performance (BLIP) when the

applied bias voltage is between -4.8V and 3.3V at T = 77K while the device is background limited between -2V and 0.8V at T = 116K.

The photocurrent was measured at T = 77 and 116K by using 1/8 monochromator and blackbody light source (T = 1273K) at 200 Hz chopped frequency. Figure 4.3 and 4.4 show the spectral responsivity of MWIR TC-QWIP at different temperatures and bias voltages. Only bound-to-continuum (BTC) transitions were observed at positive and lower negative bias voltages ( $V_b < -3.5V$  at T = 77 and 116K). The bound-to-bound (BTB) transitions were enabled at higher negative bias voltages ( $V_b > -4V$  at T = 77 and 116K). Moreover, the BTB transition was dominant at biases higher than  $V_b = -4.5V$ . The peak spectral responsivity for this MWIR TC-QWIP was 0.31 A/W at  $\lambda_p = 4.6 \mu\text{m}$ ,  $V_b = -5.5V$ , and T = 77K. The BTB transitions at a fixed bias voltage and different temperatures for the MWIR TC-QWIP were much less sensitive to the temperature increase because of the very high barrier height as shown in Figure 4.3 and 4.4. The background limited performance (BLIP) detectivity ( $D^*_{\text{BLIP}}$ ) at  $\lambda_p = 4.6 \mu\text{m}$  was found to be  $2.65 \times 10^{10} \text{ cm-Hz}^{1/2}/W$  at T = 77K and  $V_b = -4.5V$ . The peak detectivity ( $D^*$ ) under non-BLIP condition was  $1.44 \times 10^{10} \text{ cm-Hz}^{1/2}/W$  at T = 116K,  $\lambda_p = 4.6 \mu\text{m}$ , and  $V_b = -4V$ .

#### 4.4 Conclusions

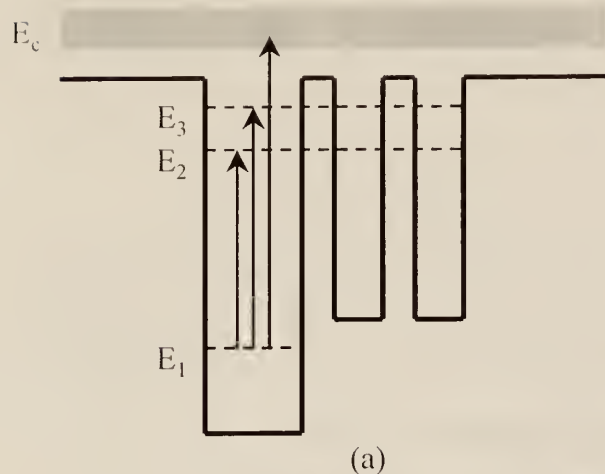
We have demonstrated a new  $\text{In}_{0.45}\text{Ga}_{0.55}\text{As}/\text{In}_{0.52}\text{Al}_{0.48}\text{As}/\text{In}_{0.3}\text{Ga}_{0.7}\text{As}$  mid-wavelength infrared triple-coupled quantum well infrared photodetector (MWIR TC-QWIP) grown on the InP substrate. This device can be operated up to T = 116K and the spectral responsivity was almost independent of the temperature. The BTC transition was

observed under both the negative and positive bias voltage conditions, while the BTB transition was detected at higher negative bias voltages. The responsivity due to BTB transition was found to increase dramatically with increasing bias voltage. It is noted that this device has better performance under negative bias voltages because both the BTB and BTC transitions can be detected with higher responsivity and lower dark current.

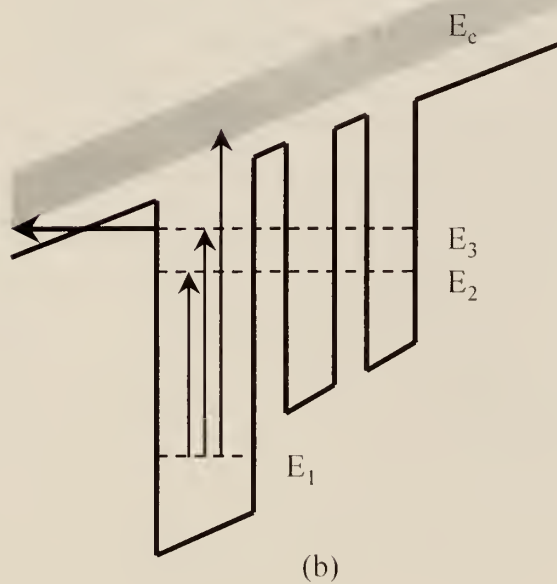
Table 4.1. The layer structure of the MWIR TC-QWIP grown on the InP substrate.

Layer	Thickness (Å)	Dopant	Concentration (cm <sup>-3</sup> )
n In <sub>0.53</sub> Ga <sub>0.47</sub> As	10000	Si	2x10 <sup>18</sup>
i In <sub>0.52</sub> Al <sub>0.48</sub> As	300	none	none
i In <sub>0.3</sub> Ga <sub>0.7</sub> As	20	none	none
i In <sub>0.52</sub> Al <sub>0.48</sub> As	12	none	none
i In <sub>0.3</sub> Ga <sub>0.7</sub> As	25	none	none
i In <sub>0.52</sub> Al <sub>0.48</sub> As	12	none	none
n In <sub>0.45</sub> Ga <sub>0.55</sub> As	40	Si	2.5x10 <sup>18</sup>
i In <sub>0.52</sub> Al <sub>0.48</sub> As	300	none	none
n In <sub>0.53</sub> Ga <sub>0.47</sub> As	10000	Si	2x10 <sup>18</sup>
S.I. InP substrate	625 ± 25 μm	none	none

( In<sub>0.45</sub>Ga<sub>0.55</sub>As/In<sub>0.52</sub>Al<sub>0.48</sub>As/In<sub>0.3</sub>Ga<sub>0.7</sub>As )



(a)



(b)

Intersubband transition energy at zero bias voltage:  $E_1-E_c$  (335 meV),  $E_1-E_3$  (270 meV)

Figure 4.1. The schematic conduction band diagram and the bound state energy of the MWIR TC-QWIP grown on the InP substrate under a) zero bias voltage and (b) negative bias conditions.

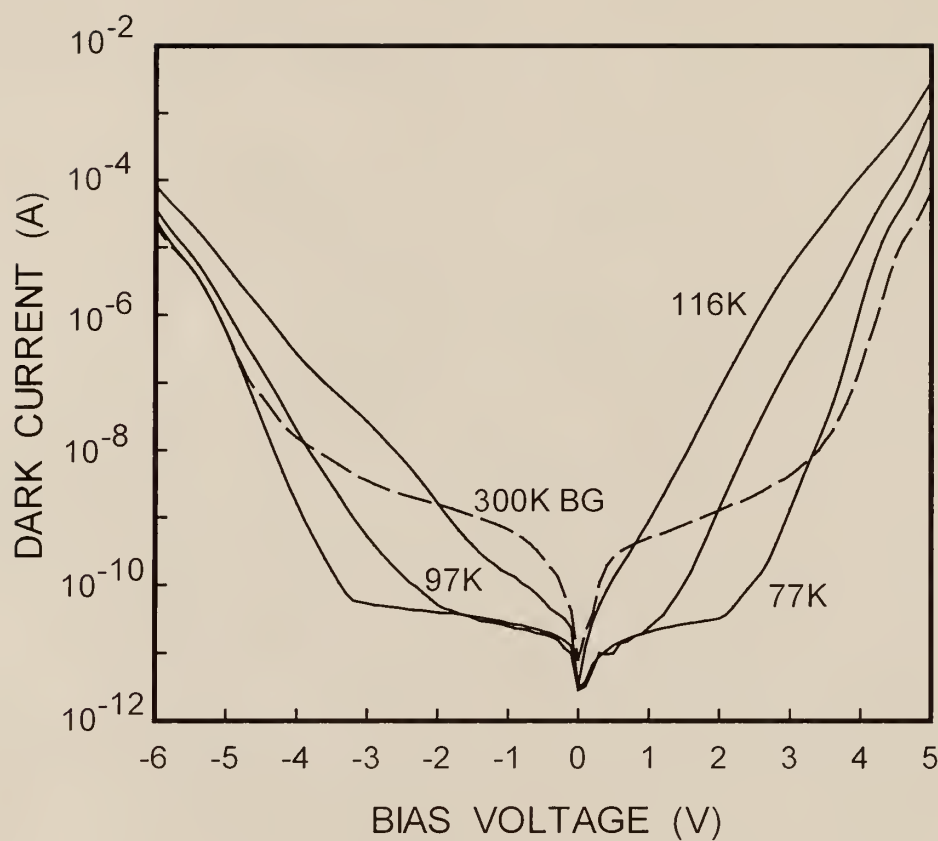


Figure 4.2. The dark current versus bias voltage (I-V) curves measured at  $T = 77$ ,  $97$ , and  $116\text{K}$  along with the  $180^\circ$  field of view (FOV)  $300\text{K}$  background photocurrent of the MWIR TC-QWIP grown on the InP substrate.

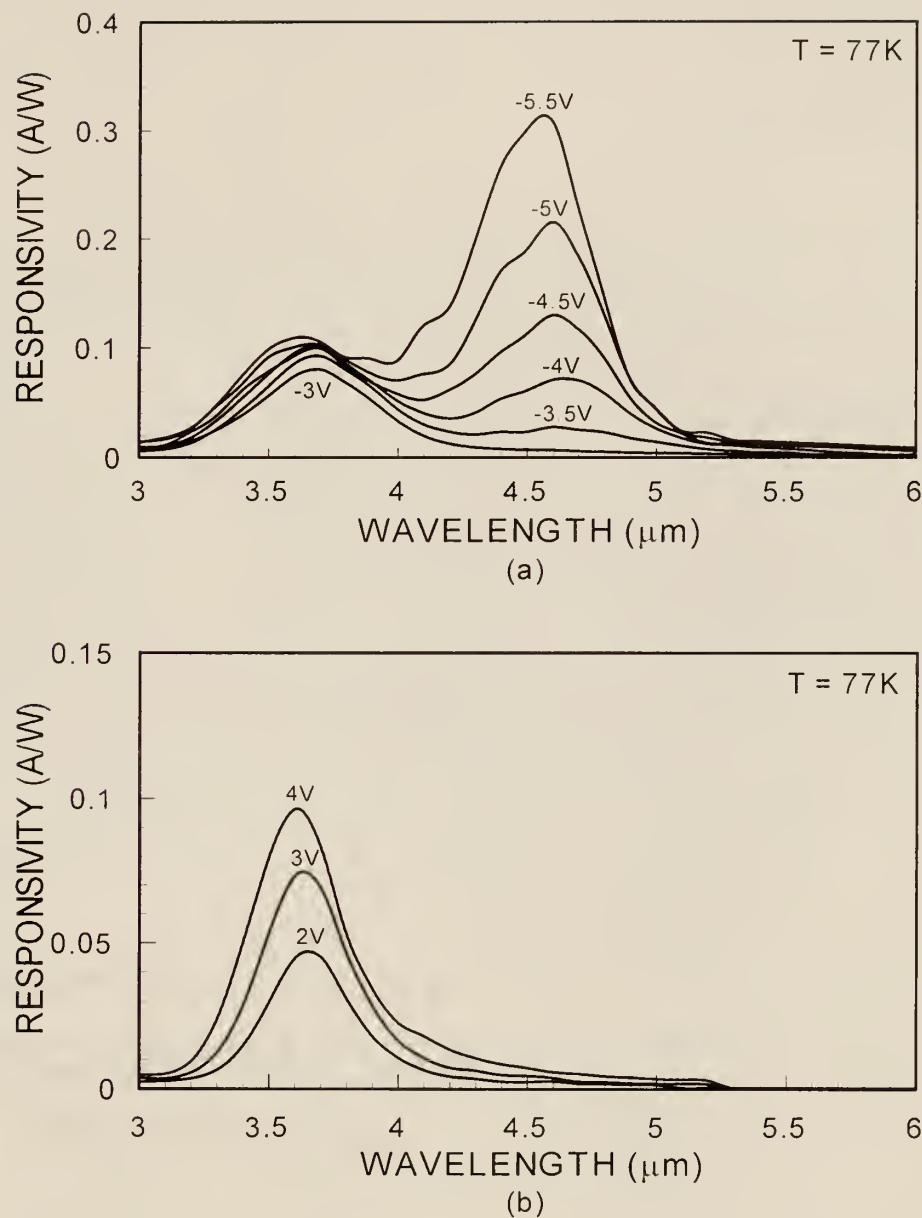


Figure 4.3. The spectral responsivity of the MWIR TC-QWIP grown on the InP substrate measured at  $T = 77\text{K}$ , under (a) negative bias and (b) positive bias conditions.

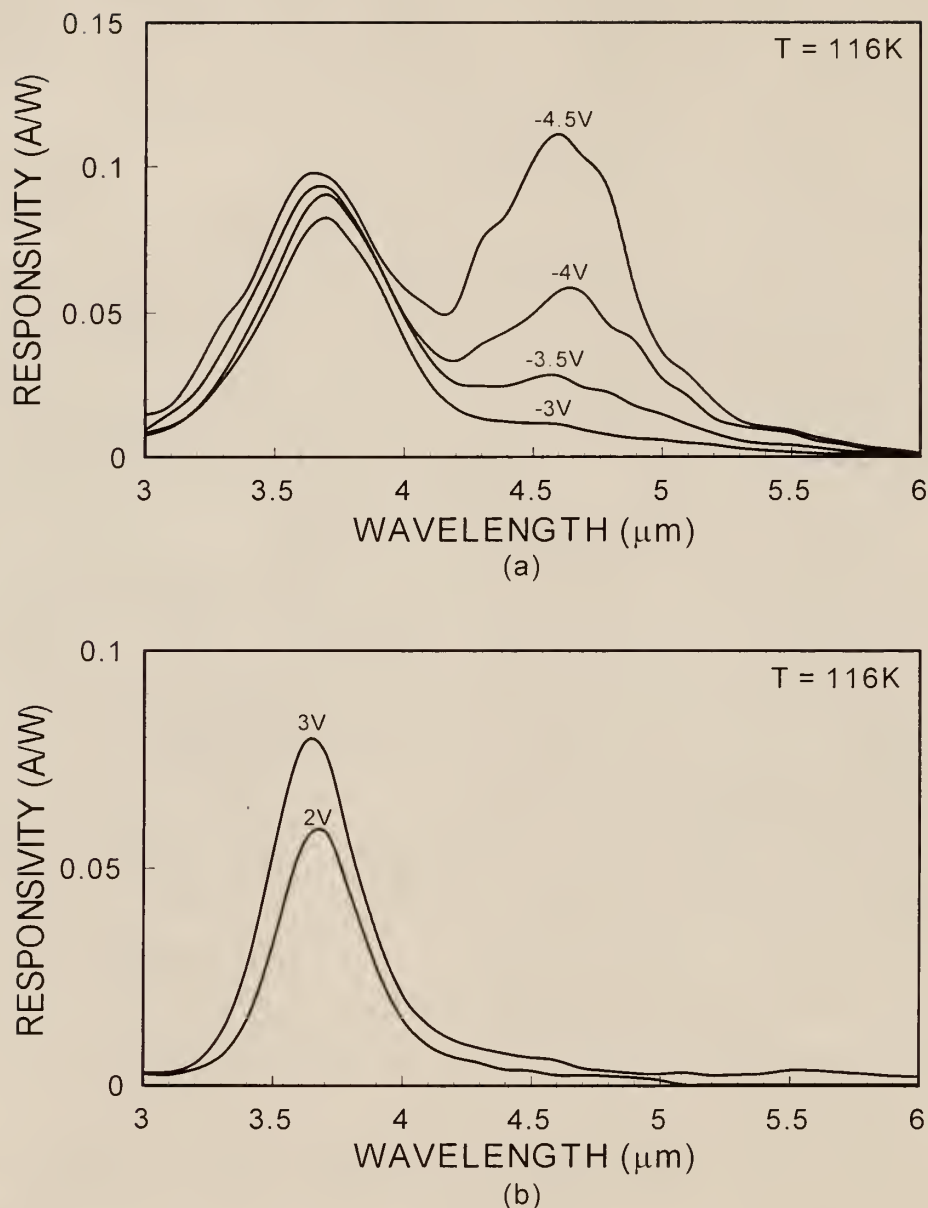


Figure 4.4. The spectral responsivity of the MWIR TC-QWIP grown on the InP substrate measured at  $T = 116\text{K}$ , under (a) negative bias and (b) positive bias conditions.

CHAPTER 5  
AN ALAS/INGAAS/ALAS/INALAS DOUBLE-BARRIER  
QUANTUM WELL INFRARED PHOTODETECTOR  
OPERATING AT 205K AND 3.4  $\mu$ m

5.1 Introduction

Quantum well infrared photodetectors (QWIPs) by using a variety of transition schemes and structures have been extremely investigated for long-wavelength (8-12  $\mu$ m) and mid-wavelength (3-5  $\mu$ m) regimes in recent years [12,68,69]. In particular, the photovoltaic (PV) mode infrared detection is attractive for practical application due to the low dark current, low power dissipation, excellent noise property, and fast integration time for focal plane array (FPA) applications. However, in most of the QWIPs, the photoresponse for the PV mode is usually much smaller than that of the photoconductive (PC) mode. As a result, most of the studies for the PV mode detection have been focussed on improving the performance by using different QWIP structures such as double-barrier quantum well (DBQW), asymmetric stepped well, and graded barrier [61,62,68-71]. The mid-wavelength infrared (MWIR) detection using intersubband transition is of great interest for imaging and target tracking applications [61-63]. The existing GaAs/AlGaAs QWIP structure grown on GaAs substrate have a limitation due to the small conduction band offset ( $\Delta E_c$ ) for shorter wavelength detection. Therefore, InGaAs/AlAs quantum well structures grown on GaAs and InP substrates have been studied for extending the intersubband transition detection wavelengths to 1.9  $\mu$ m and 1.55  $\mu$ m [64-67].

In this paper, we report a new dual-mode (i.e., PV and PC mode) operation *n*-type AlAs/InGaAs/AlAs/InAlAs double-barrier quantum well infrared photodetector (DB-QWIP) with peak detection wavelength at 3.4  $\mu\text{m}$  for mid-wavelength infrared (MWIR) detection.

## 5.2 Device Design and Fabrication

The AlAs/InGaAs/AlAs/InAlAs DB-QWIP was grown on the semi-insulating InP substrate by the molecular beam epitaxy (MBE) technique. The basic device structure for this DB-QWIP is composed of a doped  $\text{In}_{0.53}\text{Ga}_{0.47}\text{As}$  quantum well (44 $\text{\AA}$ , Si-doped to  $2.0 \times 10^{18} \text{ cm}^{-3}$ ) sandwiched between two ultra-thin undoped AlAs double-barriers (15 $\text{\AA}$ ) and separated by a thick (300 $\text{\AA}$ ) undoped  $\text{In}_{0.52}\text{Al}_{0.48}\text{As}$  barrier, which are then repeated 10 times to form the active absorber layer. Two 0.5  $\mu\text{m}$  thick highly doped  $n^+$  -  $\text{In}_{0.53}\text{Ga}_{0.47}\text{As}$  contact layers were grown on the top and bottom of the active DB-QWIP for ohmic contacts. Although the thin AlAs double barrier was highly strained (3.7%), the  $\text{In}_{0.53}\text{Ga}_{0.47}\text{As}$  quantum well and  $\text{In}_{0.52}\text{Al}_{0.48}\text{As}$  barrier layers were lattice-matched to InP substrate. As a result, excellent surface morphology and high quality of quantum well/barrier layers were obtained in this DB-QWIP structure. Table 5.1 shows the layer structure of this DB-QWIP grown on InP substrate.

In order to characterize the device performance parameters, mesa structures with active area of  $216 \times 216 \mu\text{m}^2$  were fabricated by using standard photolithography and wet chemical etching through the 10-period detector layer onto the bottom contact layer. AuGe/Ni/Au was deposited on a  $50 \times 50 \mu\text{m}^2$  area on the mesa structure for the top

contact and around the periphery of the mesa structure for the bottom contact. The IR light coupling was achieved by using a 45° facet backside illumination.

### 5.3 Results and Discussion

Figure 5.1(a) and (b) show the schematic conduction band diagram and the transition scheme, and the calculated transmission coefficient versus energy for the DB-QWIP, respectively. The multi-layer transfer matrix method (TMM) was used to calculate the transmission coefficient and the bound state energy levels in the  $\text{In}_{0.53}\text{Ga}_{0.47}\text{As}$  quantum well [69]. The effect of electron-electron interaction was considered in this calculation. The IR detection for this DB-QWIP is based on the intersubband transition from the localized ground state ( $E_1$ ) to the quasi-bound state ( $E_2$ ) inside the double barrier well. Using a lattice-matched  $\text{In}_{0.53}\text{Ga}_{0.47}\text{As}$  quantum well (44Å) and  $\text{In}_{0.48}\text{Al}_{0.52}\text{As}$  (300Å thick) barrier layer with InP substrate, an intersubband transition energy of 365 meV between the  $E_1$  and  $E_2$  bound states is obtained, which corresponds to a peak detection wavelength at 3.4 μm. The ultra-thin (15Å) wide band gap AlAs double-barrier was used to increase the barrier height so that shorter wavelength detection can be achieved by the photo-generated carrier conduction through the quasi-bound states ( $E_2$ ) above the  $\text{In}_{0.52}\text{Al}_{0.48}\text{As}$  barrier. By adjusting the well width we can push up the quasi-bound state ( $E_2$ ) and hence increase the energy spacing between the  $E_1$  and  $E_2$  bound states for shorter wavelength detection [64,65,67].

Figure 5.2 shows the dark current versus bias voltage (I-V) curves measured at T = 40, 77, 109, 137, 163, and 205K along with the 300K background window current with a

180° field of view (FOV) for this DB-QWIP. The device is under background limited performance (BLIP) at T = 77K,  $V_b < -2.5V$  and T = 109K,  $V_b < -2V$ . Due to the low device dark current this DB-QWIP was able to operate at a temperature as high as 205K while maintains good characteristics with slightly lower detectivity than the 77K operation. Furthermore, the PV mode response was observed for temperatures up to 170 K under BLIP condition. Figure 5.3(a) and (b) show the spectral responsivity curves of the DB-QWIP measured at different bias voltages and at T = 77 and 205K, respectively. The peak responsivity for the PC mode at  $V_b = -3$  V was found to be 0.159 A/W at T = 77K. This device showed a large peak responsivity for the PV mode, which was found to be 19 mA/W and 9 mA/W at T = 77 and 205K, respectively. The peak detection wavelength ( $\lambda_p$ ) for this device was found to be independent of temperature and applied bias voltage.

Figure 5.4(a) shows the peak responsivity versus temperature measured at different biases (-3.5 V >  $V_b > 0$ ). The results show that for small biases (i.e.,  $V_b < -1.5$  V) the responsivity is nearly independent of tempeature up to about 130K and then slowly rises with increasing temperature (i.e., positive temperature coefficient). It is interesting to note that the positive temperature coefficient of the responsivity has been observed only in QWIPs with short period (with number of periods less than 10) [68.72]. This is due to the fact that responsivity depends on both the quantum efficiency and the photoconductive gain (i.e.,  $R = e\lambda\eta g/hc$ ; where  $\eta$  is the quantum efficiency, and  $g$  is the photoconductive gain.). For the DB-QWIP device studied here, 10 periods of active absorber layer were used, both the photoconductive gain and quantum efficiency are expected to vary with

temperature due to the short period absorbed layer used in this structure. For typical QWIPs with 50 periods of quantum wells, the responsivity is generally found to be independent of temperature. The responsivity at higher bias voltages ( $V_b > -1.5$  V) was decreased with increasing temperature up to  $T = 163$ K. Figure 5.4(b) shows the peak responsivity versus bias voltage measured at different temperatures for the DB-QWIP. The responsivity was increased with increasing bias voltage and saturated at high biases. The increase of responsivity with bias is due primarily to the increase in the photoconductive gain with applied bias. This trend becomes more prominent at low temperatures, as clearly shown in Figure 5.4(b). The responsivity for PV mode was slightly decreased with increasing temperature. Finally, the peak detectivity ( $D^*$ ) and collection efficiency,  $\eta g$ , were calculated from the measured responsivity and dark current data. The peak detectivity and the collection efficiency for the PC mode under BLIP condition were found to be  $D_{BLIP}^* = 7.28 \times 10^{10}$  cm-Hz<sup>1/2</sup>/W and  $\eta g = 4.5\%$  at  $\lambda_p = 3.4$  μm,  $T = 77$ K, and  $V_b = -2.5$  V, respectively. The peak detectivity for the PV mode under BLIP was  $D_{BLIP}^* = 8.9 \times 10^{10}$  cm-Hz<sup>1/2</sup>/W with a 0.7 % collection efficiency at  $\lambda_p = 3.4$  μm and  $T = 77$ K. And the PV mode detectivity under BLIP at  $T = 163$ K was  $D_{BLIP}^* = 3.42 \times 10^{10}$  cm-Hz<sup>1/2</sup>/W with a 0.5 % collection efficiency at  $\lambda_p = 3.4$  μm.

#### 5.4 Conclusions

In conclusion, we have demonstrated a new high performance dual mode operation AlAs/InGaAs/AlAs/InAlAs DB-QWIP grown on the InP substrate for 3.4 μm MWIR detection. The PC and PV dual-mode detection was observed in this device with excellent

performance characteristics up to 163K. Due to the very low device dark current, excellent responsivity and BLIP detectivity were obtained for temperature below 163K, while the PV mode detection under BLIP was achieved for temperatures below 170K. The peak responsivities for PC and PV modes at T = 77K were 0.186 A/W at  $V_b = -3.5V$  and 19 mA/W, respectively. The responsivity for PV mode detection was slightly decreased with increasing temperature. The positive temperature coefficient of the responsivity was observed at low biases and high temperatures. The performance of this device was greatly enhanced by using the lattice-matched AlAs/InGaAs/AlAs/InAlAs DB-QWIP structure grown on InP substrate.

Table 5.1. The layer structure of the DB-QWIP grown on the InP substrate.

Layer	Thickness (Å)	Dopant	Concentration (cm <sup>-3</sup> )
n In <sub>0.53</sub> Ga <sub>0.47</sub> As	5000	Si	2 x 10 <sup>18</sup>
i In <sub>0.52</sub> Al <sub>0.48</sub> As	300	none	none
i AlAs	X 10	15	none
n In <sub>0.53</sub> Ga <sub>0.47</sub> As		44	Si 2 x 10 <sup>18</sup>
i AlAs		15	none
i In <sub>0.52</sub> Al <sub>0.48</sub> As		300	none
n In <sub>0.53</sub> Ga <sub>0.47</sub> As		5000	Si 2 x 10 <sup>18</sup>
S.I. InP substrate	625 ± 25 μm	none	none

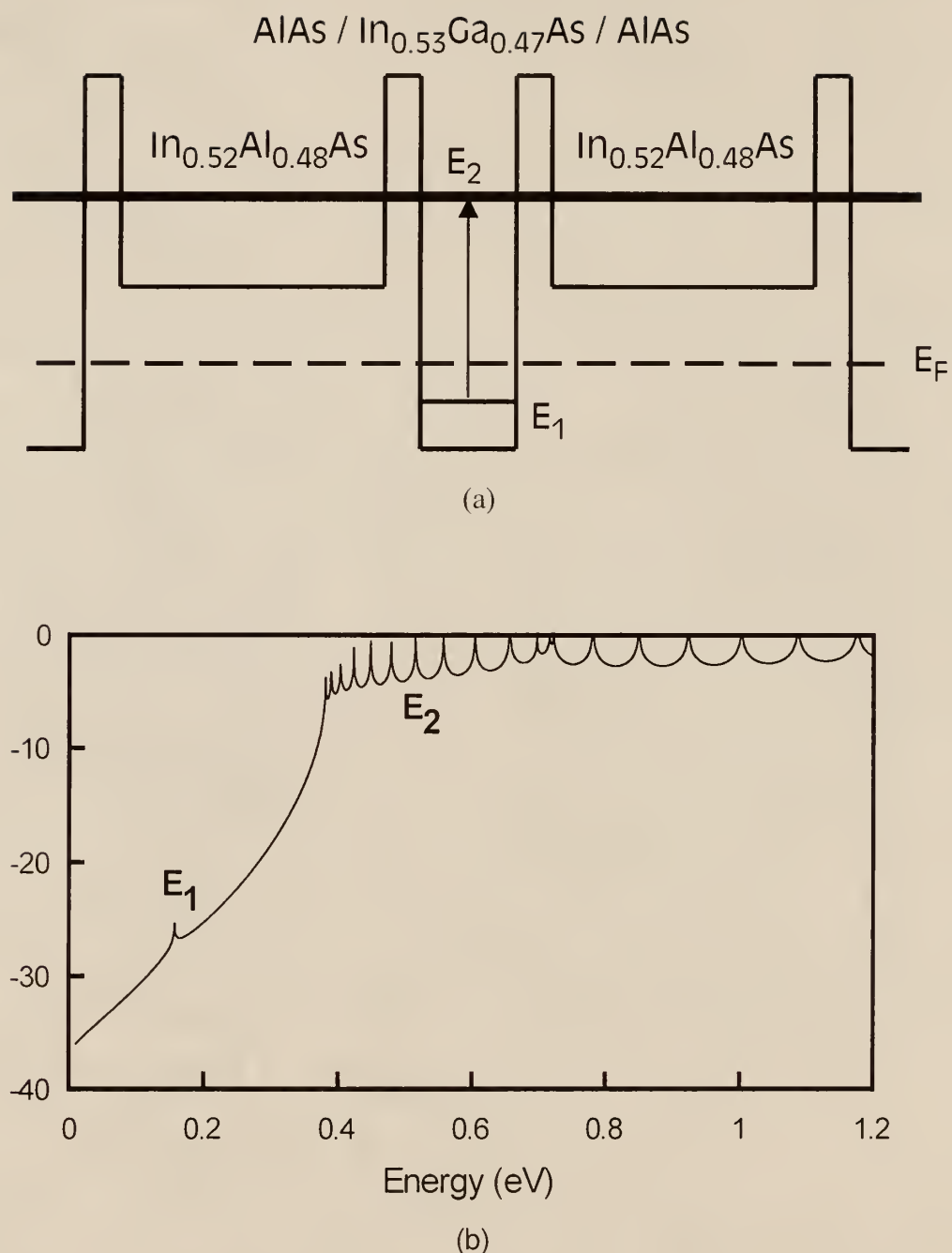


Figure 5.1. (a) The schematic conduction band diagram and transition scheme of the DB-QWIP and (b) the transmission coefficient versus energy calculated by the TMM.

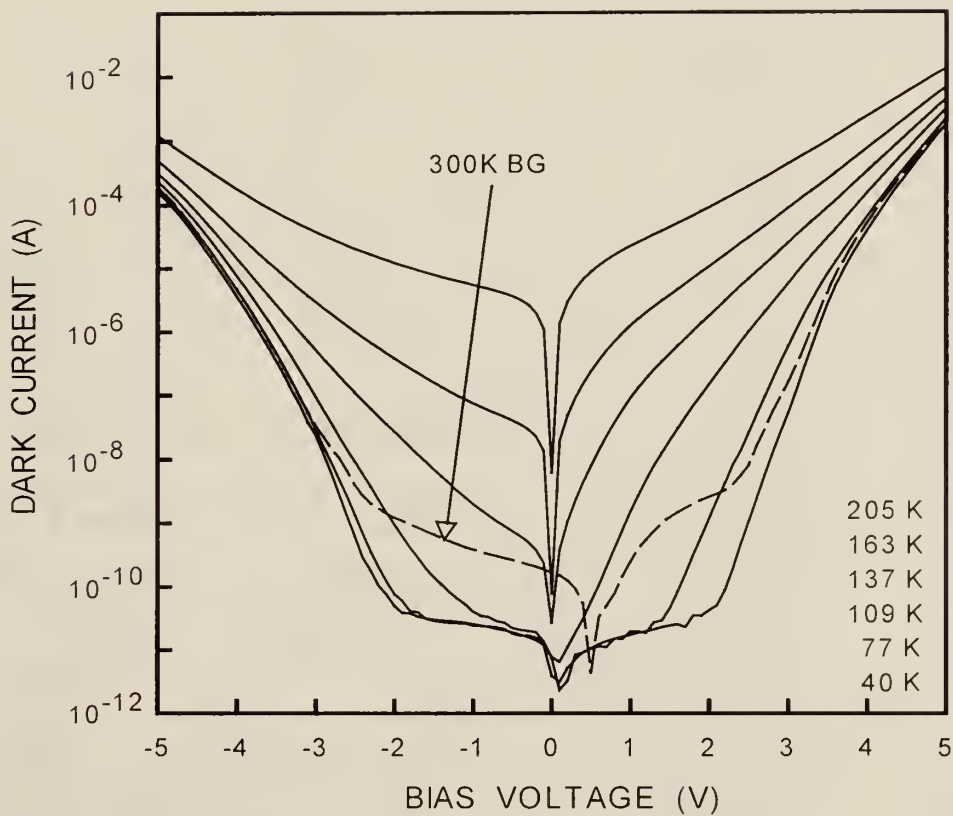


Figure 5.2. The dark current versus bias voltage measured at  $T = 40, 77, 109, 137, 163$ , and  $205\text{K}$ , along with the  $300\text{K}$  background photocurrent for the DB-QWIP.

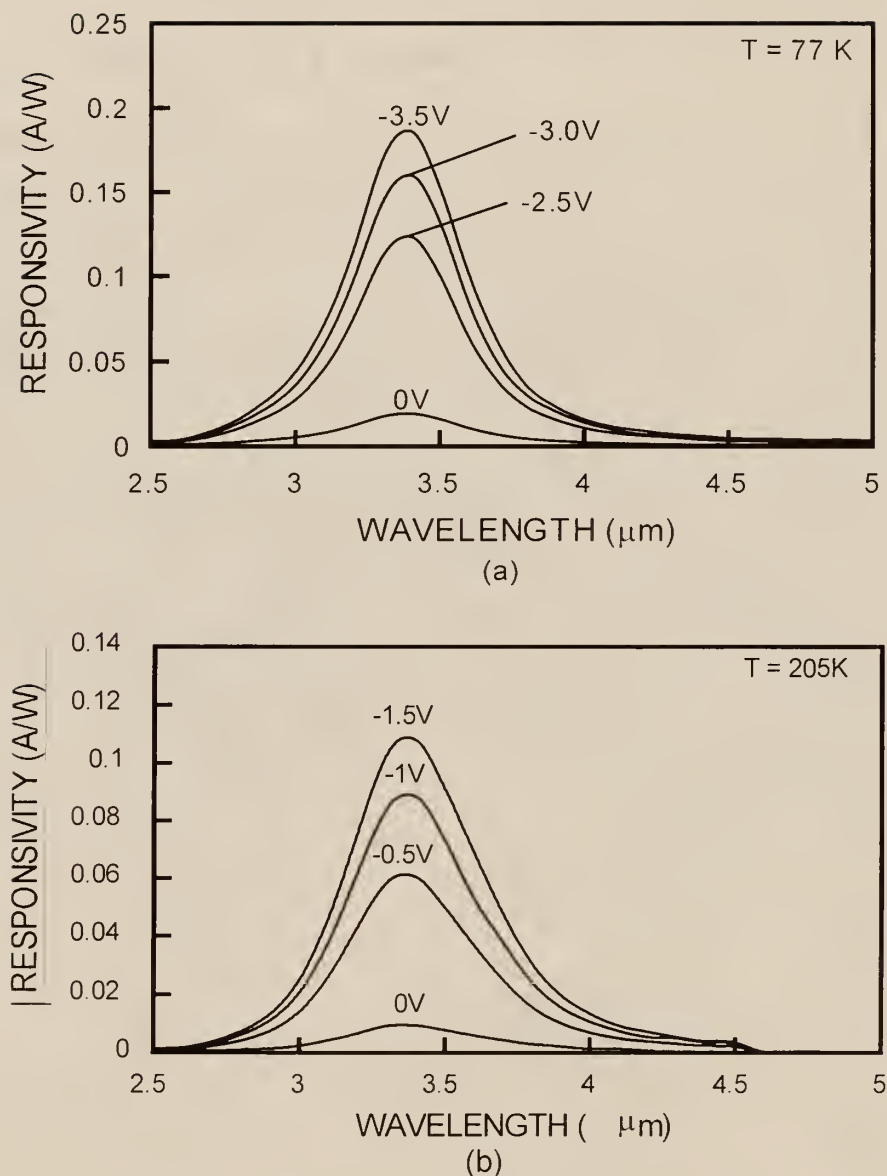


Figure 5.3. The spectral responsivity curves of the DB-QWIP measured at different biases: (a)  $T = 77 \text{ K}$  and (b)  $T = 205 \text{ K}$ .

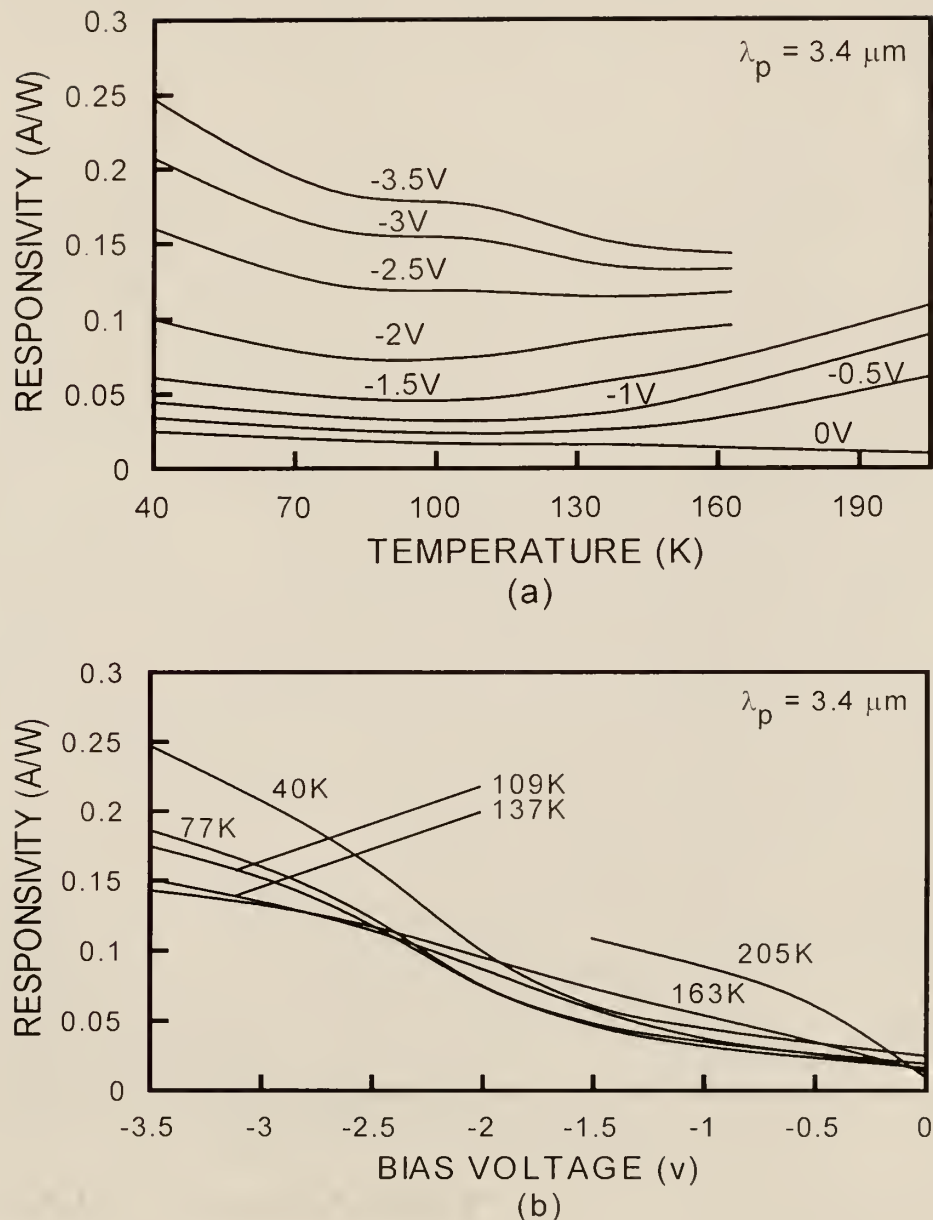


Figure 5.4. (a) The peak responsivity versus temperature for the DB-QWIP measured at different biases ( $-3.5V > V_b > 0$ ) and (b) the peak responsivity versus bias voltage measured at different temperatures.

# CHAPTER 6

## QUANTUM WELL INFRARED PHOTODETECTORS WITH DIGITAL GRADED SUPERLATTICE BARRIER FOR LONG WAVELENGTH AND BROADBAND DETECTION

### 6.1 Introduction

Quantum well infrared photodetectors (QWIPs) have been widely investigated for the mid-wavelength infrared (MWIR) and long-wavelength infrared (LWIR) as well as for multi-color or broadband infrared detection in recent years [12,73,74]. The multi-stack structure is usually employed to obtain multi-color detection in the MWIR and LWIR atmospheric spectral bands [73,74]. Voltage tunable QWIPs with asymmetrical triple-coupled quantum well structures have also been reported for multi-color infrared detection by using the quantum confined Stark effect [55]. The broadband infrared detection has been achieved by using a wide variety of device structures with variable well width and barrier height in the quantum well [58,75-82]. Levine *et al.* have reported a voltage tunable LWIR QWIP using graded barrier quantum wells to achieve large shifts in the peak detection wavelength, spectral line-width, and cutoff wavelength [82]. Duboz *et al.* has studied the effect of asymmetrical barriers on the performance of GaAs/AlGaAs QWIPs [83]. In this chapter we first report two novel high performance InGaAs/AlGaAs/GaAs QWIPs using digital graded superlattice barrier (DGSLB) to achieve the staircase-like graded barrier across the barrier region of the QWIP, which in turn gives the stepwise band gap (or composition) variation in the barrier region. This band gap engineering approach has been widely used in III-V optoelectronic devices for

band gap variation and for enhancing device performance [84,85]. The new structures enable the broadband detection and significantly improve the device performance under positive bias operation.

## 6.2 Device Design and Fabrication

Two novel InGaAs/GaAs/AlGaAs QWIP structures using digital graded superlattice barriers (DGSLB) were grown on the semi-insulating GaAs substrates by using molecular beam epitaxy (MBE). The first DGSLB QWIP structure uses the InGaAs quantum well and GaAs/AlGaAs digital graded superlattice barriers to form the DGSLB QWIP device. The second DGSLB QWIP structure adds a thin undoped AlGaAs double barrier on both sides of the InGaAs quantum well for electron wave function confinement. The DGSLB structure was used to achieve the staircase-like graded barrier in these devices. The standard MBE growth of the graded layer structure usually requires pausing the growth to change and stabilize the source temperature for the desired composition profile. As a result, it requires a longer growth time and may lead to more oxygen to be incorporated into the graded layer during the growth interruption. The compositionally digital graded superlattice barriers (DGSLB) of the QWIP structures were grown using digital graded superlattices, which enable a stepwise composition graded barrier to be formed without adjustment of the source temperature and the AlGaAs composition (i.e., using a fixed (15%) Al composition). The DGSLB structure can be obtained by using short-period superlattice structures with variable well/barrier thickness to change the Al mole fraction ratio and hence the energy band gap of the graded barrier. Adjusting the duty cycle can change the well/barrier thickness for each

superlattice unit cell (5 periods, 20Å thick). Therefore, using the DGSLB structure without changing the source temperature setting greatly simplifies the growth procedure and yields excellent wafer quality. The DGSLB layers were formed by using five superlattice unit cells in series in which the thin GaAs/Al<sub>0.15</sub>Ga<sub>0.85</sub>As layers with a 20Å period were repeated 5 times for each superlattice unit cell. The device structure for the broadband (BB-) DGSLB QWIP consists of a 50Å In<sub>0.2</sub>Ga<sub>0.8</sub>As quantum well (Si doped to  $7 \times 10^{17} \text{ cm}^{-3}$ ) and a 500Å GaAs/Al<sub>0.15</sub>Ga<sub>0.85</sub>As DGSLB layer. Each superlattice unit cell in the DGSLB-layer has a combination of five well/barrier thicknesses (17.6/2.4, 15.2/4.8, 12.8/7.2, 10.4/9.6, and 8/12Å) to obtain the target Al mole fractions of  $x = 0.018, 0.036, 0.054, 0.072$ , and 0.09 from the substrate side for the staircase-like graded barrier layer. In the double barrier (DB-) DGSLB QWIP, a thin (20Å) undoped Al<sub>0.15</sub>Ga<sub>0.85</sub>As double barrier was grown between the DGSLB layers and the 88Å In<sub>0.2</sub>Ga<sub>0.8</sub>As quantum well (Si doped to  $7 \times 10^{17} \text{ cm}^{-3}$ ) to confine the electron wave functions and to create a resonant state ( $E_4$ ) with the graded superlattice barrier. The DGSLB layer is composed of five 100Å thick superlattice layer each with 5 periods of superlattices with (well/barrier) thicknesses of 18.4/1.6, 16.8/3.2, 15.2/4.8, 13.6/6.4, and 12/8Å for the target Al mole fractions of  $x = 0.012, 0.024, 0.036, 0.048$ , and 0.06 in the Al<sub>x</sub>Ga<sub>1-x</sub>As graded barrier layer. The 5000Å contact layers (Si doped to  $2 \times 10^{18} \text{ cm}^{-3}$ ) were grown at a substrate temperature of 600°C, while the rest of the structure was grown at 510°C to avoid indium (In) desorption from the InGaAs layers. Table 6.1 and 6.2 show the layer structures of the DGSLB for the BB- and DB-DGSLB QWIPs, respectively. Finally, the complete layer structure of the BB- and DB-DGSLB QWIPs was shown in Table 6.3.

Figure 6.1(a) and (b) show the schematic conduction band diagram and the calculated transmission coefficient versus energy at zero bias using the multi-layer transfer matrix method (TMM) [24] for the broadband (BB-) DGSLB QWIP, respectively. The dotted lines denote the effective barrier height for each superlattice unit cell (5 periods, 20 Å/period), which can create a staircase-like barrier in the DGSLB layers. In this calculation, the strain effect due to lattice-mismatch between the InGaAs QW and the GaAs/AlGaAs barrier and the exchange energy due to the electron-electron interaction were considered. The E<sub>1</sub>-E<sub>4</sub>, E<sub>1</sub>-E<sub>5</sub>, and E<sub>1</sub>-E<sub>6</sub> transitions contribute to the broadband detection under positive bias condition, while only transitions from the E<sub>1</sub> to E<sub>6</sub> states were observed under negative bias because the photo-generated carriers need to surmount the abrupt side of the barrier layers. Under positive bias condition, the effective barrier will decrease gradually with increasing bias to the lowest superlattice barrier height and then the bound states aligned by the DGSLB at zero bias will broaden with increasing bias voltage to form a global miniband across the DGSLB layers and quantum wells. Thus, the broadband response can be attributed by the bound-to-miniband (B-M) state transitions under positive bias condition. On the contrary, the effective barrier height for the photo-excited electron transport will be at its maximum under negative bias condition and the slope of the DGSLB will be much steeper than under positive biases. Thus, the capture probability of the photo-excited electrons due to the bound-to-bound (B-B) transitions will be increased and normal spectral response is expected under negative bias condition.

Figure 6.2(a) and (b) show the schematic conduction-band diagram and the calculated transmission coefficient versus energy at zero bias for the double barrier (DB-) DGSLB

QWIP device. The broadband response was not observed in this device because the wave function for the peak wavelength detection is strongly confined by the thin  $\text{Al}_{0.15}\text{Ga}_{0.85}\text{As}$  double-barrier and is resonantly coupled to the wave functions of the  $E_4$ -state in the DGSLB region. Thus, normal spectral response with identical peak detection wavelength (at 12  $\mu\text{m}$ ) due to the  $E_1$  to  $E_4$  state transitions was obtained under both negative and positive biases for this device.

In order to characterize the device performance, test mesa structures with active area of  $216 \times 216 \mu\text{m}^2$  were fabricated by using standard photolithography and wet chemical etching procedure. The AuGe/Ag/Au film was deposited by E-beam evaporation on the top and periphery of the mesa structure for ohmic contacts and annealed at  $450^\circ\text{C}$  for 2 minutes. The test devices were polished to  $45^\circ$  facet on the GaAs substrates for back illumination.

### 6.3 Results and Discussion

We have performed the dark current-voltage (I-V) and spectral response measurements on both DGSLB QWIPs under negative and positive bias conditions. Excellent results were obtained in the photoresponse measurements on these devices. Figure 6.3 (a)and (b) show the dark current density as a function of applied bias voltage for the BB- and DB-DGSLB QWIPs measured at different temperatures ( $T = 35, 50, 60,$  and  $77\text{K}$ ), respectively. The 300K background window currents with a field of view (FOV) of  $180^\circ$  were also given in Fig. 6.3 (a) and (b).

As expected in the asymmetrical quantum well structure, the dark currents and photoresponse are also highly asymmetrical under positive and negative bias conditions,

which is attributed to the different effective barrier profiles under negative and positive biases, as explained previously. In both devices we have observed a much higher dark current and photo-response under positive bias condition. This is due to the barrier lowering of the DGSLB and the electron launching under positive bias condition. The BB-DGSLB QWIP device is under background limited performance (BLIP) between  $-1\text{V}$  and  $+0.75\text{V}$  at  $T = 35\text{K}$  and the BLIP temperature was  $55\text{K}$  while the DB-DGSLB QWIP is under BLIP between  $-2\text{V}$  and  $+0.35\text{V}$  at  $T = 50\text{K}$ .

Figure 6.4 shows a comparison of the dark current density as a function of the electric field at  $T = 35\text{K}$  for these two QWIP devices. Although the DB-DGSLB QWIP exhibits a longer peak wavelength ( $12 \mu\text{m}$  peak) than the BB-DGSLB QWIP ( $11 \mu\text{m}$  peak) under negative biases, the dark current density of the DB-DGSLB QWIP is slightly lower than that of the BB-DGSLB QWIP due to the use of a thin undoped  $\text{Al}_{0.15}\text{Ga}_{0.85}\text{As}$  double-barrier around the InGaAs quantum well which tends to reduce the carrier transport probability under dark condition.

The spectral response was measured at  $T = 35\text{K}$  for both the BB- and DB-DGSLB QWIPs by using an  $1/8 \text{ m}$  grating monochromater, a calibrated blackbody IR source ( $T = 1273\text{K}$ ), and a closed cycle liquid helium cryostat at  $200 \text{ Hz}$  chopped frequency. The pyroelectric detector is used to calibrate the input power of the infrared radiation from the blackbody IR source onto the photodetector.

Figure 6.5(a) and (b) show the spectral responsivity of the BB-DGSLB QWIP at  $T = 35\text{K}$  under (a) negative and (b) positive bias conditions. The peak wavelength was blue-shifted from  $11 \mu\text{m}$  to  $10.8 \mu\text{m}$  between  $-0.75\text{V}$  and  $-1.25\text{V}$  under negative bias condition. The absolute responsivity increases with the applied bias due to the increase in

photoconductive gain with increasing bias. The peak responsivities at  $\lambda_p = 10.8 \mu\text{m}$  and  $9.8 \mu\text{m}$  were found to be  $0.57 \text{ A/W}$  and  $1.07 \text{ A/W}$  at  $V_b = -1.25\text{V}$  and  $+0.75\text{V}$ , respectively. It is noted that a very broad spectral bandwidth was obtained under positive bias condition in this device. The full-width half-maximum (FWHM) spectral bandwidth of this device at  $V_b = -1.25\text{V}$  was found to be  $\Delta\lambda/\lambda_p = 13\%$  while FWHM spectral bandwidths at  $V_b = +0.75\text{V}$  and  $+0.5\text{V}$  were found to be  $\Delta\lambda/\lambda_p = 62\%$  and  $54\%$ , respectively. This broadband detection feature was attributed to the formation of miniband states by the overlapping of  $E_4$ ,  $E_5$ , and  $E_6$  wave functions, which enables the broadband detection from the  $E_1$  to the  $E_4$ ,  $E_5$ , and  $E_6$  states transitions under positive bias condition.

Figure 6.6(a) and (b) show the spectral responsivity of the DB-DGSLB QWIP at  $T = 35\text{K}$  under (a) negative and (b) positive bias conditions. The maximum peak responsivity at  $\lambda_p = 11.8 \mu\text{m}$  was found to be  $0.28 \text{ A/W}$  at  $V_b = -1.5\text{V}$  and  $T = 35\text{K}$ . However, the spectral responsivity was dramatically increased under positive bias condition due to the graded barrier lowering and electron launching effect. The peak responsivity at  $V_b = +1\text{V}$  was  $3 \text{ A/W}$  at  $\lambda_p = 12 \mu\text{m}$  and  $T = 35\text{K}$ . The FWHM spectral bandwidth at  $V_b = -1.5\text{V}$  and  $+1\text{V}$  were  $\Delta\lambda/\lambda_p = 11\%$  and  $17\%$ , respectively. A slightly broader spectral bandwidth detection was obtained under positive bias condition. The peak detection wavelength for this device was attributed to the  $E_1$  to  $E_4$  state transitions.

The detectivity of both QWIPs was calculated from the results of the responsivity and dark current measurements. Under background limited performance (BLIP) condition, it is well known that the BLIP detectivity is independent of the photoconductive gain and dark current. In the first DGSLB QWIP, the BLIP detectivity ( $D^*_{\text{BLIP}}$ ) at  $V_b = -0.75\text{V}$  and

0.75V were found to be  $7.2 \times 10^9$  cm Hz<sup>1/2</sup>/W at  $\lambda_p = 11$  μm and  $1.3 \times 10^{10}$  cm Hz<sup>1/2</sup>/W at  $\lambda_p = 9.8$  μm, respectively. The BLIP detectivity ( $D^*_{BLIP}$ ) at  $V_b = -1.5V$  and  $+1V$  for the DB-DGSLB QWIP were found to be  $5.8 \times 10^9$  cm Hz<sup>1/2</sup>/W at  $\lambda_p = 11.8$  μm and  $1.9 \times 10^{10}$  cm Hz<sup>1/2</sup>/W at  $\lambda_p = 12$  μm, respectively.

#### 6.4 Conclusions

In this chapter, we have demonstrated a novel broadband (BB-) InGaAs/AlGaAs/GaAs quantum well infrared photodetectors (QWIPs) using digital graded superlattice barrier (BB-DGSLB QWIP) for broadband detection and a high sensitivity double-barrier (DB-) InGaAs/AlGaAs/GaAs/AlGaAs DGSLB-QWIP for long-wavelength infrared (LWIR) detection. For the BB-DGSLB QWIP, the peak responsivity at  $\lambda_p = 9.8$  μm was found to be 1.07 A/W at  $V_b = +0.75V$  and  $T = 35K$ , with a corresponding BLIP detectivity ( $D^*_{BLIP}$ ) of  $1.3 \times 10^{10}$  cm Hz<sup>1/2</sup>/W. A very broad spectral response bandwidth (7 –16 μm) was obtained under positive bias condition in this device. The full-width half-maximum (FWHM) spectral bandwidth at  $V_b = +0.75V$  and  $+0.5V$  were found to be  $\Delta\lambda/\lambda_p = 62$  % and 54%, respectively, for this device. As for the DB-DGSLB QWIP device, a very large spectral responsivity and BLIP detectivity ( $D^*_{BLIP}$ ) (i.e.,  $R_i = 3$  A/W and  $D^*_{BLIP} = 1.9 \times 10^{10}$  cm Hz<sup>1/2</sup>/W) were obtained at  $V_b = +1V$  and  $\lambda_p = 12$  μm. The dark current density of the DB-DGSLB QWIP was found to be slightly lower than that of the BB-DGSLB QWIP due to the use of a thin undoped Al<sub>0.15</sub>Ga<sub>0.85</sub>As double-barrier around the InGaAs quantum well in this device. Excellent device performance was obtained in both the BB- and DB-DGSLB QWIPs.

Table 6.1. The layer structure of the digital graded superlattice barrier (1) for the BB-DGSLB QWIP.

Layer		Thickness (Å)	Average (x)	Dopant	Concentration (cm <sup>-3</sup> )
i GaAs	X 5	8	0.09	none	none
i Al <sub>0.15</sub> Ga <sub>0.85</sub> As		12		none	none
i GaAs	X 5	10.4	0.072	none	none
i Al <sub>0.15</sub> Ga <sub>0.85</sub> As		9.6		none	none
i GaAs	X 5	12.8	0.054	none	none
i Al <sub>0.15</sub> Ga <sub>0.85</sub> As		7.2		none	none
i GaAs	X 5	15.2	0.036	none	none
i Al <sub>0.15</sub> Ga <sub>0.85</sub> As		4.8		none	none
i GaAs	X 5	17.6	0.018	none	none
i Al <sub>0.15</sub> Ga <sub>0.85</sub> As		2.4		none	none

Table 6.2. The layer structure of the digital graded superlattice barrier (2) for the DB-DGSLB QWIP.

Layer		Thickness (Å)	Average (x)	Dopant	Concentration (cm <sup>-3</sup> )
i GaAs	X 5	12	0.06	none	none
i Al <sub>0.15</sub> Ga <sub>0.85</sub> As		8		none	none
i GaAs	X 5	13.6	0.048	none	none
i Al <sub>0.15</sub> Ga <sub>0.85</sub> As		6.4		none	none
i GaAs	X 5	15.2	0.036	none	none
i Al <sub>0.15</sub> Ga <sub>0.85</sub> As		4.8		none	none
i GaAs	X 5	16.8	0.024	none	none
i Al <sub>0.15</sub> Ga <sub>0.85</sub> As		3.2		none	none
i GaAs	X 5	18.4	0.012	none	none
i Al <sub>0.15</sub> Ga <sub>0.85</sub> As		1.6		none	none

Table 6.3. The complete layer structure of the BB- and DB-DGSLB QWIP.

Layer		Thickness (Å)	Dopant	Concentration (cm <sup>-3</sup> )
n GaAs (top contact)		5000	Si	2x10 <sup>18</sup>
Digital Graded Barrier (1)	X 5	500	none	none
n In <sub>0.2</sub> Ga <sub>0.8</sub> As		50	Si	7x10 <sup>17</sup>
Digital Graded Barrier (1)		500	none	none
n GaAs (middle contact)		5000	Si	2x10 <sup>18</sup>
Digital Graded Barrier (2)	X 5	500	none	none
i Al <sub>0.15</sub> Ga <sub>0.85</sub> As		20	none	none
n In <sub>0.2</sub> Ga <sub>0.8</sub> As		88	Si	7x10 <sup>17</sup>
i Al <sub>0.15</sub> Ga <sub>0.85</sub> As		20	none	none
Digital Graded Barrier (2)		500	none	none
n GaAs (bottom contact)		5000	Si	2x10 <sup>18</sup>
S.I. GaAs substrate		625 ± 25 µm	none	none

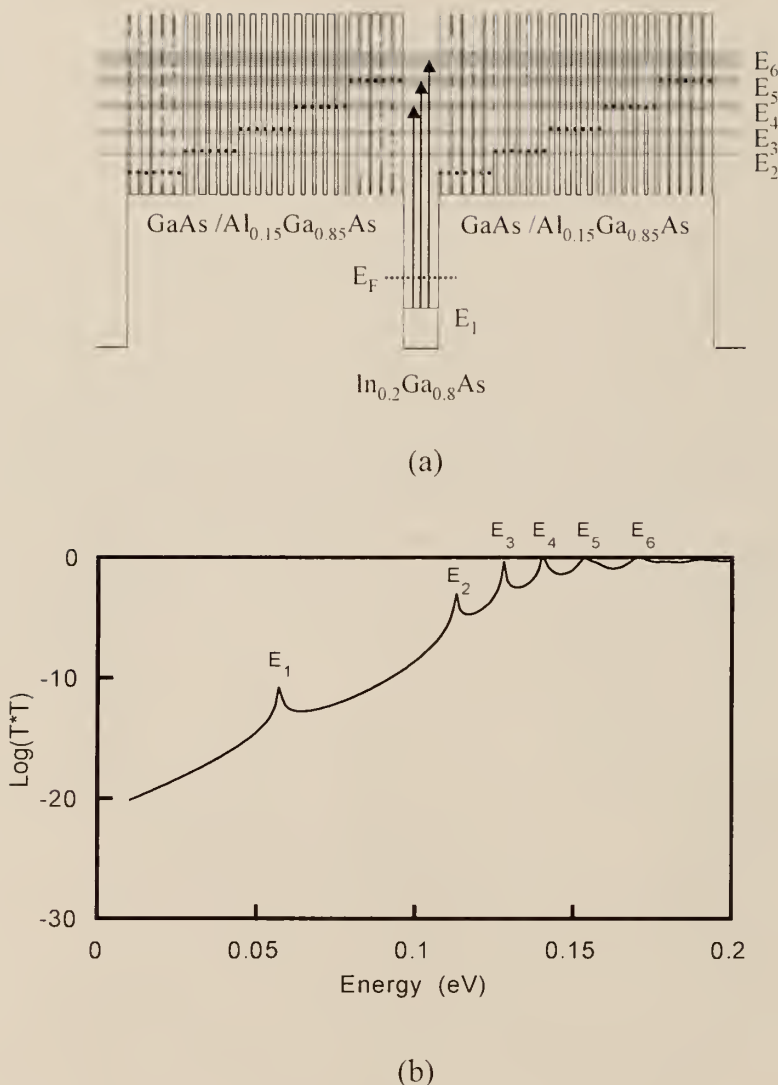
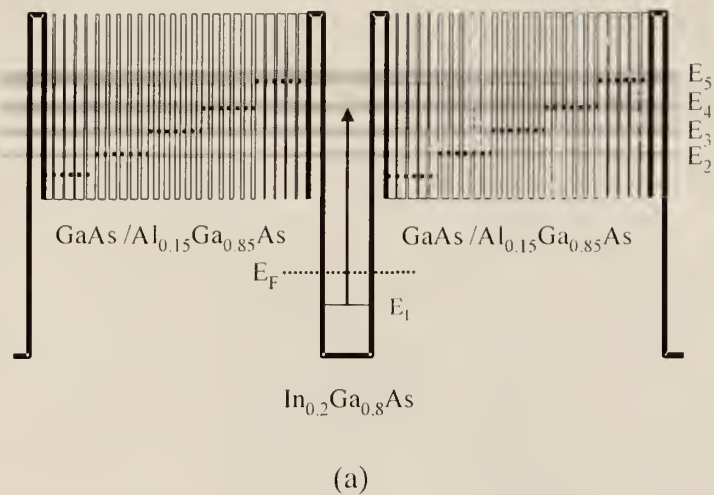
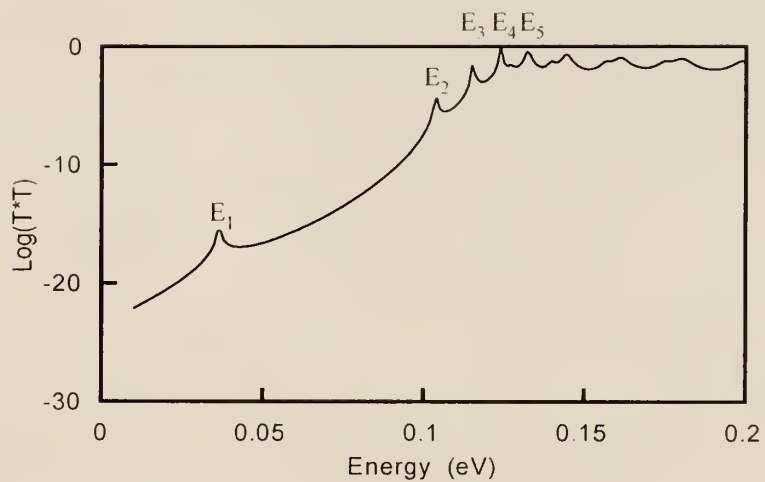


Figure 6.1. (a) The schematic conduction band diagram and (b) the calculated transmission coefficient versus at zero bias for the broadband (BB-) DGSLB QWIP.



(a)



(b)

Figure 6.2. (a) The schematic conduction band diagram and (b) the calculated transmission coefficient energy at zero bias for the double barrier (DB-) DGSLB QWIP.

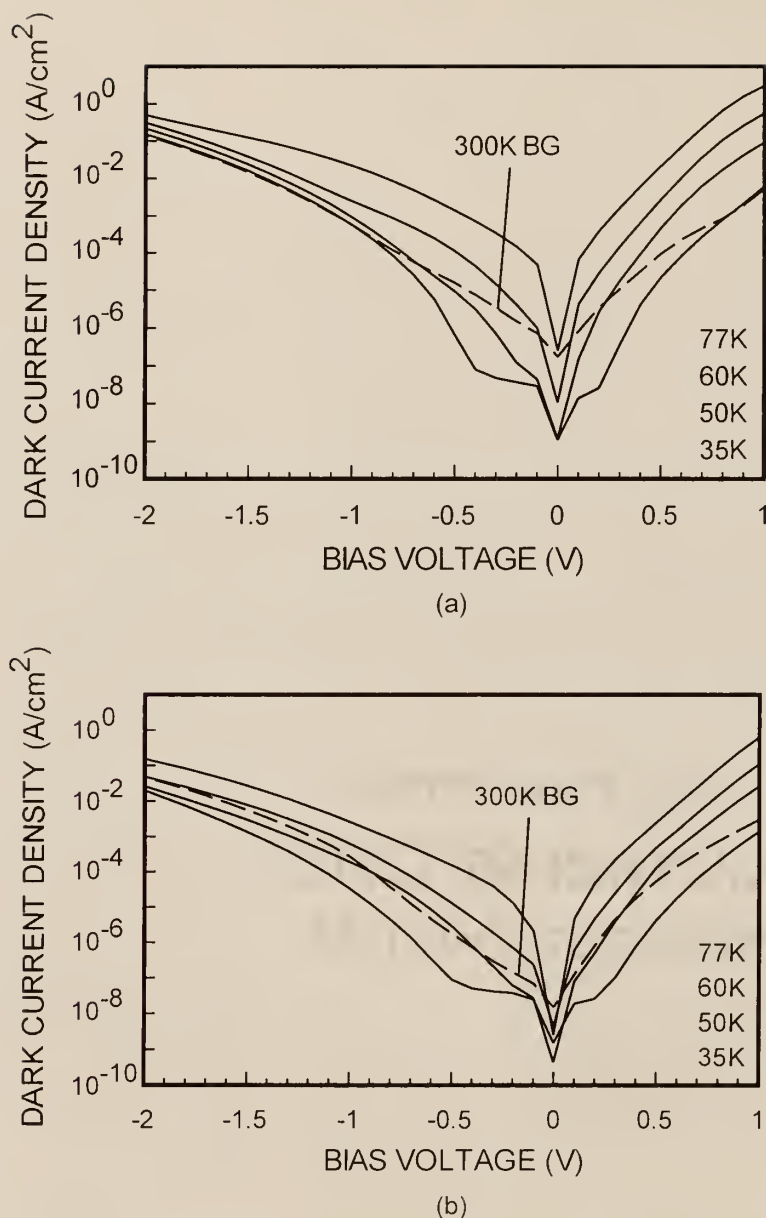


Figure 6.3. The dark current density versus bias voltage for (a) the BB-DGSLB QWIP and (b) the DB-DGSLB QWIP. The dashed line is the 300K background photocurrent.

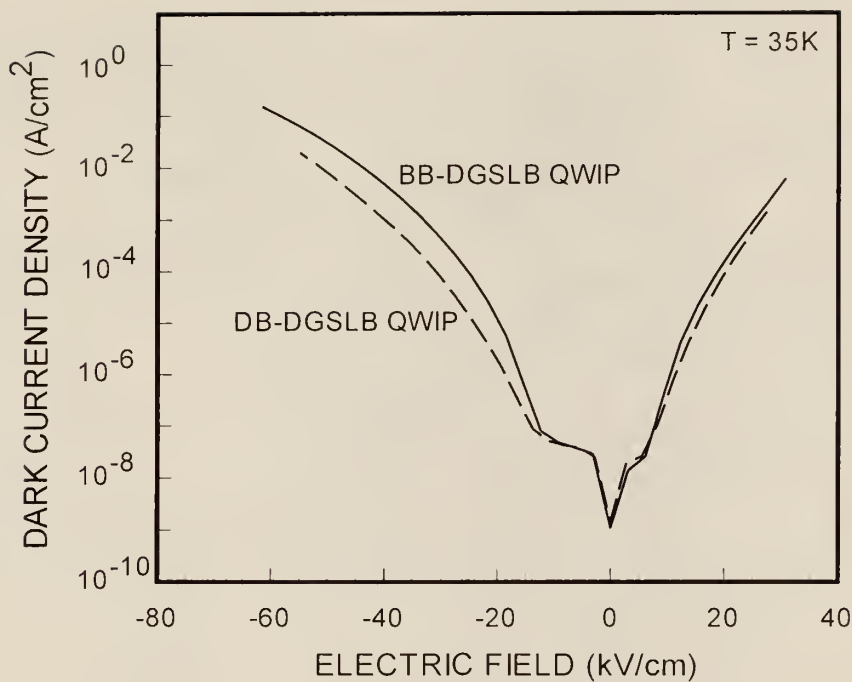


Figure 6.4. A comparison of the dark current density versus the electric field for the BB-DGSLB QWIP (solid line) and the DB-DGSLB QWIP (dashed line).

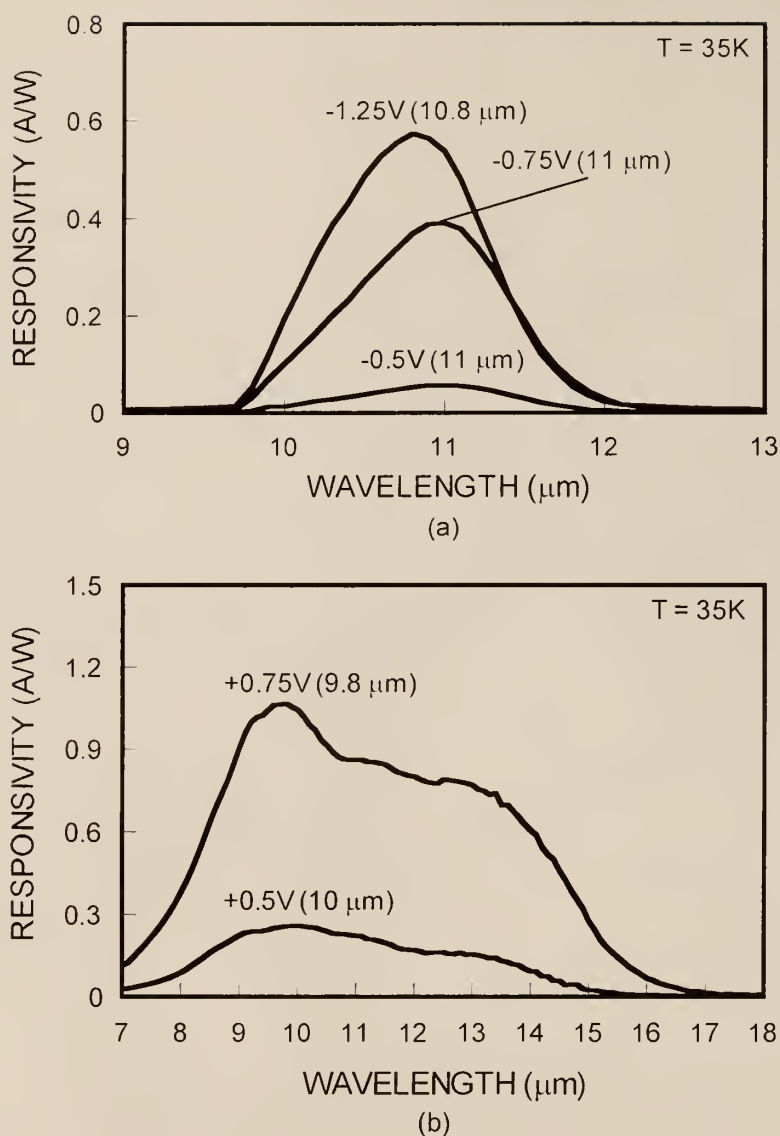


Figure 6.5. The spectral responsivity of the BB-DGSLB QWIP device at  $T = 35K$ : (a) at negative bias and (b) at positive bias condition.

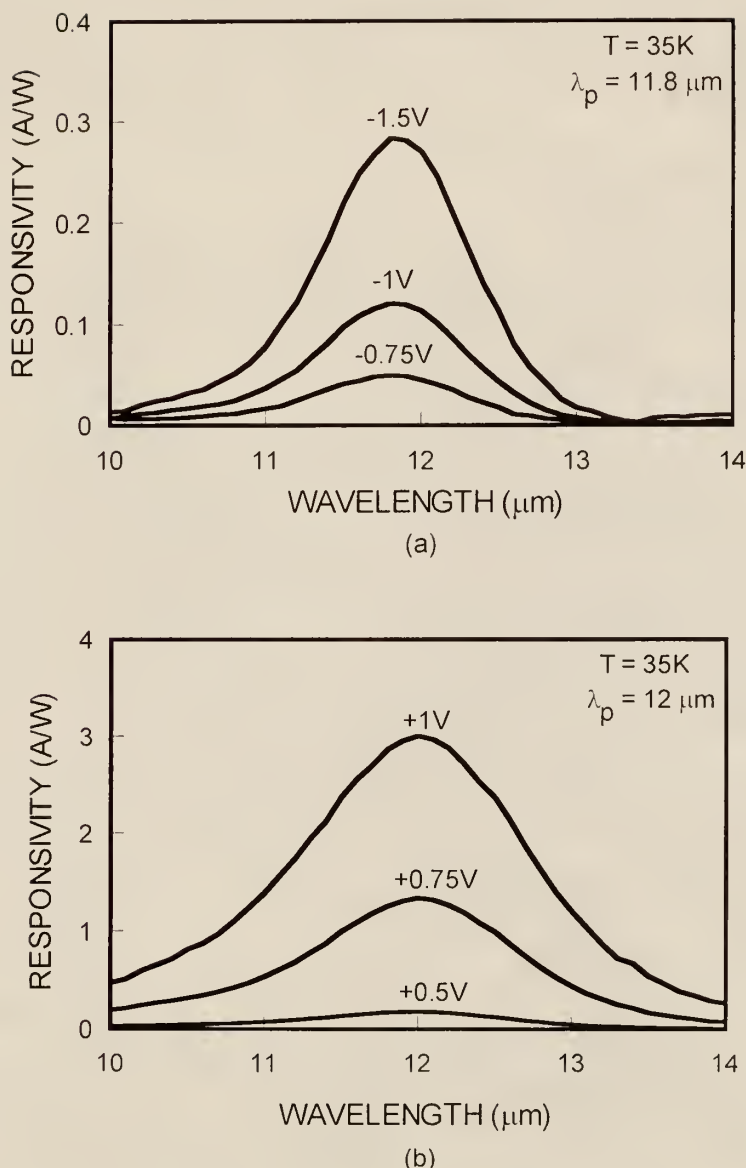


Figure 6.6. The spectral responsivity of the DB-DGSLB QWIP at  $T = 35\text{K}$ : (a) at negative and (b) at positive bias condition.

# CHAPTER 7

## HIGH SENSITIVITY

### QUANTUM WELL INFRARED PHOTODETECTORS WITH LINEAR GRADED BARRIER

#### 7.1 Introduction

In recent years, quantum well infrared photodetectors (QWIPs) have been widely developed for 3-5  $\mu\text{m}$  mid-wavelength infrared (MWIR) and 8-14  $\mu\text{m}$  long-wavelength infrared (LWIR) spectral regimes [12,86-96]. The matured III-V compound semiconductor growth technology and the flexibility of the device structure have induced the rapid development of various QWIP structures. The multi-color IR detectors for practical imaging applications such as target discrimination, remote sensing system, medical imaging, and tracking system have been extensively investigated by using the multi-stack QWIP and voltage-tunable asymmetrical coupled quantum well structures. In particular, the broadband QWIPs covering the entire LWIR region were demonstrated by repeating the quantum wells with different well width and depth [58,78]. The asymmetric structure was introduced to detect the broadband region [83,84]. This broadband detection is required in the infrared (IR) spectrometers, which measure the interaction of the IR radiation with experimental samples. To further optimize the QWIP performance, considerable efforts have been devoted to the theoretical investigation of intersubband optical absorption in various quantum well structures [97-100]. Theoretical study of the intersubband and free-carrier absorption coefficients in the heavily doped QW structure has also been reported [97]. The effective mass approximation which takes into account

the effects of strain and subband nonparabolicity has been used to calculate the electronic states for the intersubband optical absorption coefficient in the strained double- barrier quantum well structure [98]. The nonlinear spectral responsivity versus applied bias has been studied, in which the physical effects of QWIPs under localized excitation [99] and carrier depletion or accumulation on the local electric field have been theoretically shown in the QWIP devices [100]. In addition, the new light coupling schemes in the corrugated (C-) QWIP [101] and the quantum-grid infrared photodetector (QGIP) [102] have been developed, which showed efficient coupling of normal incidence light into these QWIP devices.

In this chapter, we report two high performance QWIPs with linear graded barrier which are a InGaAs/AlGaAs broadband (BB-) linear graded barrier (LGB) quantum well infrared photodetector (QWIP) and a high-sensitivity AlGaAs/InGaAs/AlGaAs double-barrier (DB-) LGB QWIP for broadband wavelength regime and long-wavelength detection.

## 7.2 Device Design and Fabrication

These two linear grade barrier (LGB) QWIPs were grown on semi-insulating GaAs substrate by using molecular beam epitaxy (MBE). The top-stack for BB-LGB QWIP consists of a 45Å  $\text{In}_{0.26}\text{Ga}_{0.74}\text{As}$  quantum well (Si-doped to  $7 \times 10^{17} \text{ cm}^{-3}$ ) and a 500Å linear graded barrier ( $\text{Al}_x\text{Ga}_{1-x}\text{As}$ ) as a unit cell in which the Al mole fraction of linear graded barrier was increased from 1.8% to 9% starting from the substrate side. This unit cell was repeated 15 times for the whole BB-LGB QWIP structure. In the DB-LGB QWIP, a thin 20Å layer ( $\text{Al}_{0.15}\text{Ga}_{0.85}\text{As}$ ) was grown between the 72Å  $\text{In}_{0.26}\text{Ga}_{0.74}\text{As}$

quantum well (Si-doped to  $7 \times 10^{17} \text{ cm}^{-3}$ ) quantum well and the LGB layer to obtain the double-barrier structure which can contribute to confine the wave function. This structure can induce the strong intersubband absorption from the ground state ( $E_1$ ) to the excited state ( $E_5$ ) which was resonantly created with the  $\text{Al}_x\text{Ga}_{1-x}\text{As}$  ( $x=1.8\% \sim 9\%$ ) 500Å linear graded barrier (LGB). The quantum well and double-barrier with the linear graded barrier were also repeated 15 times for the bottom-stack. Finally, the ohmic contact layers (Si-doped to  $2 \times 10^{18} \text{ cm}^{-3}$ ) with different thicknesses (3000, 7000, and 5000Å) were grown on the top of the BB-LGB QWIP stack and on the bottom of the DB-LGB QWIP, and between the two stacks, respectively. Table 7.1 shows the complete layer structure of the BB- and DB-LGB QWIPs.

Figure 7.1 shows (a) the schematic conduction band diagram and the intersubband transition scheme and (b) the calculated transmission coefficient by using the multi-layer matrix method (TMM) for the BB-LGB QWIP. The photo-generated carrier transport mechanism for the BB- and DB-LGB QWIP is definitely dependent on the applied bias polarity as described in chapter 6. Under positive bias condition, the slope of the linear graded barrier was gradually decreased with increasing bias so that the excited electron for longer-wavelength detection can easily overcome the barrier. Therefore, the broadband (BB) detection can be obtained by overlapping the  $E_1-E_3$ ,  $E_1-E_4$ ,  $E_1-E_5$ , and  $E_1-E_6$  transitions under positive bias condition. On the contrary, the linear graded barrier will be much steeper and the barrier height will be at its maximum under negative bias condition. Thus, the capture probability of the photo-generated electron carriers into the quantum well was enhanced by the higher barrier height and then the longer-wavelength

detection due to the  $E_1-E_3$  and  $E_1-E_4$  transitions was not expected and normal spectral response with two-peak wavelength was achieved under negative bias condition.

Figure 7.2 shows (a) the schematic conduction band diagram and the intersubband transition scheme and (b) the calculated transmission coefficient at zero bias for the DB-LGB QWIP. The high spectral response can be obtained by the thin  $\text{Al}_{0.15}\text{Ga}_{0.85}\text{As}$  barrier which confine the wave functions and then induce the strong intersubband absorption. Normal spectral response was expected under both positive and negative bias condition.

### 7.3 Results and Discussion

The test mesa structures with an active area of  $216 \times 216 \mu\text{m}^2$  was processed to characterize the device performance by using standard photo-lithography and wet chemical etching procedure. The  $\text{AuGe}/\text{Ag}/\text{Au}$  ( $300\text{\AA}/1000\text{\AA}/1500\text{\AA}$ ) was deposited on the top and the periphery of the mesa structure for ohmic metalization. The device was annealed at  $450^\circ\text{C}$  for 2 minutes. The GaAs substrate was polished for  $45^\circ$  facet back-illumination.

Figure 7.3 (a) and (b) shows the dark I-V curves measured at  $T = 35, 50, 60$ , and  $77\text{K}$  for the BB- and DB-LGB QWIPs, respectively. The  $300\text{K}$  background window current with  $180^\circ$  FOV (field of view) was also given as the dashed lines in Fig. 7.3 (a) and (b). The BB-DGB QWIP is under background limited performance (BLIP) between  $-4\text{V}$  and  $+0.9\text{V}$  at  $T = 50\text{K}$  and  $T_{\text{BLIP}} = 58\text{K}$  while the DB-LGB QWIP is under BLIP between  $-1.6\text{V}$  and  $+0.7\text{V}$  at  $T = 60\text{K}$  and  $T_{\text{BLIP}} = 65\text{K}$ . As shown in Fig. 7.3 (a) and (b), the dark current of the BB-LGB QWIP is several orders of magnitude higher than the DB-LGB QWIP, which is due to the thin  $20\text{\AA}$  double-barrier in the DB-LGB QWIP. In addition,

the asymmetrical dark currents can be attributed to the different carrier transport properties depending on the bias polarity.

The spectral response measurement was performed with 45° facet back-illumination by using an 1/8 m grating monochromator, a calibrated blackbody IR source ( $T = 1273\text{K}$ ), and a closed cycle liquid helium cryostat at 200 Hz chopper frequency. The operating temperatures of the devices for the spectral response measurement were  $T = 35$ , 60, and 77K for the BB- and DB-LGB QWIP.

Figure 7.4 shows the spectral responsivity of the BB-LGB QWIP measured at  $T = 35\text{K}$  under (a) negative and (b) positive bias condition. The maximum peak responsivity at  $T = 35\text{K}$  and  $-3\text{V}$  was  $1.61 \text{ A/W}$  at a peak wavelength with  $9.9 \mu\text{m}$  which is due to the  $E_1\text{-}E_5$  transition. The  $E_1\text{-}E_6$  transition was also obtained in this measurement, which has much lower responsivity than the  $E_1\text{-}E_5$  transition. The spectral responsivity was increased with increasing bias voltage. The inset in Fig. 7.4 (a) shows the linear dependence of the peak wavelength for the  $E_1\text{-}E_5$  and  $E_1\text{-}E_6$  transitions under applied negative bias voltage. The peak wavelength was blue-shifted with increasing bias voltage ranging from  $10.2$  to  $9.9 \mu\text{m}$  and  $8.5$  to  $7.5 \mu\text{m}$  for the  $E_1\text{-}E_5$  and  $E_1\text{-}E_6$  transitions, respectively. The peak responsivity at  $+2.75\text{V}$  and  $T = 35\text{K}$  was found to be  $1.75 \text{ A/W}$  at  $\lambda_p = 11.9 \mu\text{m}$ . The three-peak wavelength ( $8.9$ ,  $10.2$ , and  $11.9 \mu\text{m}$ ) was obtained at  $+2.7\text{V}$ , which were due to the  $E_1\text{-}E_6$ ,  $E_1\text{-}E_5$ , and  $E_1\text{-}E_4$  transitions. The full-width half-maximum (FWHM) spectral bandwidth of this device at  $+2.75\text{V}$  and  $T = 35\text{K}$  was  $\Delta\lambda/\lambda_p = 52\%$ . This broadband detection covering from  $6.5$  to  $16 \mu\text{m}$  under positive bias condition can be achieved by the overlapping of the  $E_1\text{-}E_6$ ,  $E_1\text{-}E_5$ ,  $E_1\text{-}E_4$ , and  $E_1\text{-}E_3$  transitions. The  $E_1\text{-}E_6$  and  $E_1\text{-}E_5$  transitions were first enabled at lower positive bias

voltage (+1V). The E<sub>1</sub>-E<sub>4</sub> and E<sub>1</sub>-E<sub>3</sub> transitions can be gradually detected with increasing bias voltage. However, the contribution of the E<sub>1</sub>-E<sub>3</sub> transition for the broadband detection is much smaller than the other transitions at higher positive bias voltage. Figure 7.5 shows the spectral responsivity measured at T = 60K under (a) negative and (b) positive bias condition. The peak responsivity with 1.41 A/W at 10 μm was obtained at –3V and T = 60K. The wavelength tunability was ranging from 10.5 to 10 μm and 8.6 to 7.5 μm for the E<sub>1</sub>-E<sub>5</sub> and E<sub>1</sub>-E<sub>6</sub> transitions, respectively. The peak responsivity at +1.45V was found to be 0.73 A/W at T = 60K and  $\lambda_p = 11.1 \mu\text{m}$ . The FWHM spectral bandwidth at –3V was found to be  $\Delta\lambda/\lambda_p = 12 \%$  while FWHM spectral bandwidths at +1V and +1.45V were found to be  $\Delta\lambda/\lambda_p = 42 \%$  and 45 %, respectively. As shown in the results at T = 35K, the broadband wavelength detection was achieved at T = 60K under positive bias voltage. Figure 7.6 shows the spectral responsivity measured at T = 77K under negative bias condition. The blue-shift of the peak wavelength was also observed at T = 77K. The responsivity can not be measured at positive bias voltage because Transimpedance Amplifier (TIA) was saturated due to the high dark current at T = 77K under positive bias condition.

Figure 7.7 shows the spectral responsivity measured at T = 35K for the DB-LGB QWIP under (a) negative and (b) positive bias condition. The peak responsivity due to the E<sub>1</sub>-E<sub>5</sub> transition at T = 35K and –4.5V was found to be 1.23 A/W with a peak wavelength at  $\lambda_p = 9.2 \mu\text{m}$ . The responsivity with 4.38 A/W at  $\lambda_p = 9.1 \mu\text{m}$  was obtained at +3.5V and T = 35K. The FWHM spectral bandwidths under positive bias voltage were two times broader than under negative bias voltage because the E<sub>1</sub>-E<sub>4</sub> transition for the longer-wavelength detection can be obtained under positive bias condition. The FWHM

spectral bandwidth at +3.5V was  $\Delta\lambda/\lambda_p = 27\%$  while FWHM spectral bandwidth at -4.5V was  $\Delta\lambda/\lambda_p = 11\%$ . The E<sub>1</sub>-E<sub>4</sub> transition was dominant at lower positive bias voltage ( $\leq +2.5\text{V}$ ) while the E<sub>1</sub>-E<sub>5</sub> transition was more dominant at higher positive bias voltage ( $\geq +3\text{V}$ ). The responsivity was dramatically increased with increasing bias voltage under positive bias condition. Figure 7.8 shows the spectral responsivity measured at T = 60K for the DB-LGB QWIP under (a) negative and (b) positive bias condition. The peak responsivities at -4.5V and +2.5V were found to be 1.23 A/W at  $\lambda_p = 9.2 \mu\text{m}$  and 2.49A/W at  $\lambda_p = 9.8 \mu\text{m}$ , respectively. Finally, Figure 7.9 shows the spectral responsivity measured at T = 77K for the DB-LGB QWIP under negative bias condition. The peak responsivity at -4V and -3.5V were found to be 0.72 A/W and 0.43 A/W at  $\lambda_p = 9.2 \mu\text{m}$ , respectively.

The detectivity calculation for the BB- and DB-LGB QWIPs was carried out from the measured dark current and the spectral responsivity under background limited performance (BLIP) and non-BLIP. The BLIP detectivity for the BB-LGB QWIP was found to be  $1.3 \times 10^{10} \text{ cm}\cdot\text{Hz}^{1/2}/\text{W}$  at +2.75V, 11.9  $\mu\text{m}$ , and 35K while the non-BLIP detectivity was  $6.9 \times 10^9 \text{ cm}\cdot\text{Hz}^{1/2}/\text{W}$  at -2.45V, 10.1  $\mu\text{m}$ , and 77K. For the DB-LGB QWIP, the BLIP detectivity was  $2.5 \times 10^{10} \text{ cm}\cdot\text{Hz}^{1/2}/\text{W}$  at +3.5V, 9.1  $\mu\text{m}$ , and 35K while the non-BLIP detectivity was  $6.4 \times 10^9 \text{ cm}\cdot\text{Hz}^{1/2}/\text{W}$  at -4V, 9.2  $\mu\text{m}$ , and 77K.

#### 7.4 Conclusions

In this chapter, we have developed an InGaAs/AlGaAs broadband (BB-) linear graded barrier (LGB) quantum well infrared photodetector (QWIP) and a high-sensitivity

AlGaAs/InGaAs/AlGaAs double-barrier (DB-) LGB QWIP for broadband wavelength regime and long-wavelength detection. In the BB-LGB QWIP, the broadband detection was achieved from 6.5 to 16  $\mu\text{m}$  at +2.75V and T = 35K. The wavelength can be tunable with blue-shift under negative bias condition. The maximum responsivity at 11.9  $\mu\text{m}$ , +2.75V, and 35K was 1.75 A/W with BLIP detectivity of  $1.3 \times 10^{10} \text{ cm-Hz}^{1/2}/\text{W}$  and FWHM bandwidth of  $\Delta\lambda/\lambda_p = 52\%$ . For the DB-LGB QWIP, the peak responsivity at  $\lambda_p = 9.1 \mu\text{m}$  was 4.38 A/W at +3.5V and T = 35K. The corresponding BLIP detectivity and FWHM bandwidth were  $2.5 \times 10^{10} \text{ cm-Hz}^{1/2}/\text{W}$  and  $\Delta\lambda/\lambda_p = 27\%$ , respectively. The 20 $\text{\AA}$  AlGaAs double-barrier contributed to the lower dark current and the high sensitivity.

Table 7.1. The complete layer structure of the BB- and DB-LGB QWIP.

Layer		Thickness (Å)	Dopant	Concentration (cm <sup>-3</sup> )
n GaAs (top contact)		3000	Si	2x10 <sup>18</sup>
i Al <sub>x</sub> Ga <sub>1-x</sub> As (x=0.018~0.09)	X 15	500	none	none
n In <sub>0.26</sub> Ga <sub>0.74</sub> As		45	none	7x10 <sup>17</sup>
i Al <sub>x</sub> Ga <sub>1-x</sub> As (x=0.018~0.09)		500	none	none
n GaAs (middle contact)		7000	Si	2x10 <sup>18</sup>
i Al <sub>x</sub> Ga <sub>1-x</sub> As (x=0.018~0.09)	X 15	500	none	none
i Al <sub>0.15</sub> Ga <sub>0.85</sub> As		20	none	none
n In <sub>0.26</sub> Ga <sub>0.74</sub> As		75	Si	7x10 <sup>17</sup>
i Al <sub>0.15</sub> Ga <sub>0.85</sub> As		20	none	none
i Al <sub>x</sub> Ga <sub>1-x</sub> As (x=0.018~0.09)		500	none	none
n GaAs (bottom contact)		5000	Si	2x10 <sup>18</sup>
S.I. GaAs substrate		625 ± 25 μm	none	none

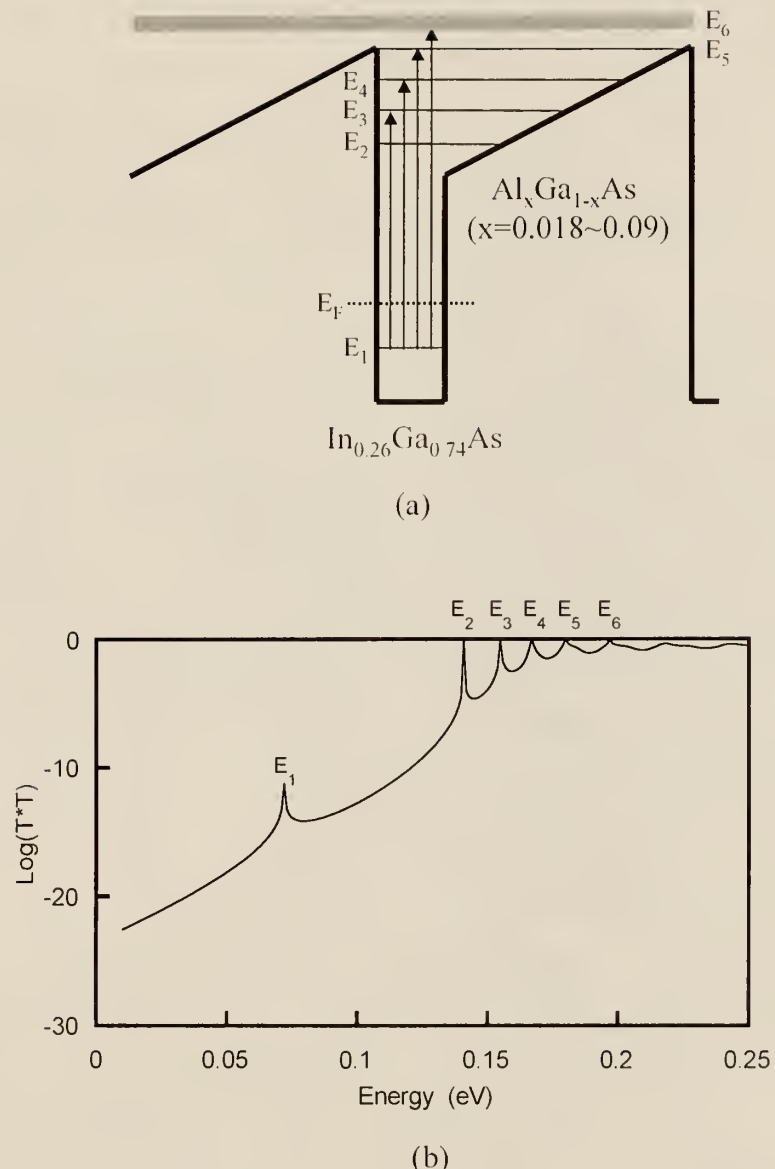


Figure 7.1. (a) The schematic conduction band diagram and (b) the calculated transmission coefficient versus energy at zero bias for the BB-LGB QWIP.

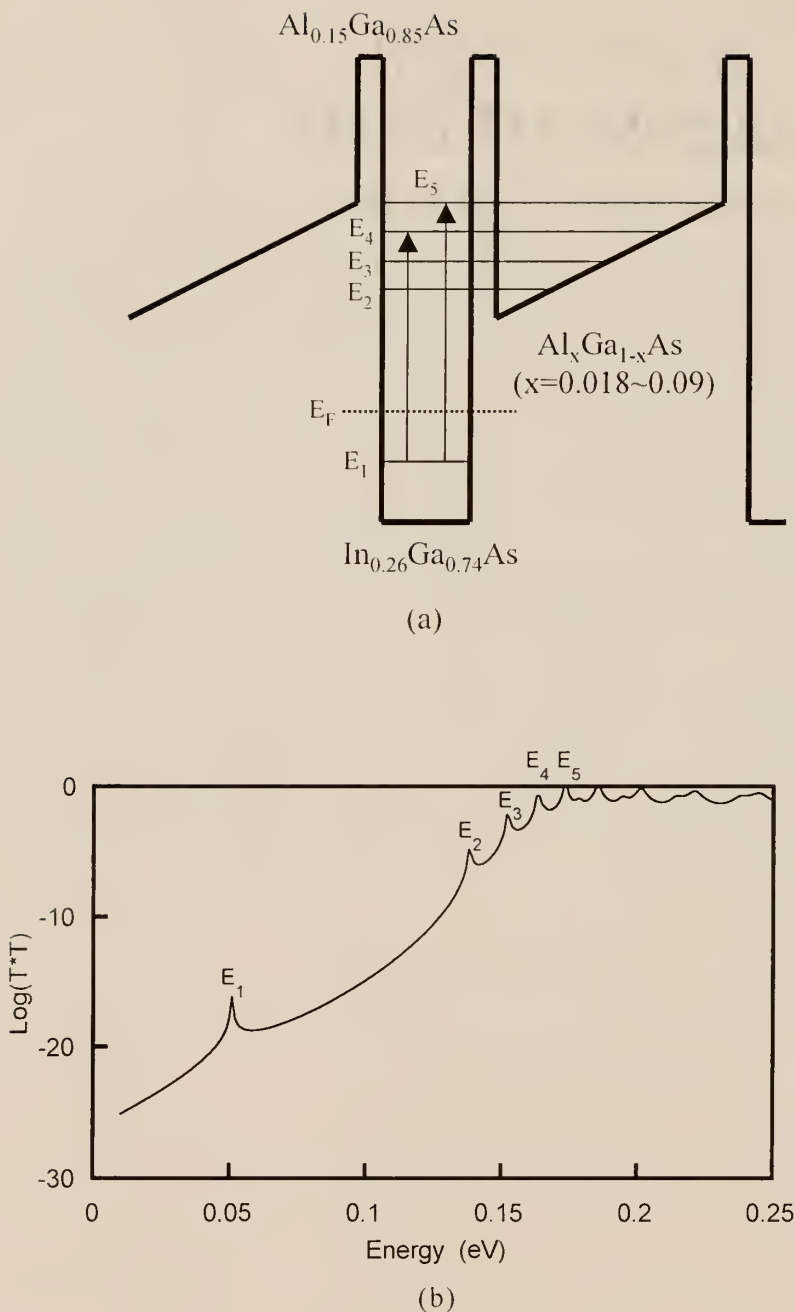


Figure 7.2. (a) The schematic conduction band diagram and (b) the calculated transmission coefficient versus energy at zero bias for the DB-LGB QWIP.

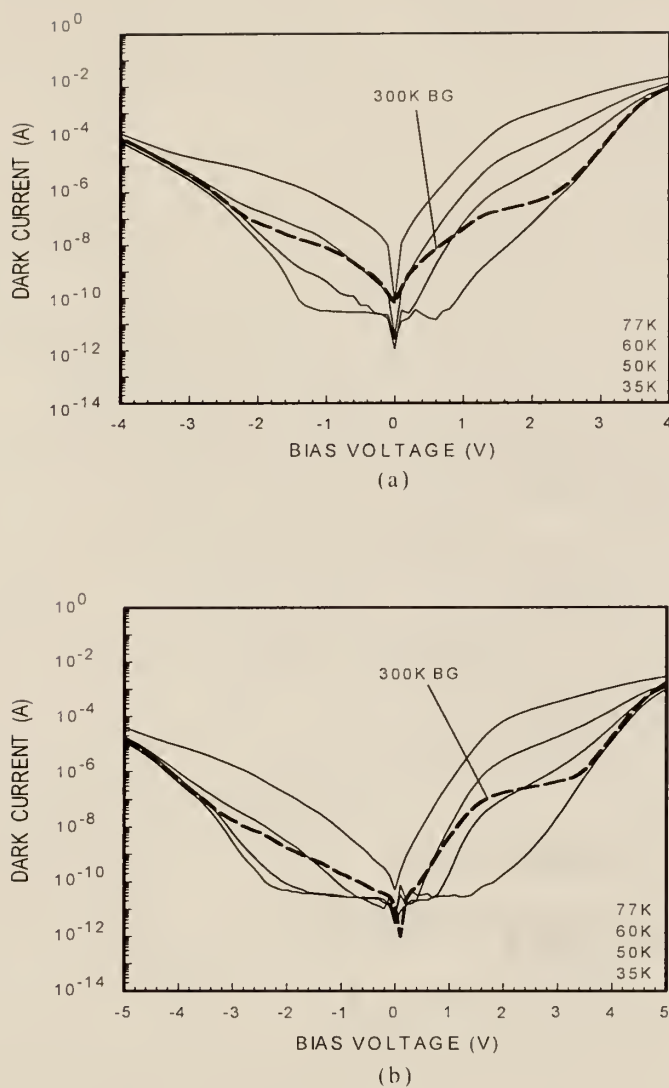


Figure 7.3. The dark current versus bias voltage for (a) the BB-LGB QWIP and (b) the DB-LGB QWIP. The dashed lines is the 300K background window current.

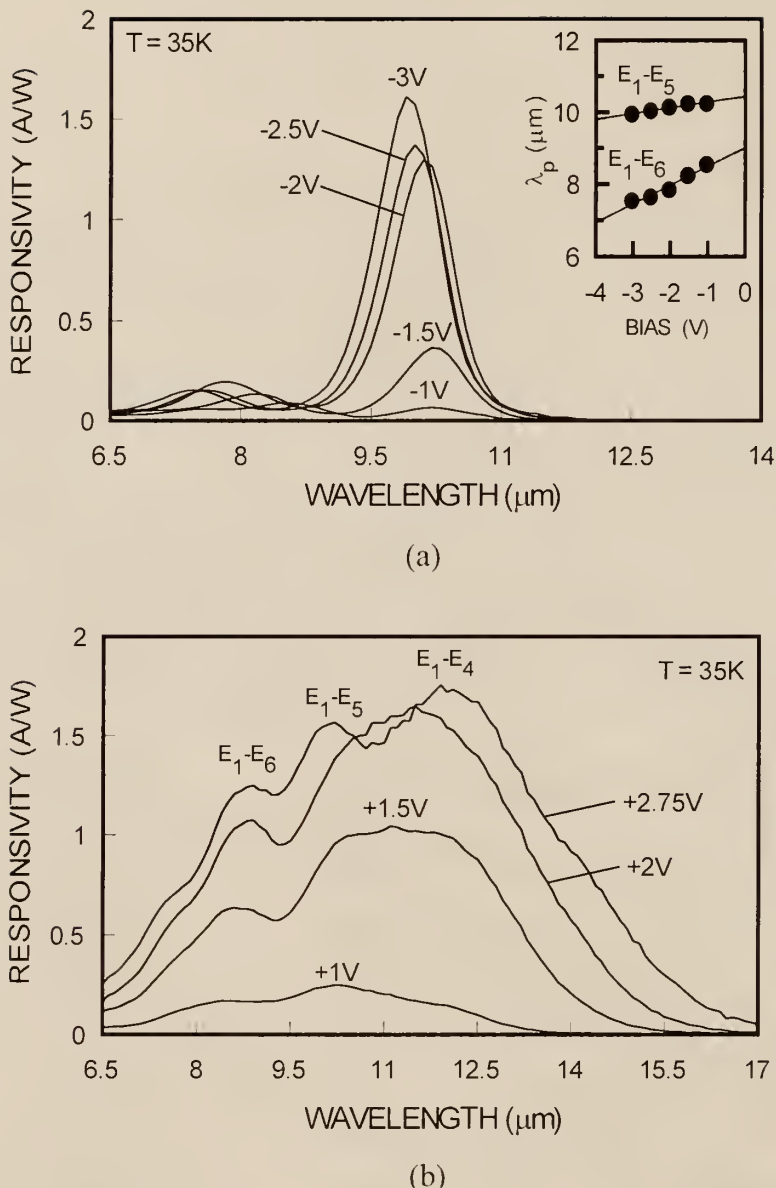


Figure 7.4. The spectral responsivity of the BB-LGB QWIP device at  $T = 35K$ : (a) at negative and (b) positive bias condition.

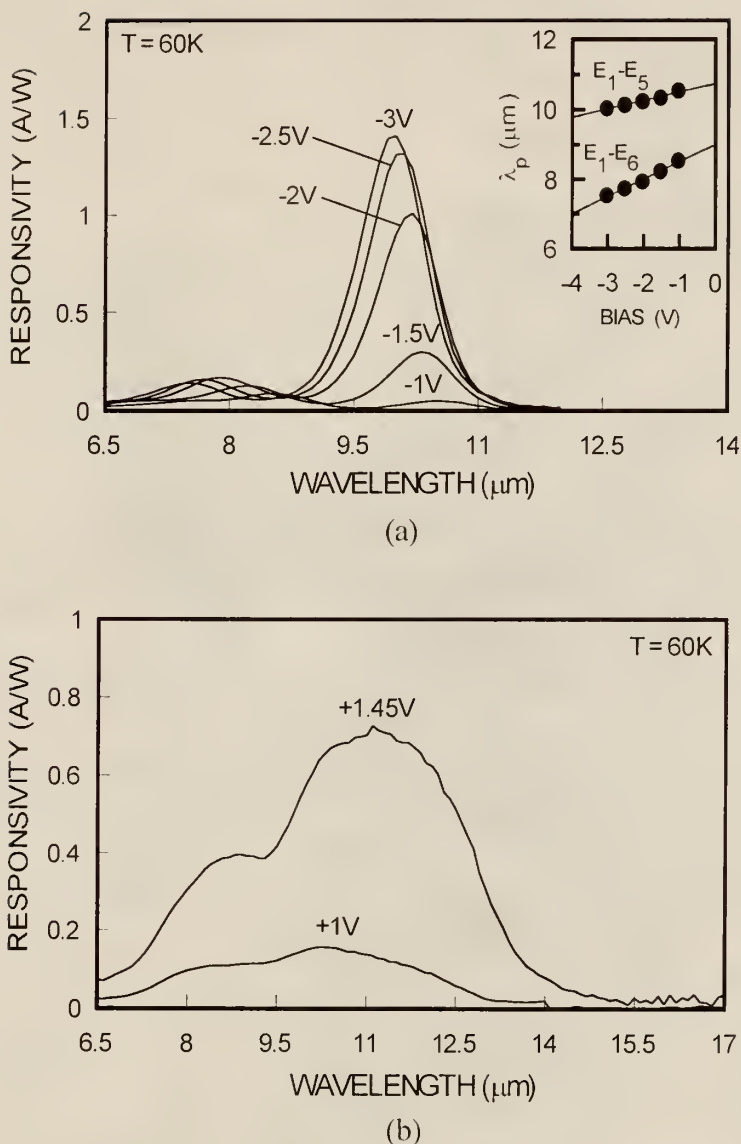


Figure 7.5. The spectral responsivity of the BB-LGB QWIP device at  $T = 60\text{K}$ : (a) at negative and (b) positive bias condition.

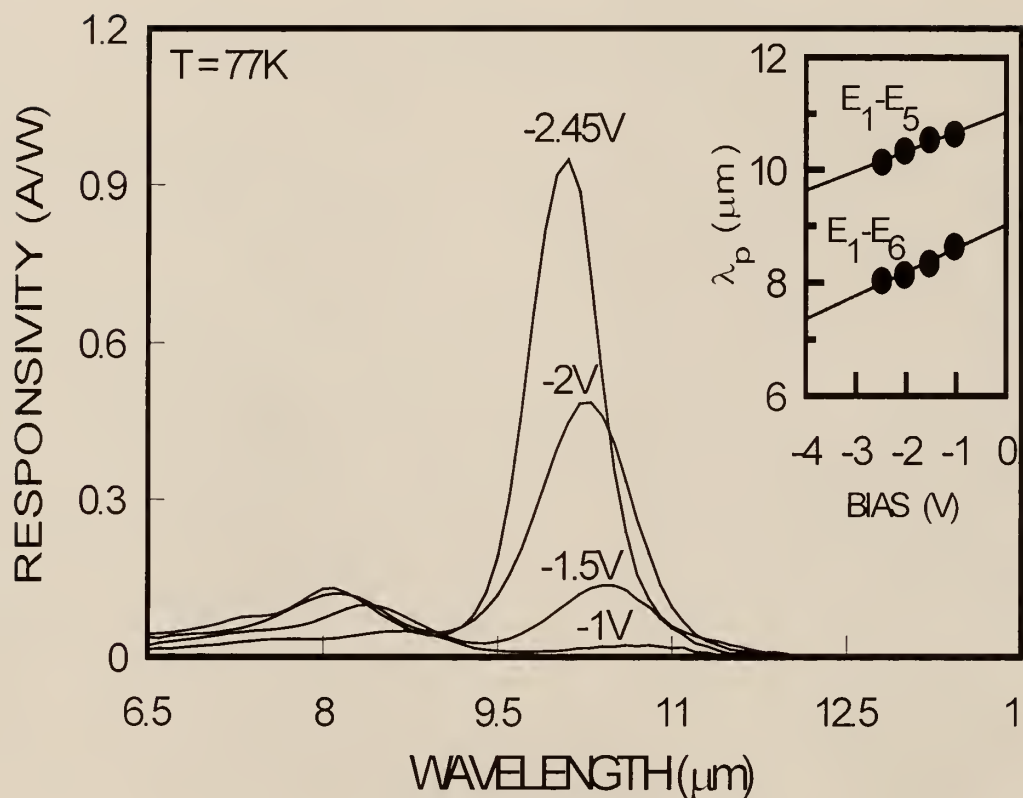


Figure 7.6. The spectral responsivity of the BB-LGB QWIP device at  $T = 77\text{K}$  under negative bias condition.

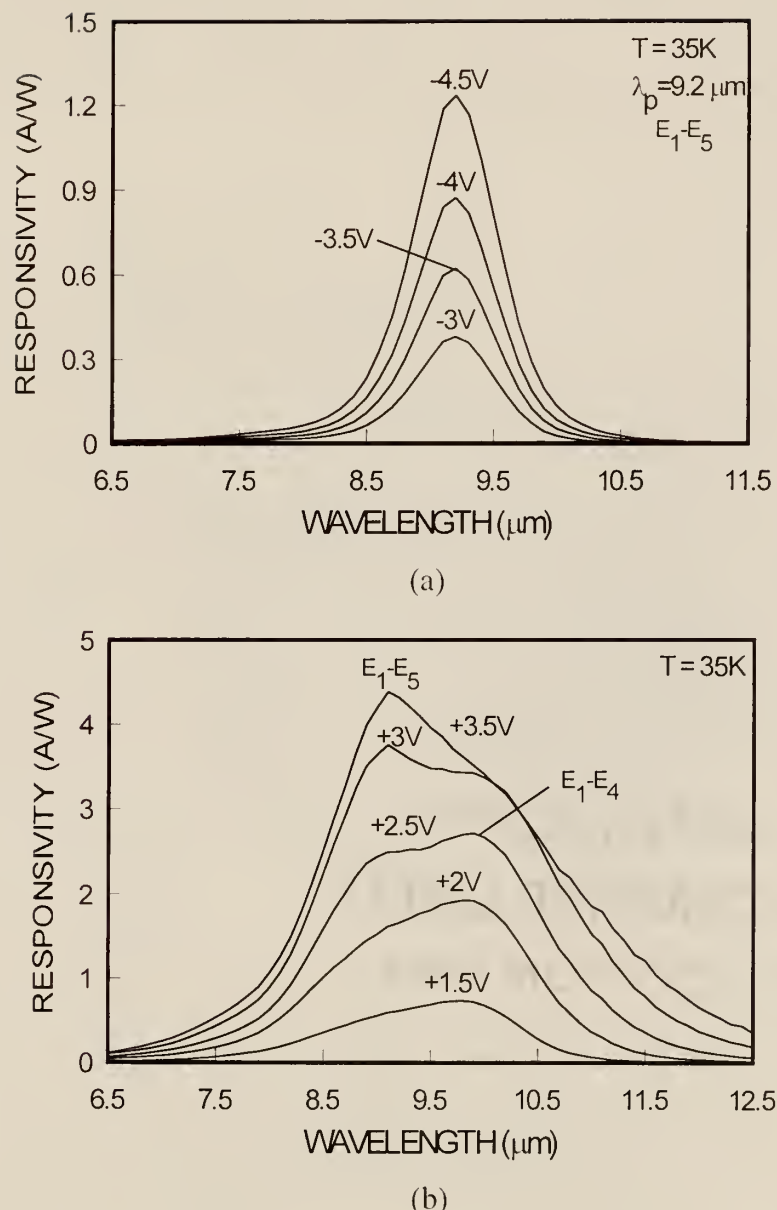


Figure 7.7. The spectral responsivity of the DB-LGB QWIP device at  $T = 35K$ : (a) at negative and (b) positive bias condition.

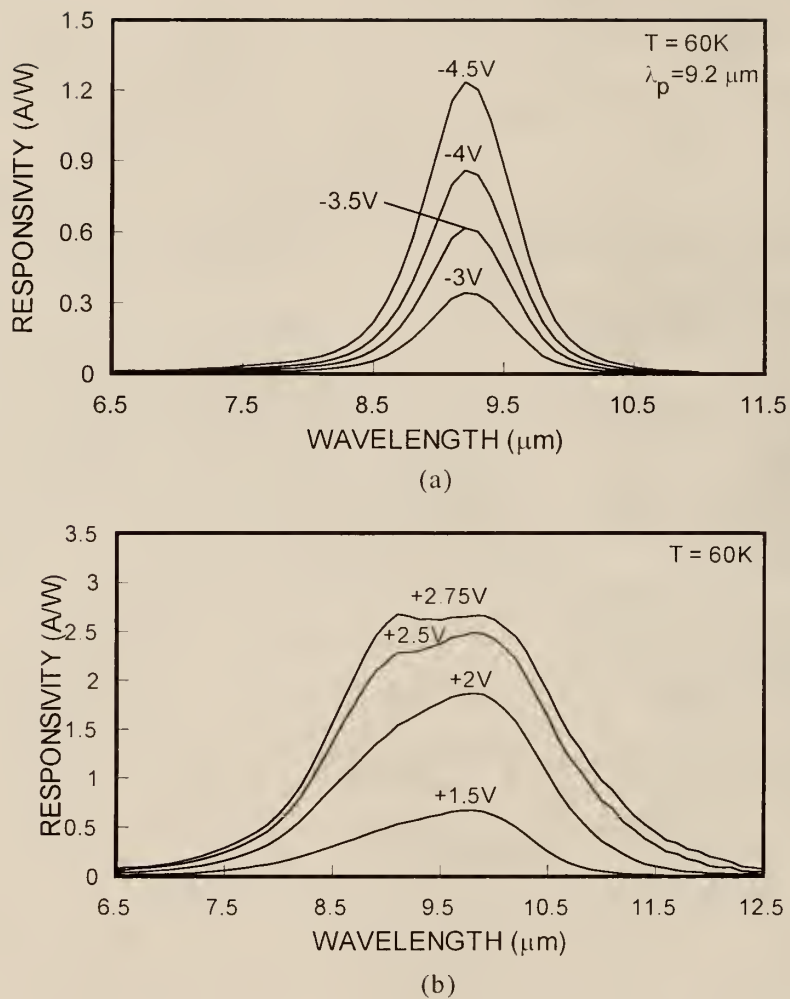


Figure 7.8. The spectral responsivity of the DB-LGB QWIP device at  $T = 60\text{K}$ : (a) at negative and (b) positive bias condition.

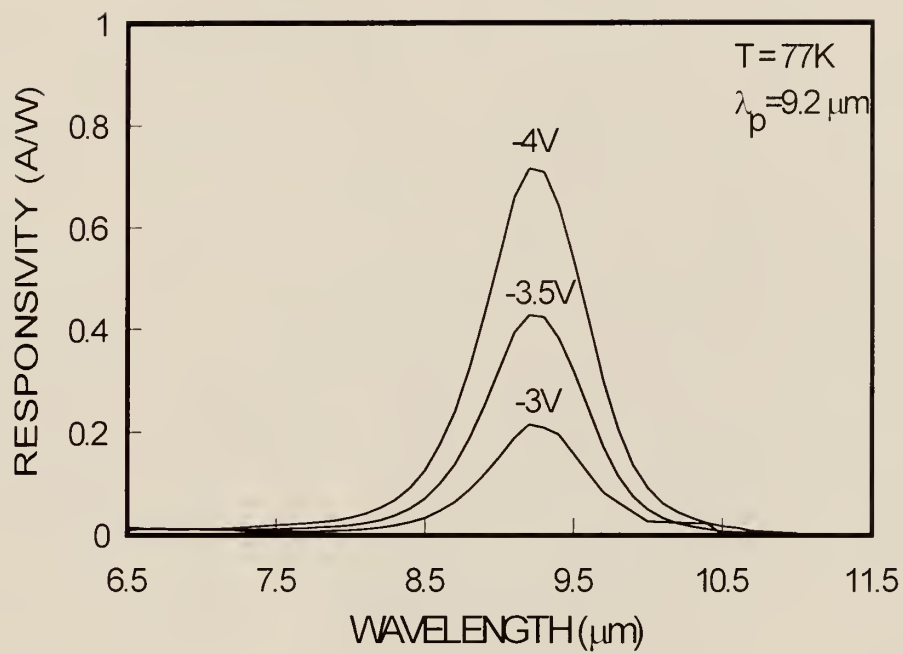


Figure 7.9. The spectral responsivity of the DB-LGB QWIP device at  $T = 77\text{K}$  under negative bias condition.

## CHAPTER 8

### THREE-COLOR THREE-STACK QUANTUM WELL INFRARED PHOTODETECTOR 4 x 4 FOCAL PLANE ARRAYS

#### 8.1 Introduction

Recently, there have been great interests in developing the quantum well infrared photodetectors (QWIPs) for the multi-color detection and the large focal plane array (FPA). For multi-color detection in QWIP structure, there are mainly two approaches in which one is to use the multi-stack structure [10,11,74] and the other is the asymmetrical QWIP structure. The multi-color detection is highly desired in some practical applications such as the discrimination and identification of the target. The mature of the QWIP growth technique such as molecular beam epitaxy (MBE) make it possible. J. C. Chiang *et al.* [54] has successfully demonstrated two-stack multi-color QWIP for MWIR and LWIR dual-band detection, and voltage tunable multi-color triple-coupled (TC-) QWIP for LWIR detection. Focal plane array (FPA) in IR imaging system has many applications such as night vision, early warning system, monitoring the temperature profiles, target detection, and discrimination. While single-color FPA is useful for distinct targets, multicolor FPA with two or more spectral bands can improve the overall performance when the targets are not clear [103]. Therefore, the advanced FPA requires a simultaneous multicolor response in SWIR, MWIR, LWIR, or VLWIR bandwidths. Recently, the large 640 x 486 GaAs/AlGaAs FPA with 9  $\mu\text{m}$  cutoff wavelength and two-color large 640 x 486 GaAs/AlGaAs FPA for LWIR and VLWIR regions have been

developed [17,104]. In addition, the 256 x 256 two-color MW/LW QWIP FPA with pixel registration and simultaneous integration has been demonstrated [105]. Finally, the large format and high uniformity QWIP focal plane array (FPA) cameras have been successfully developed for IR imaging applications [106-107].

In this chapter, we have designed and demonstrated two three-color, three-stack QWIP 4 x 4 focal plane arrays (FPAs) grown on semi-insulating (SI) GaAs substrate.

## 8.2 Device Design and Fabrication

The two (LW/LW/MW and LW/MW/SW) three-color, three-stack QWIP 4 x 4 FPAs were grown on semi-insulating GaAs substrate. For the first QWIP 4 x 4 FPA of LW/LW/MW three-color detection, the top-stack for LWIR detection ( $\lambda_p \approx 12 \mu\text{m}$ ) consists of 62Å In<sub>0.23</sub>Ga<sub>0.77</sub>As quantum well (Si-doped to  $7 \times 10^{17} \text{ cm}^{-3}$ ) separated by 500Å thick undoped GaAs barrier as a period, which was repeated 5 times. The middle-stack for LWIR detection ( $\lambda_p \approx 8.8 \mu\text{m}$ ) was formed by a 62Å In<sub>0.23</sub>Ga<sub>0.77</sub>As quantum well (Si-doped to  $7 \times 10^{17} \text{ cm}^{-3}$ ) and a 300Å Al<sub>0.11</sub>Ga<sub>0.89</sub>As barrier as a unit cell in which a very thin GaAs (5Å) was inserted between quantum well and barrier. This unit cell was repeated 5 times. The five-period MWIR QWIP structure for bottom-stack consists of a 25Å In<sub>0.35</sub>Ga<sub>0.65</sub>As quantum well (Si-doped to  $2 \times 10^{18} \text{ cm}^{-3}$ ) and a 300Å Al<sub>0.38</sub>Ga<sub>0.62</sub>As quantum well as a unit cell in which a very thin GaAs (5Å) was also grown between quantum well and barrier. Each stack was surrounded by the undoped 500Å GaAs spacer layers, which can contribute to the lower dark current. The ohmic contact layers (4500Å, Si-doped to  $2 \times 10^{18} \text{ cm}^{-3}$ ) were grown on top of top-stack, bottom of bottom-stack, and between top- and middle-stacks. Finally, the p-type Al<sub>0.38</sub>Ga<sub>0.62</sub>As buffer layer (3000Å,

Be-doped to  $1 \times 10^{16} \text{ cm}^{-3}$ ) sandwiched by two ohmic contact layers was grown between middle- and bottom-stacks. Table 8.1 shows the complete layer structure for this LW/LW/MW three-stack, three-color QWIP 4 x 4 FPA. The second three-color, three-stack QWIP 4 x 4 FPA can detect the three different bands of LW, MW, and SW wavelength regimes. The top-stack for LWIR detection ( $\lambda_p \cong 7.9 \mu\text{m}$ ) consists of 62Å  $\text{In}_x\text{Ga}_{1-x}\text{As}$  ( $x=0.23\pm0.01$ ) quantum well (Si-doped to  $7 \times 10^{17} \text{ cm}^{-3}$ ) separated by 300Å undoped  $\text{Al}_x\text{Ga}_{1-x}\text{As}$  ( $x=0.11\pm0.01$ ) barrier as a unit cell in which a very thin layer was inserted between quantum well and barrier and the unit cell was repeated 5 times. The middle-stack for MWIR detection ( $\lambda_p \cong 3.7 \mu\text{m}$ ) was formed by a 25Å  $\text{In}_x\text{Ga}_{1-x}\text{As}$  ( $x=0.35\pm0.01$ ) quantum well (Si-doped to  $2.5 \times 10^{18} \text{ cm}^{-3}$ ) and a 300Å undoped  $\text{Al}_x\text{Ga}_{1-x}\text{As}$  ( $x=0.38\pm0.01$ ) barrier as a unit cell in which a very thin GaAs (5Å) was also inserted between quantum well and barrier as described in the top-stack. This unit cell was also repeated 5 times. The unit cell of the bottom-stack with 10-period for SWIR detection consists of 500Å  $\text{Al}_x\text{Ga}_{1-x}\text{As}$  ( $x=0.80\pm0.01$ ) indirect-barrier (IB) and 24Å  $\text{In}_x\text{Ga}_{1-x}\text{As}$  ( $x=0.37\pm0.01$ ) quantum well (Si-doped to  $2 \times 10^{18} \text{ cm}^{-3}$ ) with 5Å GaAs thin layer between quantum well and barrier. Each stack except for bottom-stack was surrounded by the undoped 500Å GaAs spacer layers. The ohmic contact layers (4500Å) were grown on top of top-stack (Si-doped to  $2 \times 10^{18} \text{ cm}^{-3}$ ), bottom of bottom-stack (Si-doped to  $2 \times 10^{18} \text{ cm}^{-3}$ ), and between top- and middle-stacks (Si-doped to  $3 \times 10^{18} \text{ cm}^{-3}$ ). Finally, the  $\text{Al}_x\text{Ga}_{1-x}\text{As}$  ( $x=0.38\pm0.01$ ) buffer layer (3000Å) sandwiched by two ohmic contact layers (Si-doped to  $3 \times 10^{18} \text{ cm}^{-3}$ ) was grown between middle- and bottom-stacks. Table 8.2 shows the complete layer structure for this LW/MW/SW three-stack, three-color QWIP 4 x 4 FPA. Figure 8.1 shows the schematic conduction band diagrams of the first

LW/LW/MW QWIP 4 x 4 FPA for (a) top-stack, (b) middle-stack, and (c) bottom-stack. Figure 9.2 shows the schematic conduction band diagrams of the second LW/MW/SW QWIP 4 x 4 FPA for (a) LWIR, (b) MWIR, and (c) SWIR QWIPs, respectively. The intersubband transition schemes of LWIR QWIP stacks for both LW/LW/MW and LW/MW/SW QWIP 4 x 4 FPAs were bound-to-quasi-bound (BTQB) while MWIR QWIP stacks employed bound-to-continuum (BTC) transition schemes. The bottom-stack of the LW/MW/SW QWIP 4 x 4 FPA used the indirect-barrier (IB) with very high barrier height required for SWIR detection.

These two three-color, three-stack QWIP structures were fabricated to the 4 x 4 focal plane array (FPA) with a pixel size ( $100 \times 100 \mu\text{m}^2$ ) by using wet etching and photolithography procedure. The seven masks are required to process the complete three-color, three-stack QWIP 4 x 4 FPA devices. The mesa structure for top-stack detector was first etched from top contact layer onto middle contact layer (1) by using MESA 1 mask. Secondly, the mesa structure for middle-stack detector was etched from middle contact layer (1) onto middle contact layer (2) by using MESA 2 mask. Figure 8.3 shows the top-views of mesa structure for three-color, three-stack QWIP 4 x 4 FPA: (a) after etching of top-stack and (b) after etching of top- and middle-stack. Next, the mesa structure for the buffer layer was etched from middle contact layer (2) onto middle contact layer (3) by using MESA 3 mask. The bottom-stack QWIP structure was etched from contact layer (3) onto bottom contact layer by using MESA 4 mask. Figure 8.4 shows the top-views of mesa structure for three-color, three-stack QWIP 4 x 4 FPA: (a) after etching for top-, middle-, and buffer-stack, and (b) after etching for top-, middle-, buffer, and bottom-stack. The MESA 5 mask was used to etch from bottom contact layer

(3) onto semi-insulating GaAs substrate for isolations between 4 x 4 FPAs. The ISOLATION mask was used for the passivation layer ( $\text{Si}_3\text{N}_4$ ) to cover the whole device area except the area for electrical connection. Figure 8.5 shows the top-views of mesa structure for three-color, three-stack QWIP 4 x 4 FPA: (a) after etching for top-stack, middle-, buffer-, bottom-, and ohmic contact-stack, and (b) after passivation layer (gray area) evaporation on the etched mesa structure (the white areas are opened for the ohmic contact metalization). Finally, the ohmic contact pattern (AuGe/Ag/Au) was deposited by METAL mask and then annealed at  $T = 450^\circ\text{C}$  for 2 minutes. Figure 8.6 shows the final top-view of three-color, three-stack QWIP 4 x 4 FPA: after ohmic contact metalization evaporation (the dark areas are bonding pads and interconnect lines, and the gray area is passivation layer). Figure 8.7 shows (a) the cross section view and (b) the three-dimensional (3-D) view of a detector pixel for three-color, three-stack QWIP 4 x 4 FPA.

### 8.3 Results and Discussion

The 4 x 4 array detectors was polished to  $45^\circ$  facet on the back side of the substrate for coupling the incident IR radiation into the active layers of the FPA detectors. The 4 x 4 FPAs were bonded on the TO-8 can and then mounted in the closed cycle cryogenic system for low operating temperature. The spectral photoresponse was measured by using a 1/8 monochromater, a calibrated blackbody IR source ( $T=1000^\circ\text{C}$ ) at 200 Hz chopped frequency, and Oxford CCC1204 closed cycle liquid helium cryostat. The results of the dark I-V and spectral responsivity measurements for these two QWIP 4 x 4 FPAs are described in this section.

### 8.3.1 LW/LW/MW QWIP 4 x 4 FPA

Figure 8.8, 8.9, and 8.10 show the dark current versus bias voltage (I-V) curves of top-stack (LWIR-QWIP), middle-stack (LWIR-QWIP), and bottom-stack (MWIR-QWIP) for the LW/LW/MW QWIP 4 x 4 FPA, respectively. The dark current of the two LWIR-QWIP stacks is several orders of magnitude higher than the MWIR-QWIP (bottom-stack) because the dark current is dependent of the barrier height. The dark current of the MWIR-QWIP stack is slowly increased with the increasing temperature up to T=100K. However, the dark current was dramatically increased with the increasing temperature in temperature range over T=120K as shown in Figure 8.10. The slight asymmetric dark current characteristics can be attributed to the doping migration into the barrier layers.

The spectral photoresponse measurement was carried out for each stack. Figure 8.11 shows the responsivity measured at T = 40K for top-stack (LWIR-QWIP) at (a) negative and (b) positive biases. The peak responsivity were found to be 0.5 A/W at  $V_b = -1.25V$  with a peak of  $\lambda_p = 11.9 \mu\text{m}$  and 0.77 A/W at  $V_b = +1V$  and  $\lambda_p = 12.1 \mu\text{m}$ . The peak wavelengths were slightly different on the polarity of the applied bias voltage. The maximum responsivity at T = 77K for the middle-stack LWIR-QWIP was 0.13 A/W at  $V_b = -1.5V$  and  $\lambda_p = 8.8 \mu\text{m}$ . Figure 8.12 shows the measured spectral responsivity for this middle-stack LWIR-QWIP at (a) negative and (b) positive biases. The peak responsivity was linearly increased with the increasing bias voltages. Figure 8.13 shows the measured spectral responsivity for the bottom-stack MWIR-QWIP. This stack can be operative up to T = 180K. The maximum responsivity was 0.12 A/W with a peak wavelength of 4.2  $\mu\text{m}$  at  $V_b = -4V$  and T = 77K.

The detectivity was calculated by using the results of the dark current and spectral responsivity measurement. The non-background limited performance (non-BLIP) detectivity for the top-stack LWIR-QWIP was  $1.94 \times 10^{10}$  cm-Hz $^{1/2}$ /W at  $V_b = -0.7V$ ,  $T = 40K$ , and  $\lambda_p = 11.9 \mu m$  while the non-BLIP detectivity for the middle-stack LWIR-QWIP was  $3.93 \times 10^{10}$  cm-Hz $^{1/2}$ /W at  $V_b = -1V$ ,  $T = 77K$ , and  $\lambda_p = 8.8 \mu m$ . The non-BLIP detectivity for the bottom-stack MWIR-QWIP at  $T = 77$  and  $180K$  were  $2.54 \times 10^{10}$  and  $6.73 \times 10^9$  cm-Hz $^{1/2}$ /W at  $V_b = -2.5V$  and  $\lambda_p = 8.8 \mu m$ , respectively. Figure 8.20 (a) shows the normalized spectral responsivity for this three-color, three-stack LW/LW/MW QWIP 4 x 4 FPA, which has three identical peaks in two bands for multi-color detection.

### 8.3.2 LW/MW/SW QWIP 4 x 4 FPA

Figure 8.14 and 8.15 shows the dark current versus bias voltage (I-V) curves measured at  $T = 40, 77$ , and  $100K$  for the LWIR-QWIP (top-stack) and at  $T = 77, 100, 150$ , and  $200K$  for the MWIR-QWIP (middle-stack) of the LW/MW/SW QWIP 4 x 4 FPA, respectively. Figure 8.16 shows the dark current versus bias voltage (I-V) measured at  $T = 40, 60, 77$ , and  $90K$  for the SWIR-QWIP (bottom-stack) of the LW/MW/SW QWIP 4 x 4 FPA. The dark current for the bottom-stack is higher than those of normal MWIR or SWIR-QWIPs because the X-valley barrier is much lower than  $\Gamma$ -valley barrier in the  $Al_{0.8}Ga_{0.2}As$  barrier region.

The maximum responsivity for the top-stack LWIR-QWIP at  $T = 77K$  was  $0.29 A/W$  ( $\lambda_p = 7.8 \mu m$ ) at  $V_b = +2V$  and  $0.18 A/W$  ( $\lambda_p = 7.9 \mu m$ ) at  $V_b = -2.5V$ . Figure 8.17 (a) and (b) show the spectral responsivity measured at  $T = 77K$  under (a) negative and (b) positive biases. The spectral responsivity for the middle-stack MWIR-QWIP was

measured up to T = 200K. Figure 8.18 shows the measured responsivity for this MWIR-QWIP at (a) T = 77K and (b) T = 100K. The peak wavelength was  $\lambda_p = 3.7 \mu\text{m}$  independent of the applied bias voltage and the operating temperature. The peak responsivity at  $V_b = +4\text{V}$  and  $\lambda_p = 3.7 \mu\text{m}$  was found to be 0.23 A/W at T = 77K and 0.24 A/W at T = 100K. The bottom-stack of this LW/MW/SW QWIP 4 x 4 FPA was the SWIR-QWIP using the indirect-barrier (IB). The short-wavelength detection as short as 2.4  $\mu\text{m}$  is attributed to the very high Al<sub>0.8</sub>Ga<sub>0.2</sub>As  $\Gamma$ -valley barrier. As shown in Figure 8.2 (c), the solid lines and the dotted lines are the  $\Gamma$ -valleys and X-valleys for each layer, respectively. An electron can be excited by the transition from  $E_1^\Gamma$  to  $E_c^\Gamma$  for short-wavelength detection. The photo-excited electron will be soon scattered into X-valley of the Al<sub>0.8</sub>Ga<sub>0.2</sub>As barrier and then tunnel through the GaAs/InGaAs X-valleys barriers to be efficiently collected as photocurrent. It is required that the scattering time from  $\Gamma$ -valley to X-valley and the tunneling time through the GaAs/InGaAs X-valley barriers are much shorter than  $\Gamma$ -valley hot electron lifetime and the recapture time into the GaAs/InGaAs  $\Gamma$ -valley quantum well, respectively. Figure 8.19 shows the spectral responsivity measured at T = 77K for this IB-SWIR QWIP under negative and positive bias conditions. The peak responsivity at -4.5V and +4.5V were found to be 0.021 A/W and 0.014 A/W with a peak wavelength of 2.4  $\mu\text{m}$  at T = 77K, respectively. The peak wavelength at 2.4  $\mu\text{m}$  was independent of the applied bias voltage.

The non-BLIP detectivity for three-stack QWIP was estimated by using the measurement results. The peak responsivity for the top-stack LWIR-QWIP at T = 77K was  $3.21 \times 10^{10} \text{ cm}\cdot\text{Hz}^{1/2}/\text{W}$  at  $V_b = +1.5\text{V}$  and  $\lambda_p = 7.8 \mu\text{m}$ . The corresponding product of the quantum efficiency and the photoconductive gain was 0.018. The peak detectivity

of  $4.89 \times 10^{10}$  cm-Hz<sup>1/2</sup>/W was obtained at  $V_b = -4V$ ,  $T = 77K$ , and  $\lambda_p = 3.7 \mu m$  for the middle-stack MWIR-QWIP. The detectivity for the bottom-stack SWIR-QWIP was low as much as  $5.89 \times 10^8$  cm-Hz<sup>1/2</sup>/W at  $V_b = -5V$ ,  $T = 77K$ , and  $\lambda_p = 2.4 \mu m$  which is due to the high dark current and low spectral responsivity. Figure 8.20 (b) shows the normalized spectral responsivity for this three-color, three-stack LW/MW/SW QWIP 4 x 4 FPA, which has three identical peaks in three bands for multi-color detection.

#### 8.4 Conclusions

We have developed two three-color, three-stack quantum well infrared photodetector (QWIP) 4 x 4 focal plane arrays (FPAs) with a pixel size of  $100 \times 100 \mu m^2$  using InGaAs/GaAs and InGaAs/GaAs/AlGaAs material systems. The first LW/LW/MW FPA can detect two peaks in LWIR wavelength region and a peak in MWIR wavelength region. The truly three-color detection in three bands was observed in the second LW/MW/SW QWIP 4 x 4 FPA. The peak wavelengths for the LW/LW/MW FPA were 12, 8.8, and  $4.2 \mu m$  while the peak wavelengths of 7.9, 3.7, and  $2.4 \mu m$  was obtained in the LW/MW/SW FPA. Success in this 4 x 4 FPA will lead the larger format FPA. The study for readout integrated circuit (ROIC) is of prime important for the larger format FPA characterization.

Table 8.1. The layer structure of the LW/LW/MW QWIP 4 x 4 FPA.

Layer		Thickness (Å)	Dopant	Concentration (cm <sup>-3</sup> )
n GaAs (top contact)		4500	Si	2x10 <sup>18</sup>
i GaAs (spacer layer)		500	none	none
i GaAs	X 5	500	none	none
n In <sub>0.23</sub> Ga <sub>0.77</sub> As		62	Si	7x10 <sup>17</sup>
i GaAs (spacer layer)		1000	none	none
n GaAs (middle contact 1)		4500	Si	2x10 <sup>18</sup>
i GaAs (spacer layer)		500	none	none
i Al <sub>0.11</sub> Ga <sub>0.89</sub> As	X 5	300	none	none
i GaAs		5	none	none
n In <sub>0.23</sub> Ga <sub>0.77</sub> As		62	Si	7x10 <sup>17</sup>
i GaAs		5	none	none
i Al <sub>0.11</sub> Ga <sub>0.89</sub> As		300	none	none
i GaAs (spacer layer)		500	none	none
n GaAs (middle contact 2)		4500	Si	2x10 <sup>18</sup>
p Al <sub>0.38</sub> Ga <sub>0.62</sub> As (isolation layer)		3000	Be	1x10 <sup>16</sup>
n GaAs (middle contact 3)		4500	Si	2x10 <sup>18</sup>
i Al <sub>0.38</sub> Ga <sub>0.62</sub> As	X 5	300	none	none
i GaAs		5	none	none
n In <sub>0.35</sub> Ga <sub>0.65</sub> As		25	Si	2x10 <sup>18</sup>
i GaAs		5	none	none
i Al <sub>0.38</sub> Ga <sub>0.62</sub> As		300	none	none
i GaAs		500	none	none
n GaAs (bottom contact)		4500	Si	2x10 <sup>18</sup>
S.I. GaAs substrate		625 ± 25 μm	none	none

Table 8.2. The layer structure of the LW/MW/SW QWIP 4 x 4 FPA.

Layer		Thickness (Å)	Dopant	X	Concentration (cm <sup>-3</sup> )
n GaAs (top contact)		4500	Si		2x10 <sup>18</sup>
i GaAs (spacer layer)		500	none		none
i Al <sub>x</sub> Ga <sub>1-x</sub> As	X 5	300	none	0.11±0.01	none
i GaAs		5	none		none
n In <sub>x</sub> Ga <sub>1-x</sub> As		62	Si	0.25±0.01	7x10 <sup>17</sup>
i GaAs		5	none		none
i Al <sub>x</sub> Ga <sub>1-x</sub> As		300	none	0.11±0.01	none
i GaAs (spacer layer)		500	none		none
n GaAs (middle contact 1)		4500	Si		3x10 <sup>18</sup>
i GaAs (spacer layer)		500	none		none
i Al <sub>x</sub> Ga <sub>1-x</sub> As	X 5	300	none	0.38±0.01	none
i GaAs		5	none		none
n In <sub>x</sub> Ga <sub>1-x</sub> As		25	Si	0.35±0.01	2.5x10 <sup>18</sup>
i GaAs		5	none		none
i Al <sub>x</sub> Ga <sub>1-x</sub> As		300	none	0.38±0.01	none
i GaAs (spacer layer)		500	none		none
n GaAs (middle contact 2)		4500	Si		3x10 <sup>18</sup>
p Al <sub>x</sub> Ga <sub>1-x</sub> As		3000	none	0.38±0.01	none
n GaAs (middle contact 3)		4500	Si		3x10 <sup>18</sup>
i Al <sub>x</sub> Ga <sub>1-x</sub> As	X 10	500	none	0.80±0.01	none
i GaAs		5	none		none
n In <sub>x</sub> Ga <sub>1-x</sub> As		24	Si	0.37±0.01	3x10 <sup>18</sup>
i GaAs		5	none		none
i Al <sub>x</sub> Ga <sub>1-x</sub> As		500	none	0.80±0.01	none
n GaAs (bottom contact)		4500	Si		2x10 <sup>18</sup>
S.I. GaAs substrate		625 ± 25 μm	none		none

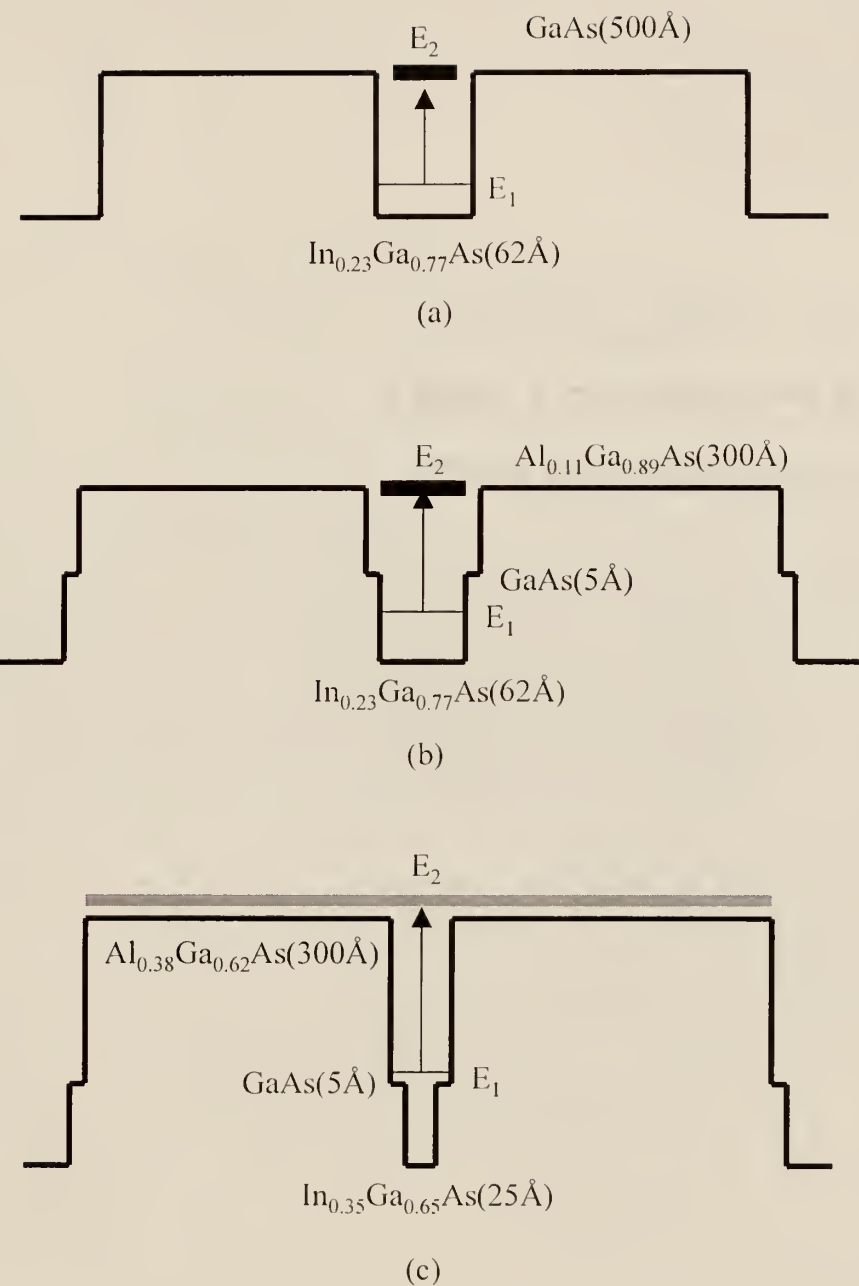


Figure 8.1. The schematic conduction band diagrams and intersubband transitions for LW/LW/MW QWIP 4 x 4 FPA: (a) top-stack (LW), (b) middle-stack (LW), and (c) bottom-stack (MW)

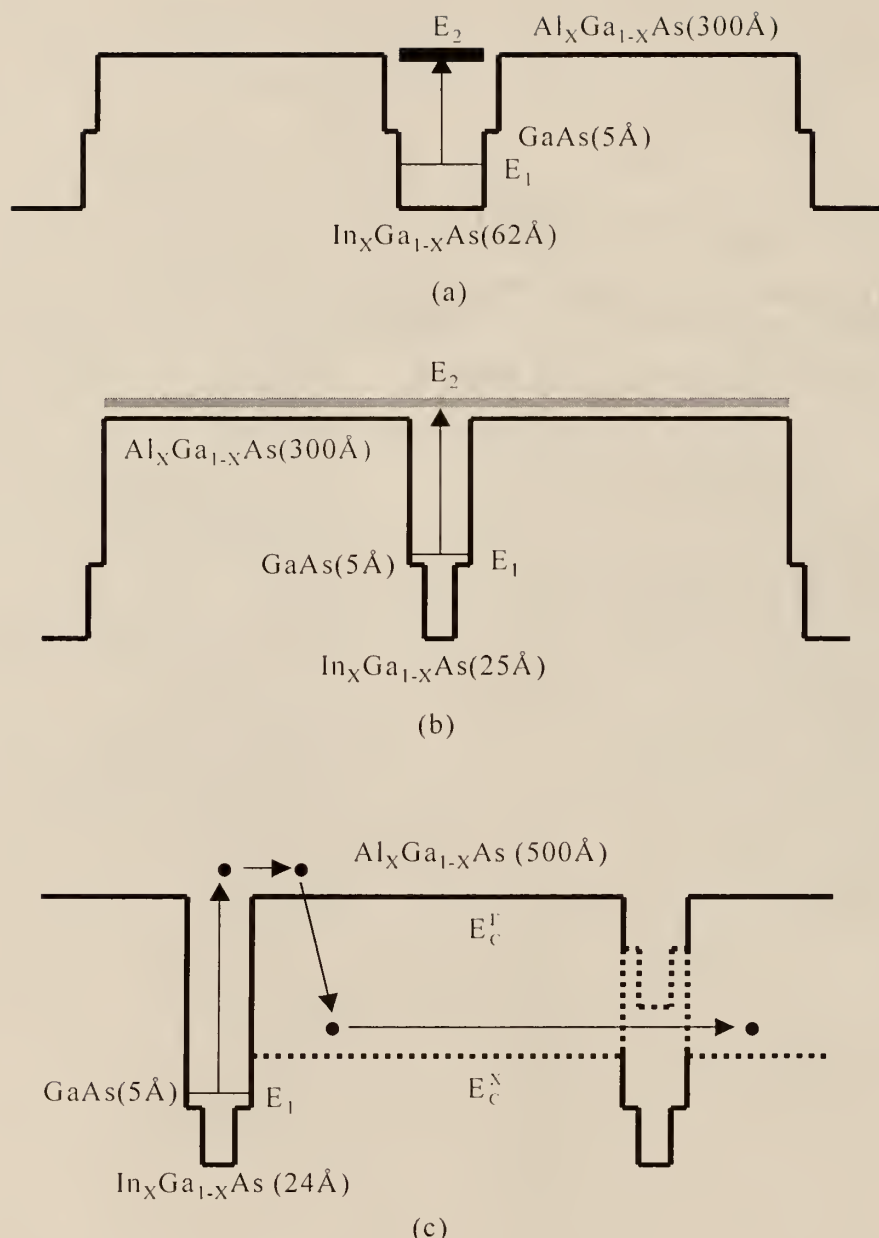
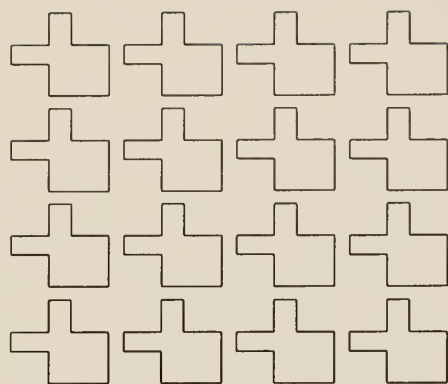
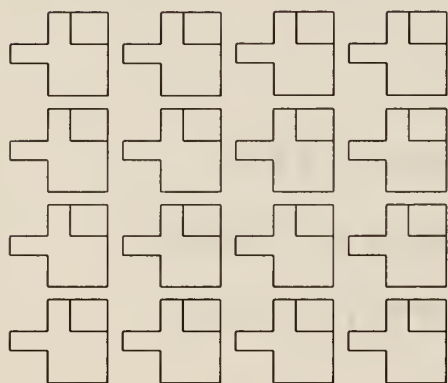


Figure 8.2. The schematic conduction band diagrams and intersubband transitions for LW/LW/MW QWIP 4 x 4 FPA: (a) top-stack (LW), (b) middle-stack (MW), and (c) bottom-stack (SW)

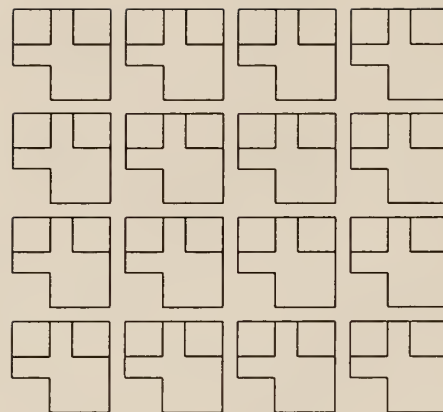


(a)

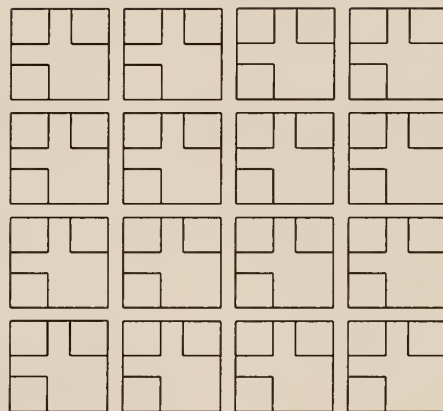


(b)

Figure 8.3. The top-views of mesa structure for three-color, three-stack QWIP 4 x 4 FPA:  
(a) after etching of top-stack and (b) after etching of top- and middle-stack.

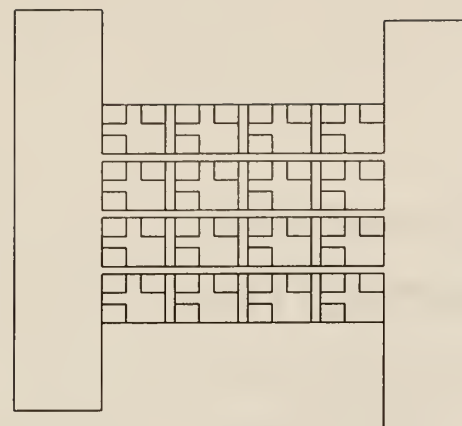


(a)

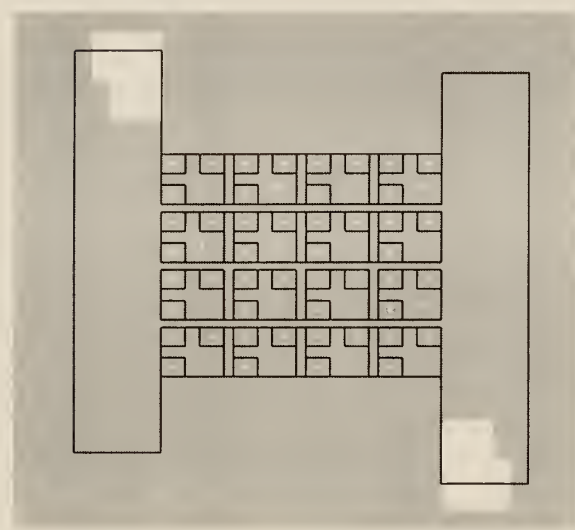


(b)

Figure 8.4. The top-views of mesa structure for three-color, three-stack QWIP  $4 \times 4$  FPA: (a) after etching for top-, middle-, and buffer-stack, and (b) after etching for top-, middle-, buffer, and bottom-stack.



(a)



(b)

Figure 8.5. The top-views of mesa structure for three-color, three-stack QWIP 4 x 4 FPA: (a) after etching for top-stack, middle-, buffer-, bottom-, and ohmic contact-stack, and (b) after passivation layer (gray area) evaporation on the etched mesa structure (the white areas are opened for the ohmic contact metalization).

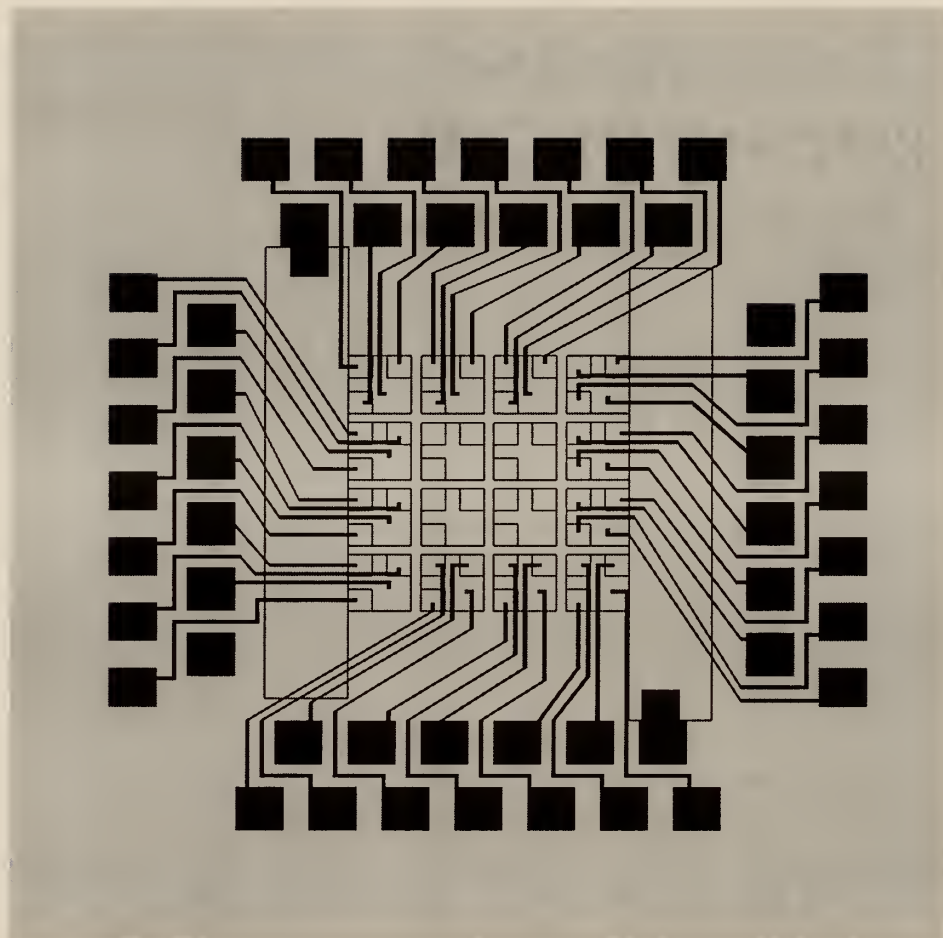


Figure 8.6. The final top-view of three-color, three-stack QWIP 4 x 4 FPA: after ohmic contact metalization evaporation (the dark areas are bonding pads and interconnect lines, and the gray area is passivation layer).

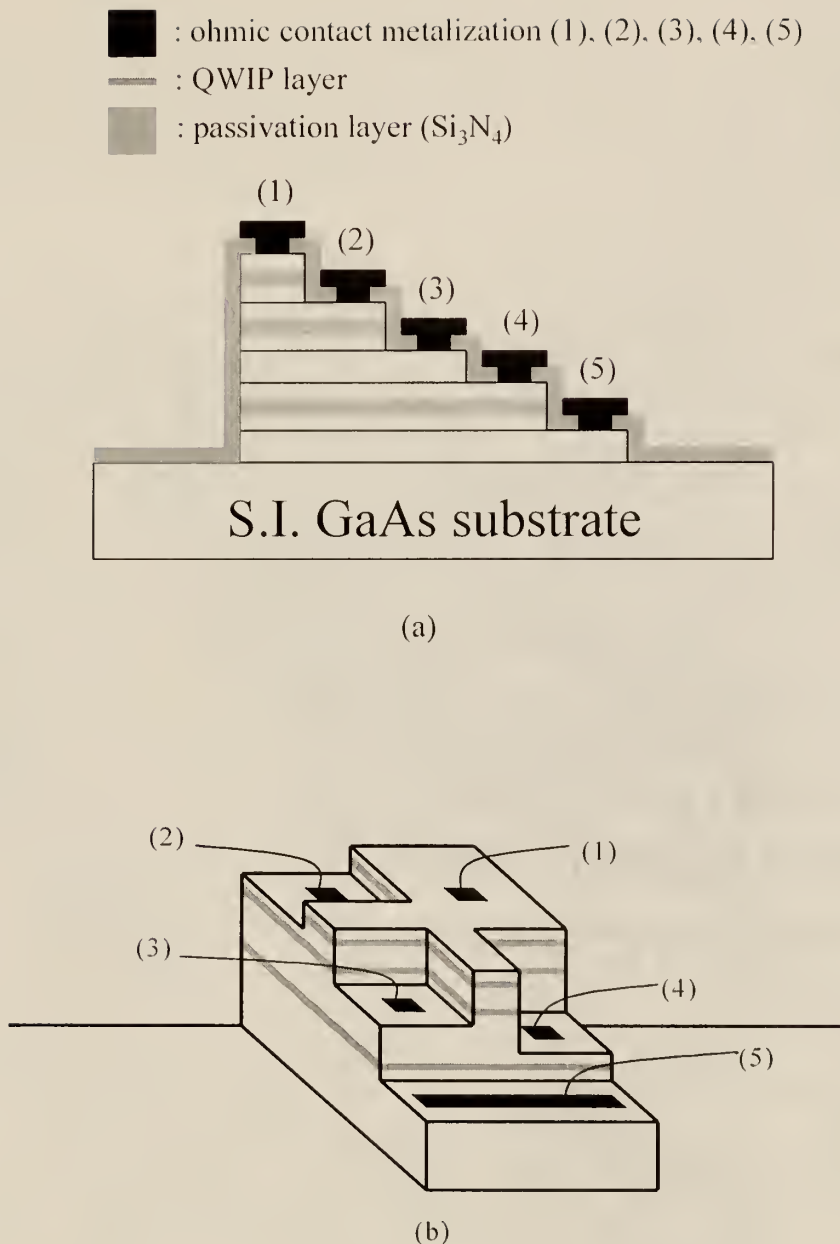


Figure 8.7. (a) The cross section view and (b) the three-dimensional (3-D) view of a detector pixel for the three-color, three-stack QWIP 4 x 4 FPA.

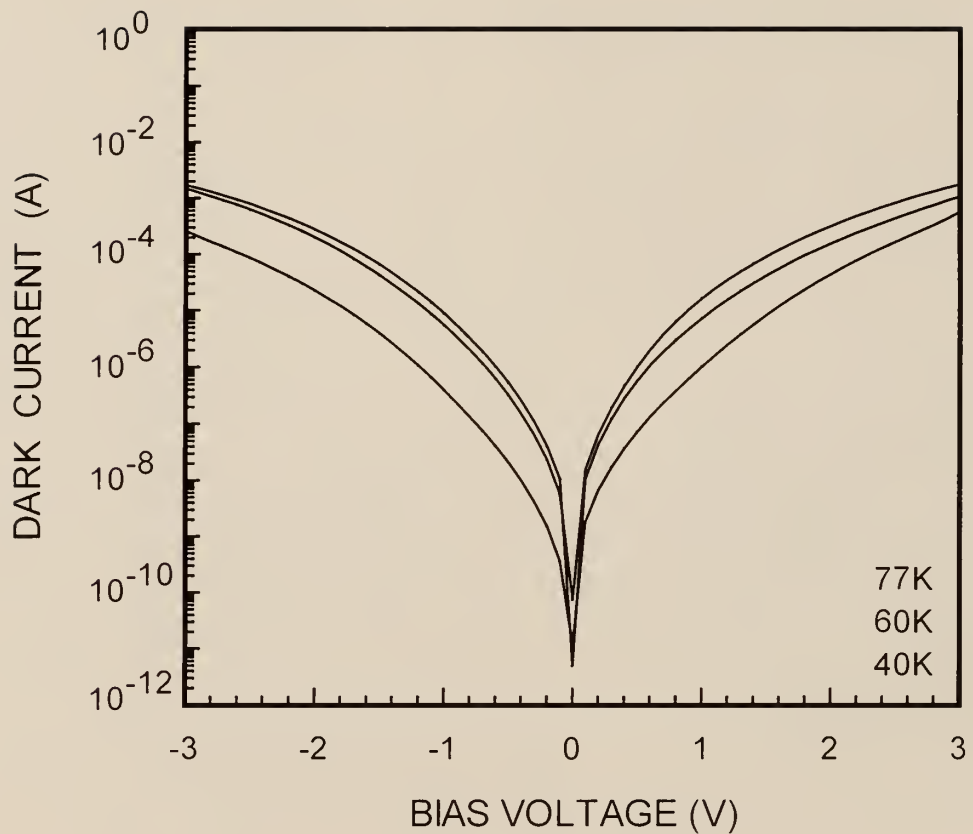


Figure 8.8. The dark current versus bias voltage (I-V) measured at  $T = 40, 60$ , and  $77\text{K}$  for the LWIR-QWIP (top-stack) of the LW/LW/MW QWIP  $4 \times 4$  FPA.

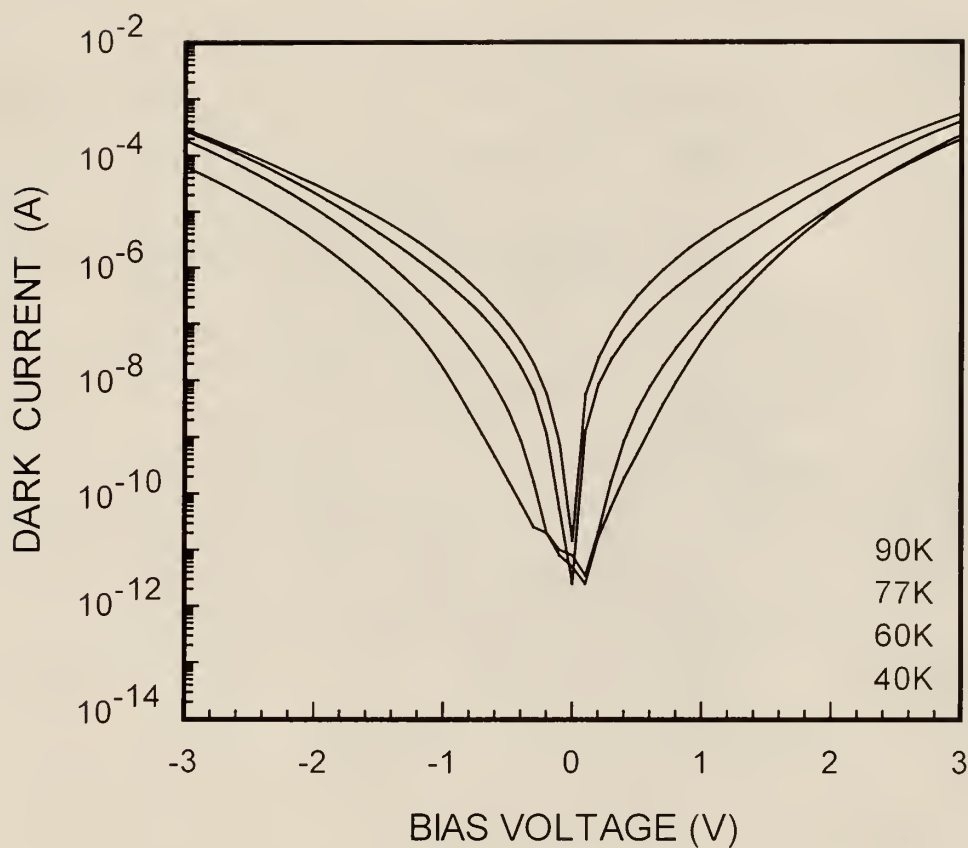


Figure 8.9. The dark current versus bias voltage (I-V) measured at  $T = 40, 60, 77$ , and  $90\text{K}$  for the LWIR-QWIP (middle-stack) of the LW/LW/MW QWIP  $4 \times 4$  FPA.

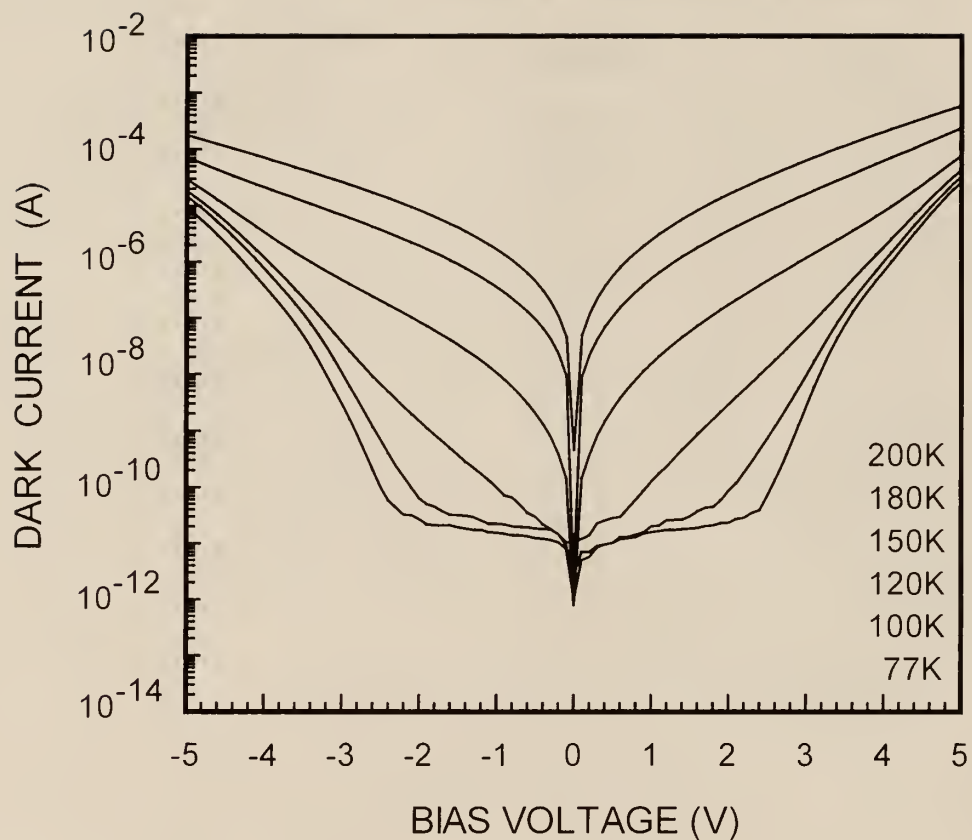


Figure 8.10. The dark current versus bias voltage (I-V) measured at T = 77, 100, 120, 150, 180, and 200K for the MWIR-QWIP (bottom-stack) of the LW/LW/MW QWIP 4 x 4 FPA.

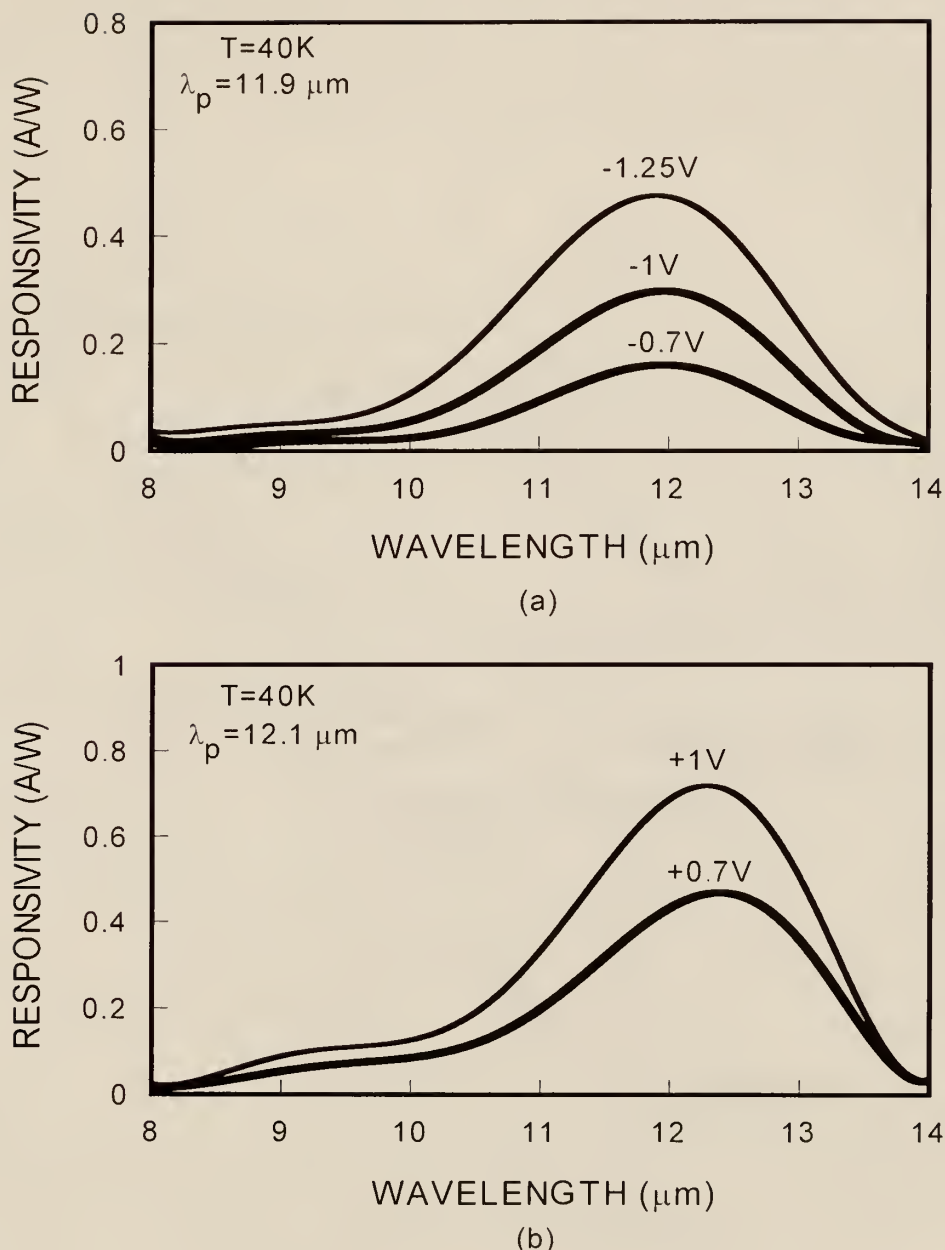


Figure 8.11. The spectral responsivity measured at  $T = 40\text{K}$  for the LWIR-QWIP (top-stack) of the LW/LW/MW QWIP 4 x 4 FPA: (a) negative and (b) positive biases.

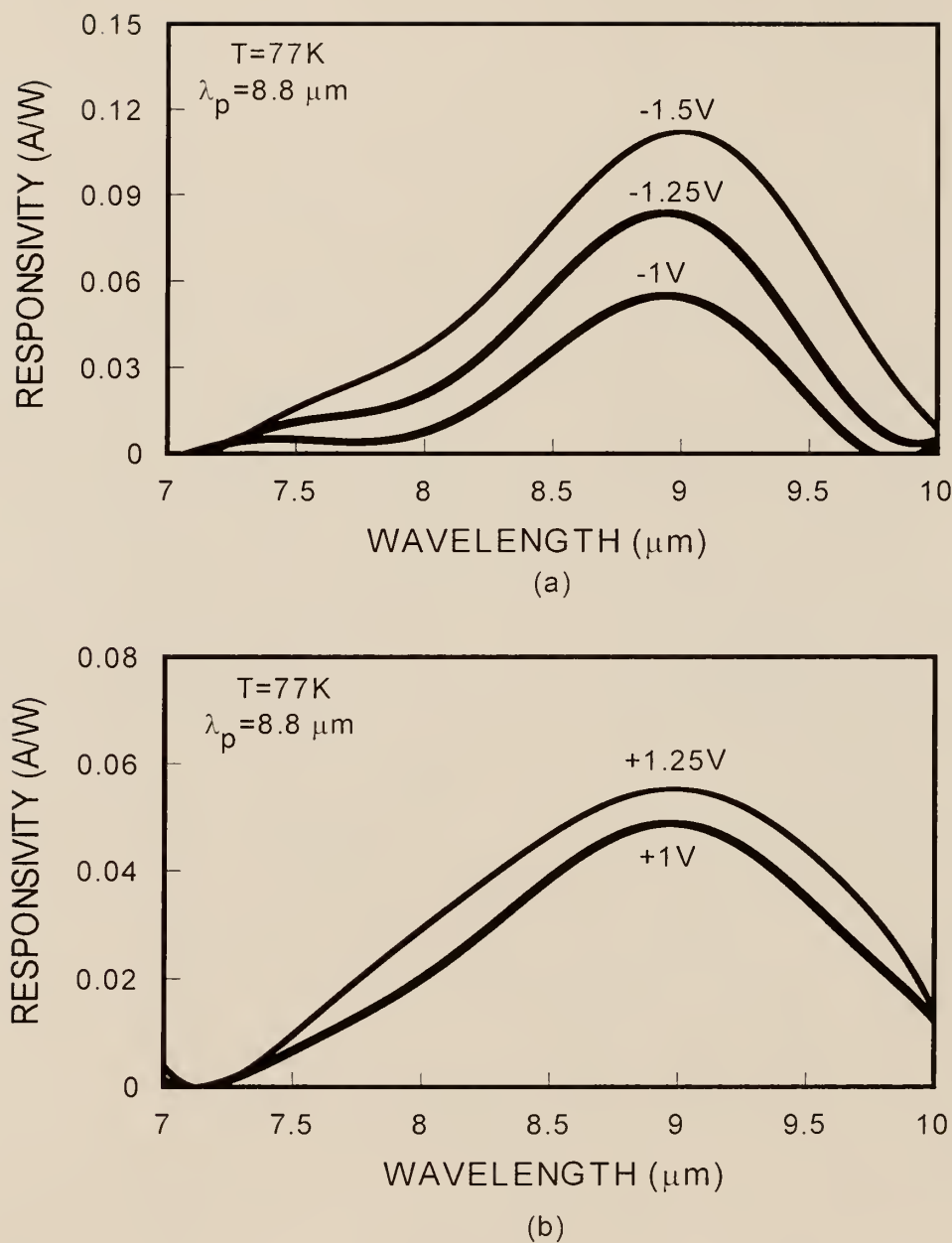


Figure 8.12. The spectral responsivity measured at  $T = 77\text{K}$  for the LWIR-QWIP (middle-stack) of the LW/LW/MW QWIP 4 x 4 FPA: (a) negative and (b) positive biases.

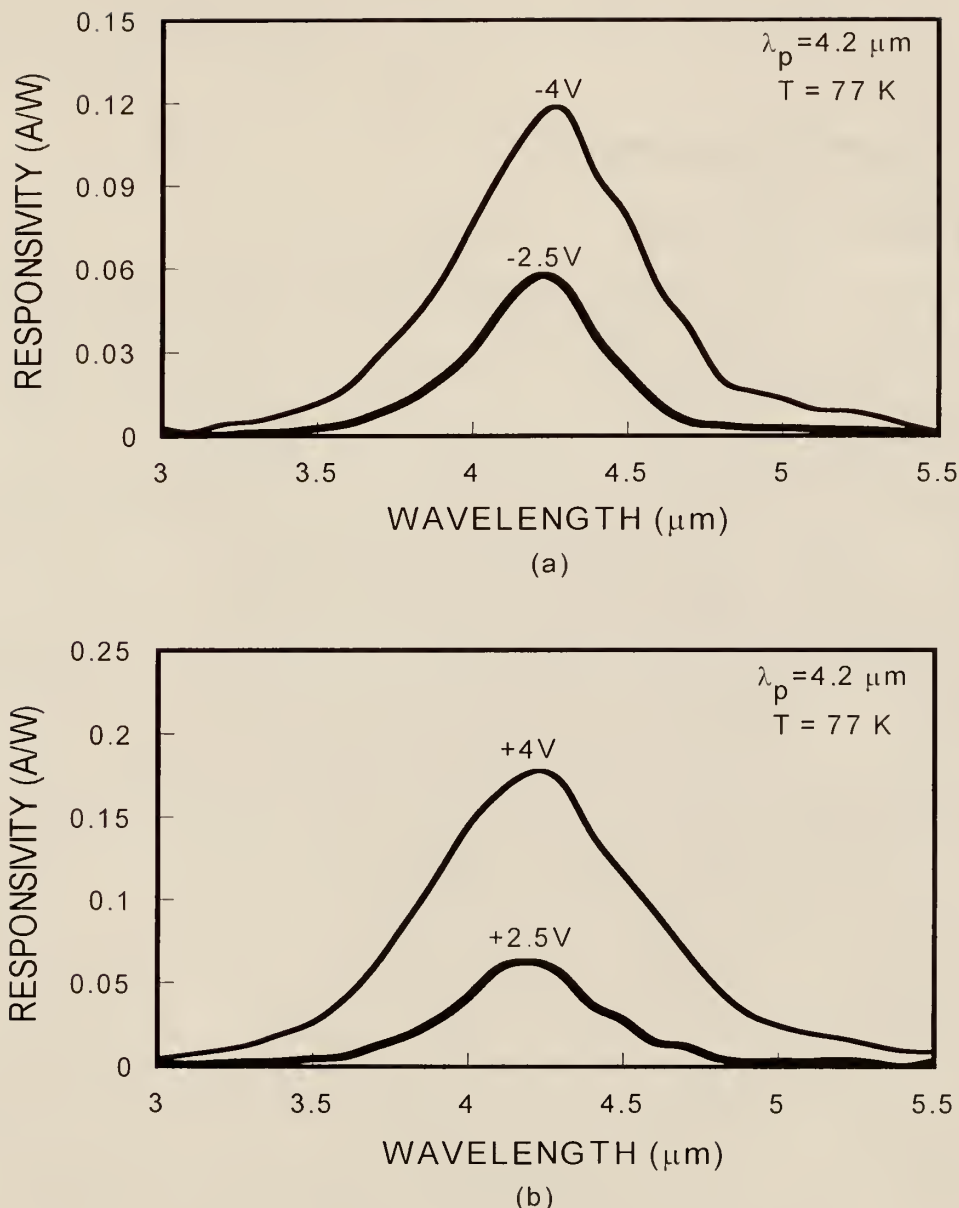


Figure 8.13. The spectral responsivity measured at  $T = 77\text{ K}$  for the MWIR-QWIP (bottom-stack) of the LW/LW/MW QWIP 4 x 4 FPA: (a) negative and (b) positive biases.

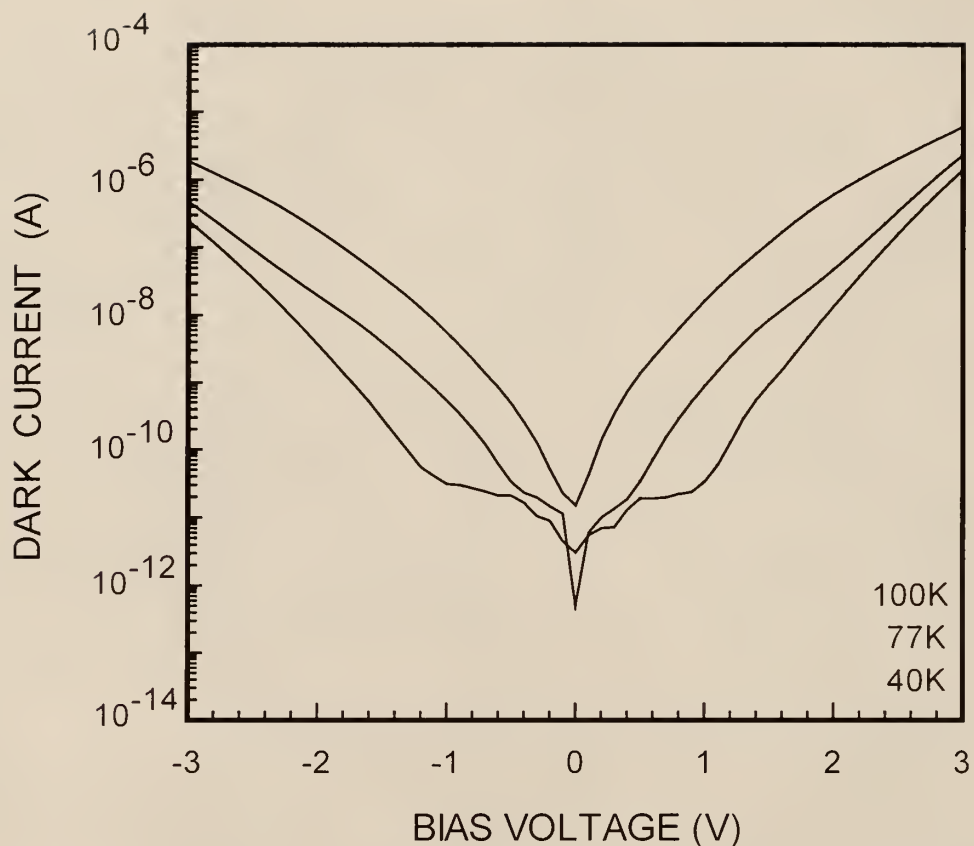


Figure 8.14. The dark current versus bias voltage (I-V) measured at  $T = 40$ ,  $77$ , and  $100\text{K}$  for the LWIR-QWIP (top-stack) of the LW/MW/SW QWIP  $4 \times 4$  FPA.

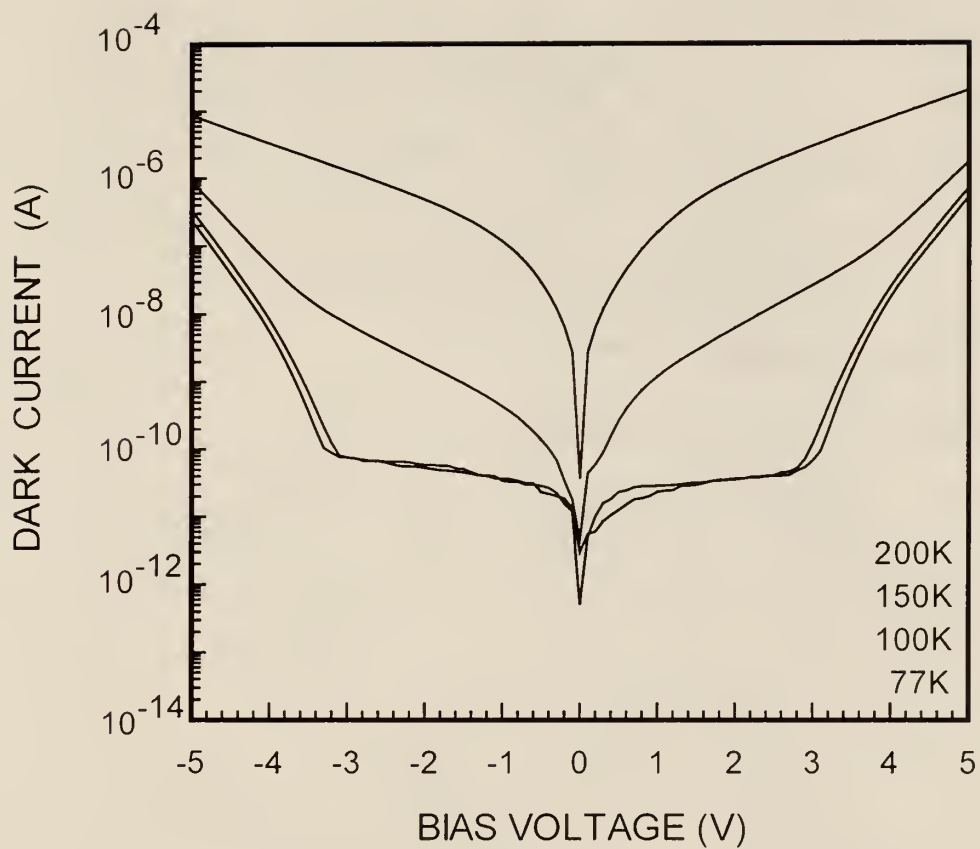


Figure 8.15. The dark current versus bias voltage (I-V) measured at  $T = 77, 100, 150$ , and  $200\text{K}$  for the MWIR-QWIP (middle-stack) of the LW/MW/SW QWIP  $4 \times 4$  FPA.

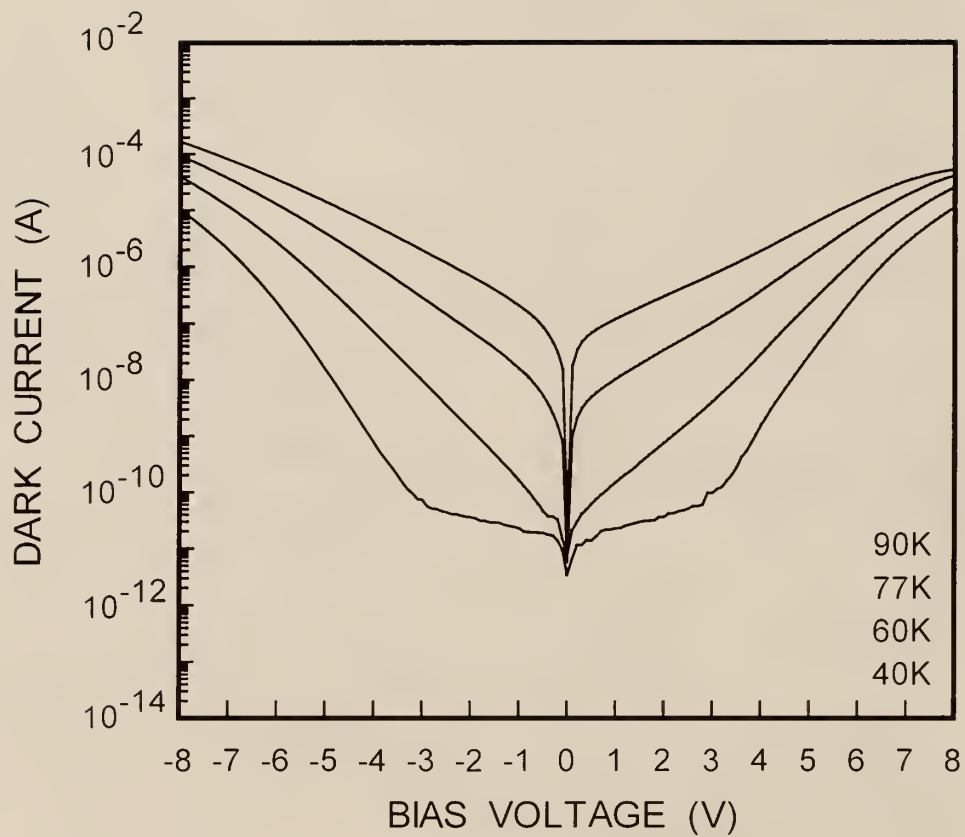


Figure 8.16. The dark current versus bias voltage (I-V) measured at T = 40, 60, 77, and 90K for the SWIR-QWIP (bottom-stack) of the LW/MW/SW QWIP 4 x 4 FPA.

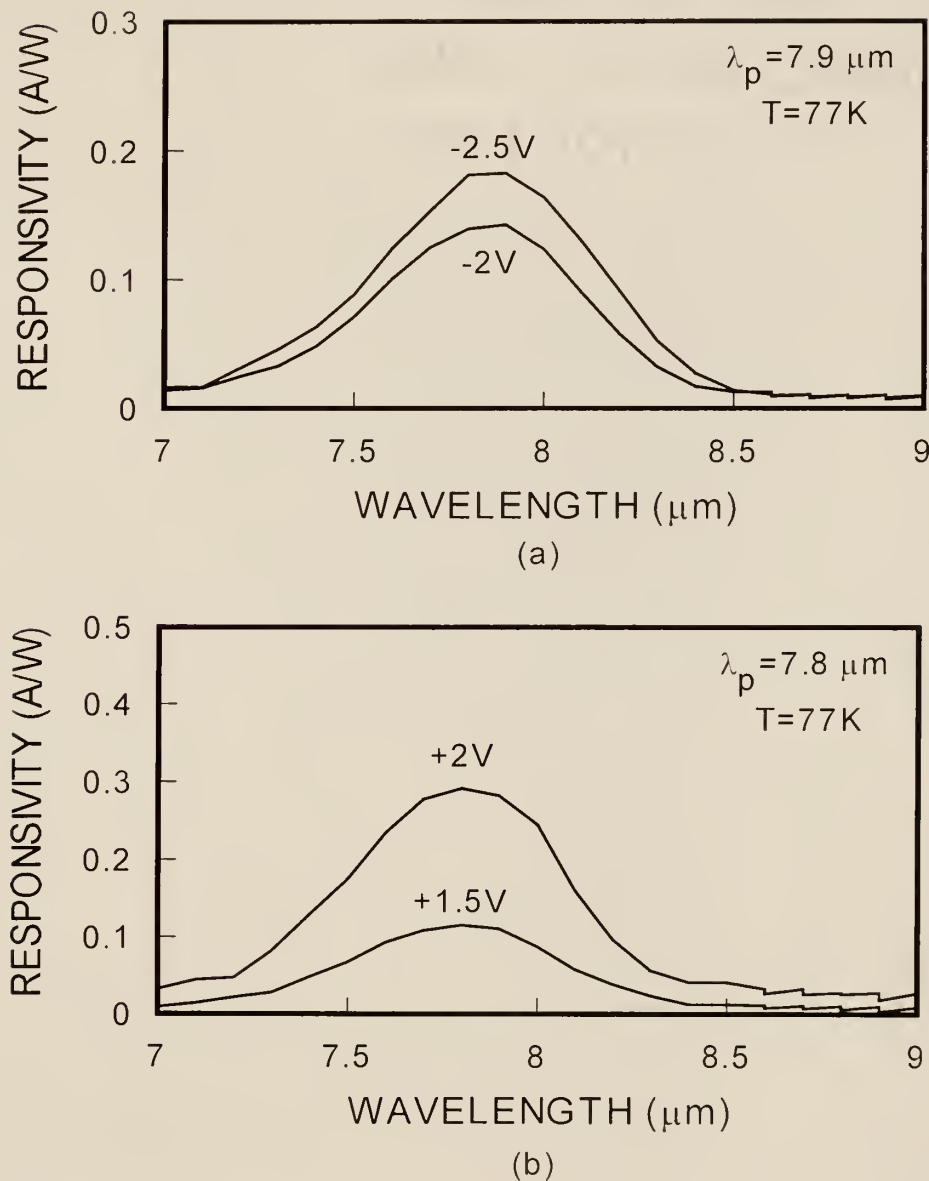


Figure 8.17. The spectral responsivity measured at  $T = 77\text{ K}$  for the LWIR-QWIP (top-stack) of the LW/MW/SW QWIP 4 x 4 FPA: (a) negative and (b) positive biases.

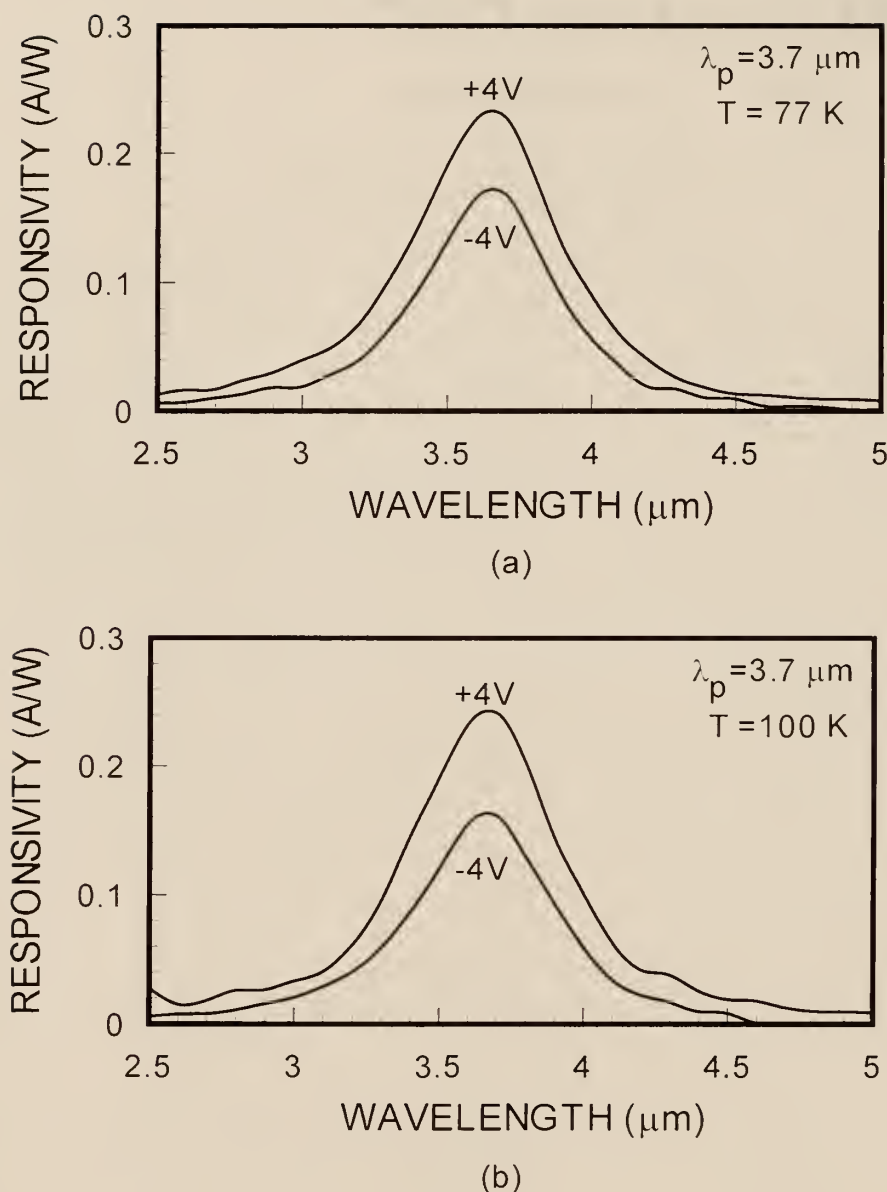


Figure 8.18. The spectral responsivity measured at  $T =$  (a) 77 and (b) 100K for the MWIR-QWIP (middle-stack) of the LW/MW/SW QWIP 4 x 4 FPA.

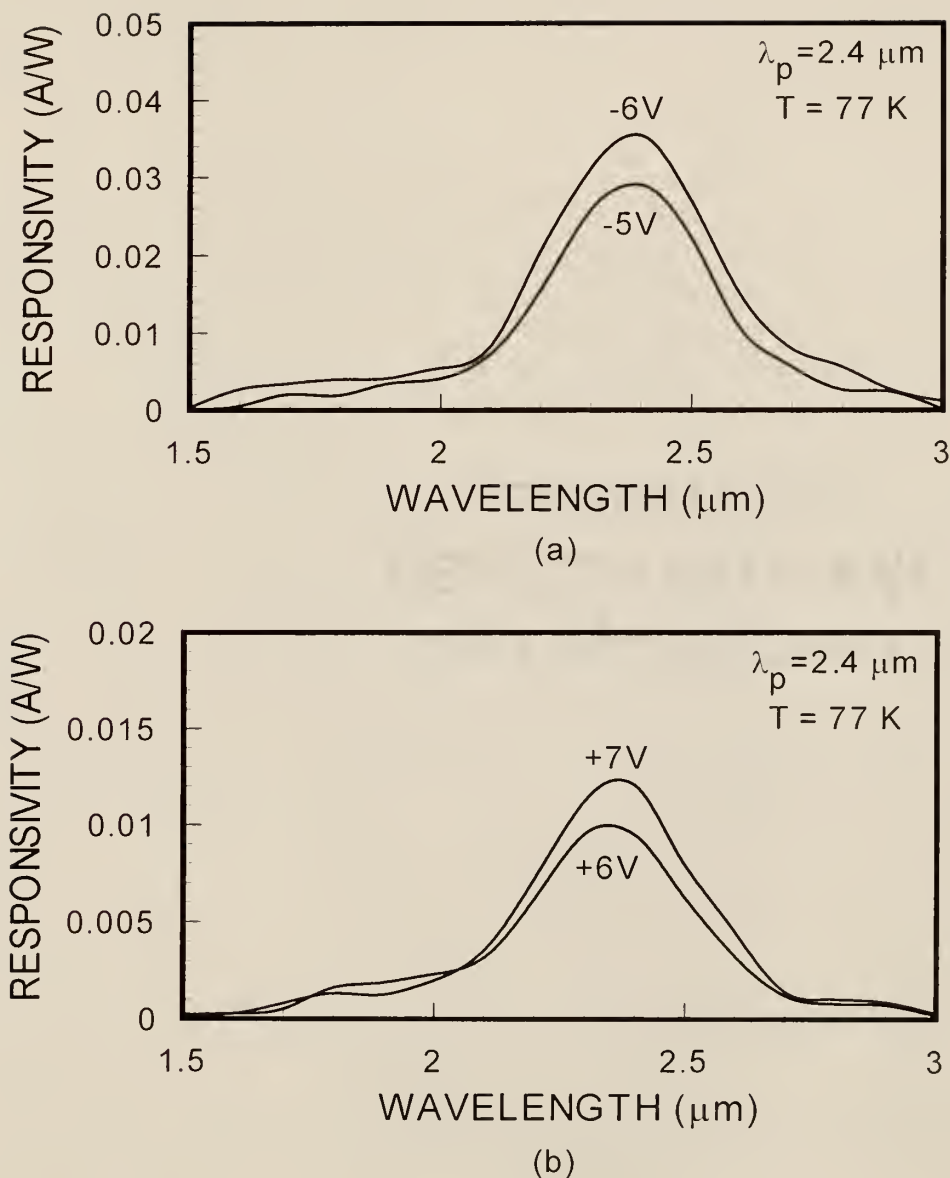


Figure 8.19. The spectral responsivity measured at  $T = 77\text{ K}$  for the SWIR-QWIP (bottom-stack) of the LW/MW/SW QWIP  $4 \times 4$  FPA: (a) negative and (b) positive biases.

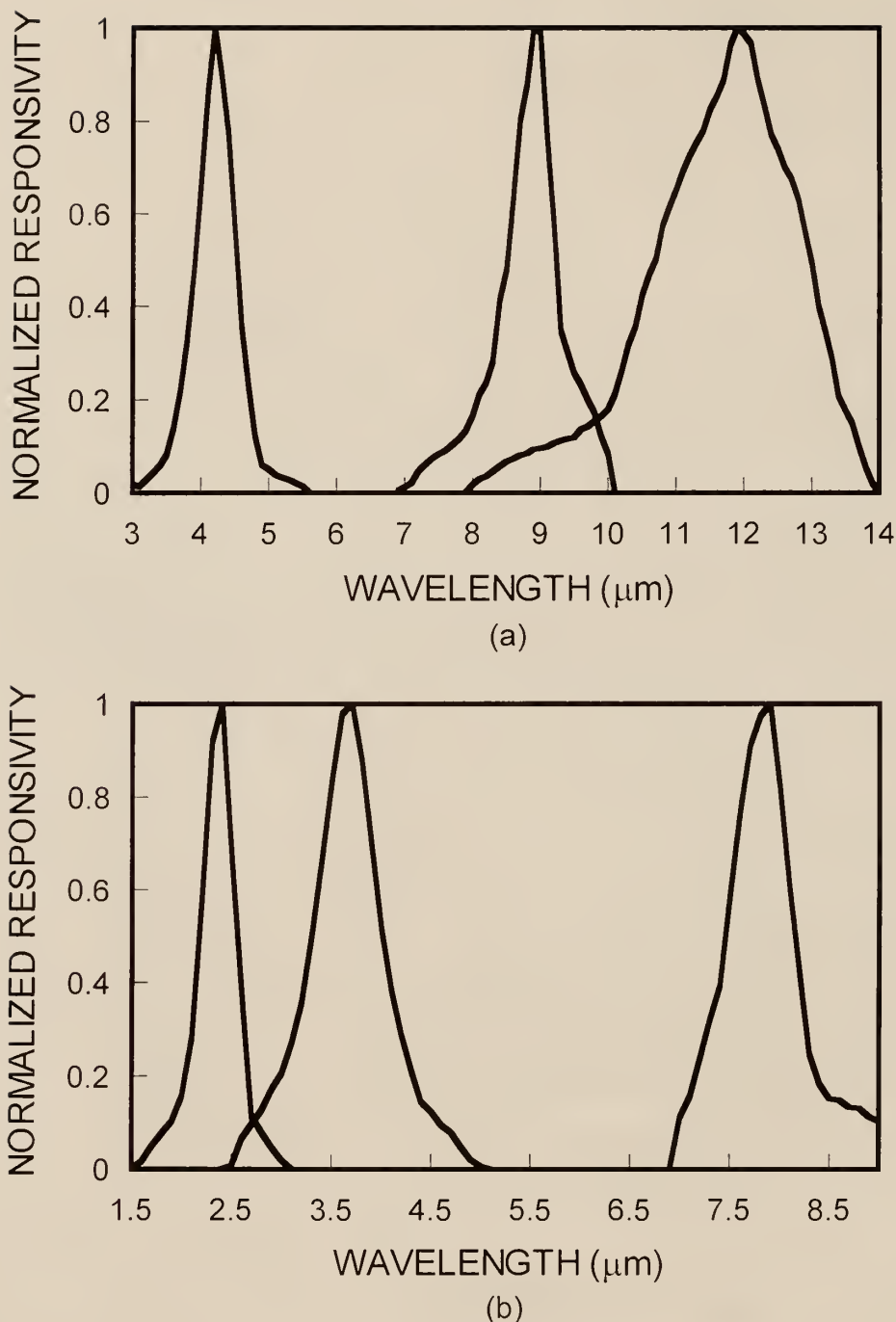


Figure 8.20. The normalized spectral responsivity for (a) LW/LW/MW and (b) LW/MW/SW QWIP 4 x 4 FPAs.

## CHAPTER 9 SUMMARY AND CONCLUSIONS

We have developed several novel high performance n-type quantum well infrared photodetectors (QWIPs) and two three-color, three-stack QWIP 4 x 4 focal plane arrays (FPAs) in this dissertation. These QWIP structures with excellent morphology were grown by molecular beam epitaxy (MBE) technique. The detection peak wavelengths extended from 1-3  $\mu\text{m}$  short-wavelength infrared (SWIR) to 8-14  $\mu\text{m}$  long-wavelength infrared (LWIR) regions including 3-5  $\mu\text{m}$  mid-wavelength infrared (MWIR) region. Multicolor and broadband detection with high performance have been achieved through single QWIP devices by using the asymmetric structure and the strain effect. In addition, the QWIP 4 x 4 FPAs have been successfully demonstrated for three-color wavelength detection in two-band or three-band in infrared region.

The first QWIP device was a high performance InGaAs/AlGaAs/InGaAs broadband triple-coupled (BB TC-) QWIP for voltage tunable multicolor and broadband detection in 7-12  $\mu\text{m}$  long-wavelength infrared (LWIR) regime. This BB TC-QWIP device consists of three-stack structure without contact layers between the stacks. Each stack has unique quantum well width, period, and barrier height by using different Al mole fraction. Therefore, each stack can detect different peak wavelength and hence the broadband detection can be obtained by the superposition of the detection wavelengths in this whole three-stack structure. The peak responsivity and full-width half-maximum (FWHM) at

the bias voltage of -4.5V was 0.81 A/W at  $\lambda_p = 10.8 \mu\text{m}$  and broad responsivity curve of  $\Delta\lambda/\lambda_p = 20 \%$  was achieved for this QWIP device. This  $\Delta\lambda/\lambda_{p2} = 20 \%$  is much broader than that of the one stack high-strain TC-QWIP ( $\Delta\lambda/\lambda_p = 10 \%$ ). In particular, the peak spectral responsivity at  $\lambda_p = 10.6 \mu\text{m}$  and  $V_b = -5.2\text{V}$  was found to be very high as much as 2.75 A/W. The corresponding background limited performance (BLIP) detectivity ( $D^*_{\text{BLIP}}$ ) was  $1.98 \times 10^{10} \text{ cm}\cdot\text{Hz}^{1/2}/\text{W}$ . The voltage tunable multicolor detection ranging from 10.6 to  $10.8 \mu\text{m}$  was observed between -5.2V and -4.75V in this BB TC-QWIP.

The next QWIP was a mid-wavelength infrared (MWIR) TC-QWIP using  $\text{In}_{0.53}\text{Ga}_{0.47}\text{As}/\text{In}_{0.52}\text{Al}_{0.48}\text{As}/\text{In}_{0.3}\text{Ga}_{0.7}\text{As}$  material system grown on InP substrate. The bound-to-continuum (BTC) transition was observed at positive and lower negative bias voltages while the bound-to-bound (BTB) transition can be detected and dominant at higher negative bias voltages. The peak spectral responsivity for this MWIR TC-QWIP was 0.31 A/W at  $\lambda_p = 4.6 \mu\text{m}$ ,  $V_b = -5.5\text{V}$ , and  $T = 77\text{K}$ . The peak detectivity ( $D^*$ ) under non-BLIP condition was  $1.44 \times 10^{10} \text{ cm}\cdot\text{Hz}^{1/2}/\text{W}$  at  $T = 116\text{K}$ ,  $\lambda_p = 4.6 \mu\text{m}$ , and  $V_b = -4\text{V}$ . This device can be operated up to 116K.

The third QWIP design was dual-mode (i.e., PV and PC mode) operation AlAs/InGaAs/AlAs/InAlAs double-barrier (DB-) QWIP with peak detection wavelength at  $3.4 \mu\text{m}$  for mid-wavelength infrared (MWIR) detection grown on InP substrate. The device was under background limited performance (BLIP) at  $T = 77\text{K}$ ,  $V_b < -2.5\text{V}$ . The PV mode response was observed for temperatures up to 170K under BLIP condition. The PC mode peak responsivity at  $V_b = -3\text{V}$  was found to be 0.159 A/W at  $T = 77\text{K}$  while the PV mode responsivity was found to be 19 mA/W and 9 mA/W at  $T = 77\text{K}$  and 205K, respectively. The peak detectivity for the PV mode under BLIP was  $D^*_{\text{BLIP}} = 8.9 \times 10^{10}$

cm-Hz<sup>1/2</sup>/W at  $\lambda_p = 3.4 \mu\text{m}$  and T = 77K. And the PV mode detectivity under BLIP at T = 163K was  $D^*_{\text{BLIP}} = 3.42 \times 10^{10} \text{ cm-Hz}^{1/2}/\text{W}$  at  $\lambda_p = 3.4 \mu\text{m}$ . This DB-QWIP can be operated at a temperature as high as 205K with good characteristics.

The fourth QWIPs were two novel high performance InGaAs/AlGaAs/GaAs QWIPs using digital graded superlattice barrier (DGSLB) for LWIR and broadband detection. The short-period superlattice structures with variable well/barrier thickness were used for the DGSLB structure to change the Al mole fraction ratio and hence the energy band gap of the graded barrier. Two DGSLB QWIPs have been demonstrated, which were broadband (BB-) and double-barrier (DB-) DGSLB QWIPs. For the BB-DGSLB QWIP, the peak responsivity at  $\lambda_p = 9.8 \mu\text{m}$  was 1.07 A/W at  $V_b = +0.75\text{V}$  and T = 35K. The broadband spectral response from 7  $\mu\text{m}$  to 16  $\mu\text{m}$  was observed under positive bias condition in this device. The full-width half-maximum (FWHM) spectral bandwidth at  $V_b = +0.75\text{V}$  and  $+0.5\text{V}$  were found to be  $\Delta\lambda/\lambda_p = 62\%$  and 54%, respectively. A large spectral responsivity as much as 3.0 A/W was obtained at  $V_b = +1\text{V}$  and  $\lambda_p = 12 \mu\text{m}$  with normal bandwith for the DB-DGSLB QWIP. The BLIP detectivity ( $D^*_{\text{BLIP}}$ ) at 0.75V for the BB-DGSLB QWIP were found to  $1.3 \times 10^{10} \text{ cm Hz}^{1/2}/\text{W}$  at  $\lambda_p = 9.8 \mu\text{m}$ . The BLIP detectivity ( $D^*_{\text{BLIP}}$ ) at  $V_b = -1.5\text{V}$  for the DB-DGSLB QWIP were found to be  $5.8 \times 10^9 \text{ cm Hz}^{1/2}/\text{W}$  at  $\lambda_p = 11.8 \mu\text{m}$ . This DGSLB structure can enable the broadband detection and significantly improve the device performance under positive bias operation.

The fifth QWIPs developed were two linear- graded barrier (LGB) QWIPs which are broadband (BB-) and double-barrier (DB-) LGB QWIPs. The superposition of the photo-responses due to the transitions from the ground state to the upper excited states induced the broadband detection (6.5-16  $\mu\text{m}$ ) under positive bias condition in the BB-LGB

QWIP. The peak wavelength for this device was blue-shifted from 10.2 to 9.9  $\mu\text{m}$  and 8.5 to 7.5  $\mu\text{m}$  under negative biases ( $-1\text{V} < V_b < -3\text{V}$ ), respectively. The maximum responsivity at +2.75V was found to be 1.75 A/W at  $\lambda_p = 11.9 \mu\text{m}$  and  $T = 35\text{K}$ . The corresponding full-width half-maximum (FWHM) spectral bandwidth and the BLIP detectivity were  $\Delta\lambda/\lambda_p = 52\%$  and  $1.3 \times 10^{10} \text{ cm Hz}^{1/2}/\text{W}$ , respectively. For the DB-LGB QWIP, the responsivity was greatly enhanced due to the use of an enlarged high-strain quantum well and DB structure. The maximum responsivity was obtained 4.38 A/W at  $\lambda_p = 9.1 \mu\text{m}$ ,  $V_b = +3.5\text{V}$ , and  $T = 35\text{K}$ . The corresponding BLIP detectivity and FWHM bandwidth were  $2.5 \times 10^{10} \text{ cm-Hz}^{1/2}/\text{W}$  and  $\Delta\lambda/\lambda_p = 27\%$ , respectively. The FWHM spectral bandwidths under positive biases were two times broader than under negative biases. This LGB structure contributed to the broadband detection due to the overlapping of the transitions and the combination of these LGB and DB structures induced both broadband and high-sensitivity detection.

Finally, we have developed two three-color, three-stack QWIP 4 x 4 FPAs grown on GaAs substrate. Each pixel has a size of 100 x 100  $\mu\text{m}^2$  and the 12 out of 16 detector pixels in one FPA were connected to the wire-bonding pads for characterization. The 4 x 4 array detectors was polished to 45° facet on the back side of substrate for coupling the incident IR radiation into the active layers of the FPA detectors. The first LW/LW/MW FPA has three peaks (12, 8.8, and 4.2  $\mu\text{m}$ ) in two bands (LWIR and MWIR regions). The peak responsivity were found to be 0.77 A/W at  $V_b = +1\text{V}$  and  $\lambda_p = 12.1 \mu\text{m}$  for the top-stack LWIR QWIP. The peak responsivity at  $T = 77\text{K}$  for the middle-stack LWIR-QWIP was 0.13 A/W at  $V_b = -1.5\text{V}$  and  $\lambda_p = 8.8 \mu\text{m}$  while for the bottom-stack MWIR QWIP the peak responsivity was 0.12 A/W with a peak wavelength of 4.2  $\mu\text{m}$  at  $V_b = -4\text{V}$  and  $T$

= 77K. This bottom-stack can be operative up to T = 180K. The truly three-color detection (7.9, 3.7, and 2.4  $\mu\text{m}$ ) in three bands (LWIR, MWIR, and SWIR regions) was observed in the second LW/MW/SW QWIP 4 x 4 FPA. The peak responsivity for the top-stack LWIR-QWIP at T = 77K was 0.29 A/W ( $\lambda_p = 7.8 \mu\text{m}$ ) at  $V_b = +2\text{V}$ . The peak wavelength for the middle-stack MWIR-QWIP was  $\lambda_p = 3.7 \mu\text{m}$  independent of the applied bias voltage and the operating temperature. The peak responsivity at  $V_b = +4\text{V}$  and  $\lambda_p = 3.7 \mu\text{m}$  was found to be 0.23 A/W at T = 77K. The spectral responsivity for the middle-stack MWIR-QWIP was measured up to T = 200K. The bottom-stack of this LW/MW/SW QWIP 4 x 4 FPA was the SWIR-QWIP using the indirect-barrier (IB) and the peak responsivity at -4.5V was found to be 0.021 A/W with a peak wavelength of 2.4  $\mu\text{m}$  at T = 77K. These two QWIP 4 x 4 FPAs have been successfully demonstrated for multicolor detection using multi-stack structure. Furthermore, this excellent performance for multicolor detection can be expected in the larger format QWIP FPAs with high uniformity due to the advanced MBE growth technique.

Table 9.1 summarized the device performance for QWIP developed in this work. For broadband and voltage tunable multicolor detection in one band, the asymmetric structure using strain effect due to lattice mismatch was strongly suggested and demonstrated. In addition, it is well known from the results of this study that the multi-stack QWIP structure can also provide the multicolor detection in two- or three-band and the broadband detection. For the further optimization of the QWIP device performance, the specific study is needed in modeling of device, improving low background characteristics, theoretical consideration on bias distribution across the active QWIP layer, temperature effect and so on. Recently, many efforts have been done in quantum

dot infrared photodetector (QDIP), photonic crystal structure, and type II uncooled detector, which can greatly improve the device performance. The light coupling scheme is also of extreme important for large two-dimensional (2-D) FPA applications. The metal or dielectric grating coupler with lamellar (one-dimensional), crossed (two-dimensional), random scattering structures is required for the absorption of the normal incidence IR radiation for n-type QWIP device. Usually, one period of the grating coupler is a few micrometer ( $\mu\text{m}$ ) so that the dry etching procedure for dielectric grating is needed for anisotropic pattern transfer onto the wafer. The inductively coupled plasma (ICP) etching technique has been widely employed for dry etching of compound semiconductor, which has more advantage than reactive ion etching (RIE): 1) high ion density, 2) independent control of ion energy and flux. 3) lower damage on surface, and 4) anisotropic pattern transfer. The thinned substrate combined with grating and the microlense are also good candidates for the multiple reflection light coupling. Finally, the basic understanding of the design and analysis of the infrared FPA readout electronics is main concern in FPA camera, which includes accurate CMOS and detector modeling, control logic design, circuit design and layout, image signal processing, and portable cryogenic cooling system.

Table 9.1. The summary of the QWIP performance for devices developed in this work.

Device	T (°K)	Bias (V)	$\lambda_p$ (μm)	$R_{ip}$ (A/W) [ $\Delta\lambda/\lambda_p$ (%)]	$D^*$ (cm-Hz <sup>1/2</sup> /W)	
BB TC-QWIP	40	-5.2	10.6	2.75 [20]	$1.98 \times 10^{10}$ (BLIP)	
MWIR TC-QWIP	77	-5.5	4.6	0.31	$4.33 \times 10^{10}$ (non-BLIP)	
DB-QWIP	77	-3.5	3.4	0.19	$5.47 \times 10^9$ (non-BLIP)	
BB-DGSLB	35	-0.75	11	0.39 [13]	$6.71 \times 10^{10}$ (non-BLIP)	
		+0.75	9.8	1.07 [62]	$1.89 \times 10^{10}$ (non-BLIP)	
DB-DGSLB	35	-1.5	11.8	0.28	$4.79 \times 10^9$ (non-BLIP)	
		+1	12	3	$2.54 \times 10^{10}$ (non-BLIP)	
BB-LGB QWIP	35	-3	9.9	1.61 [11]	$1.54 \times 10^{10}$ (BLIP)	
		+2.75	11.9	1.75 [52]	$1.29 \times 10^{10}$ (BLIP)	
DB-LGB QWIP	35	-4.5	9.2	1.23 [12]	$1.46 \times 10^{10}$ (BLIP)	
		+3.5	9.1	4.38 [27]	$2.45 \times 10^{10}$ (BLIP)	
QWIP	LW	40	-0.7	11.9	0.19	$1.94 \times 10^{10}$ (non-BLIP)
4 x 4	LW	77	-1	8.8	0.073	$3.93 \times 10^9$ (non-BLIP)
	FPA (1)	MW	77	+2.5	4.2	0.063
QWIP	LW	77	-2	7.9	0.14	$2.25 \times 10^{10}$ (non-BLIP)
4 x 4	MW	77	+4	3.7	0.23	$2.12 \times 10^{10}$ (non-BLIP)
FPA (2)	SW	77	-5	2.4	0.029	$5.89 \times 10^8$ (non-BLIP)

## REFERENCES

1. Paul R. Norton, Proc. of SPIE **3379**, 102 (1998).
2. L. Esaki and T. Tsu, IBM J. Res. Develop. **14**, 61 (1970).
3. L. C. West and S. J. Eglash, Appl. Phys. Lett. **46**, 1156 (1985).
4. B. F. Levine, K. K. Choi, C. G. Bethea, J. Walker, and R. J. Malik, Appl. Phys. Lett. **50**, 1092 (1987).
5. D. D. Coon and R. P. Karunasiri, Appl. Phys. Lett. **33**, 495 (1984).
6. L. S. Yu and S. S. Li, Appl. Phys. Lett. **59**, 1332 (1991).
7. B. F. Levine, C. G. Bethea, G. Hasnain, V. O. Shen, E. Pelve, R. R. Abbot, and S. J. Hsieh, Appl. Phys. Lett. **56**, 851 (1990).
8. Jerome Chu and Sheng S. Li, IEEE J. Quantum Electronics **33**, 1104 (1997).
9. H. C. Liu, F. Szmulowicz, Z. R. Wasilewski, M. Buchanan, and G. J. Brown, J. Appl. Phys. **85**, 2972 (1999).
10. M. A. Kinch and A. Yariv, Appl. Phys. Lett. **55**, 2093 (1989).
11. M. A. Kinch, S. R. Borrello, and A. Simmons, Infrared Phys. **17**, 127 (1977).
12. B. F. Levine, J. of Appl. Phys. **74**, R1 (1993).
13. Walter R. Dyer and Dwight Duston, Electrochemical Society Proceedings **PV97-33**, 1 (1997).
14. C. G. Bethea, B. F. Levine, M. T. Asom, R. E. Leibenguth, J. W. Stayt, K. Glogovsky, R. A. Morgan, J. D. Blackwell and W. J. Parrish, IEEE Trans. Electron, Devices **40**, 1957 (1993).
15. W. A. Beck, J. W. Little, A. C. Goldberg and T. S. Faska, in H. C. Liu, B. F. Levine and J. Y. Andersson (eds.), "Quantum Well Intersubband Transition Physics and Devices," NATO ASI Series, **vol. 270**, 55, Kluwer, Dordrecht (1994).

16. S. D. Gunapala, J. K. Liu, M. Sundaram, J. S. Park, C. A. Shott, T. Hoelter, T. I. Lin, S. T. Massie, P. D. Maker, R. E. Muller and G. Sarusi, 3<sup>rd</sup> Int. Symp. Long Wavelength Infrared Detectors and Arrays. Physics and Applications III. Electrochemical Society Proc., **vol. 95**, 55, The Electrochemical Society, Inc., Pennington, NJ (1995).
17. S. D. Gunapala, S. V. Bandara, J. K. Liu, W. Hong, M. Sundaram, P. D. Maker and R. E. Muller, Electrochemical Society Proceedings **PV97-33**, 14 (1997).
18. David J. Griffiths, "Introduction to Quantum Mechanics," Prentice-Hall, Inc., Englewood Cliff, NJ (1995).
19. G. Bastard, Phys. Rev. **B-24**, 5693 (1981).
20. D. Delagebeaudeuf, P. Deleckyse, P. Etienne, J. Massiers, M. Laviron, J. Chaplart, and T. Linh, Electron. Lett. **18**, 85 (1982).
21. I. Hase, H. Kawai, K. Kaneko, and K. Watanabe, Electron. Lett. **20**, 491 (1984).
22. P. J. Price, IBM J. Res. Develop. **17**, 39 (1973).
23. M. Artaki and K. Hess, Superlattice and Microstructures **1**, 489 (1985).
24. Ajoy K. Ghatak, K. Thyagarajan, and M. R. Shenoy, IEEE J. Quantum Electronics **24**, 1524 (1988).
25. F. H. Pollack, "Semiconductors and Semimetals," ed. T. P. Pearsall, **vol. 32**, 17, Academic Press, New York (1990).
26. J. W. Matthews and A. E. Blakeslee, J. Cryst. Growth **32**, 265 (1976).
27. S. H. Pan, H. Shen, Z. Hang, F. H. Pollak, W. Zhuang, Q. Xu, A. P. Roth, R. A. Masut, C. Lacelle, and D. Morris, Phys. Rev. **B-38**, 3375 (1988).
28. J. W. Choe, O. Byungsung, K. M. S. V. Bandara, and D. D. Coon, Appl. Phys. Lett. **56**, 1679 (1990).
29. K. M. S. V. Bandara and D. D. Coon, Appl. Phys. Lett. **53**, 1865 (1988).
30. S. J. Allen, Jr. and D. C. Tsui, Solid-State Commun. **20**, 425 (1976).
31. M. O. Manasreh, F. Szmulowicz, T. Vaughan, K. R. Evans, C. E. Stutz, and D. W. Fischer, Phys. Rev. **B43**, 9996 (1991).
32. A. Raymond, J. L. Robert, and C. Bernard, J. Phys. **C12**, 2289 (1979).
33. M. J. Kane, M. T. Emeny, N. Apsley, C. R. Whitehouse, and D. Lee, Superlattices and Microstructures **5**, 587 (1989).

34. D. Ahn and S. L. Chuang. Physical Review B **35**, 35 4149 (1987).
35. Rui Q. Yang, Appl. Phys. Lett. **66**, 959 (1995).
36. Yoav Peleg, Reuven Pnini, and Elyahu Zoarur, "Theory and Problems of Quantum Mechanics," McGraw-Hill, New York (1998).
37. S. K. Chun, D. S. Pan, and K. L. Wang, Phys. Rev. B **47**, 15638 (1993).
38. E. Pelve, F. Beltram, C. G. Bethea, B. F. Levine, V. O. Shen, and S. J. Hsieh, J. Appl. Phys. **66**, 5656 (1989).
39. B. F. Levine, C. G. Bethea, G. Hasnain, V. O. Shen, E. Pelve, and R. R. Abbott, Appl. Phys. Lett. **56**, 851 (1990).
40. A G Petrov and A Ya Shik, Semicond. Sci. Technol. **6**, 1163 (1991).
41. S. R. Andrews and B. A. Miller, J. Appl. Phys. **70**, 993 (1991).
42. H. C. Liu, A. G. Steele, M. Buchanan, and Z. R. Wasilewski, J. Appl. Phys. **73**, 2029 (1993).
43. F. Luc, E. Rosencher, and B. Vinter, Appl. Phys. Lett. **62**, 1143 (1993).
44. Jian-Ping Peng, Yao-Ming Mu, and Xue-Chu Shen, J. Appl. Phys. **74**, 1421 (1993).
45. L. Thibaudeau, P. Bois, and J. Y. Duboz, J. Appl. Phys. **79**, 446 (1996).
46. Daniel C. Wang, Gijs Bosman, and Sheng S. Li, Appl. Phys. Lett. **68**, 2532 (1996).
47. V. Ryzhii, J. Appl. Phys. **81**, 6442 (1997).
48. S. D. Gunapala, B. F. Levine, L. Pfeiffer, and K. West, J. Appl. Phys. **69**, 6517 (1991).
49. E. L. Derniak and D. G. Crowe, "Optical Radiation Detectors," Wiley, New York (1984).
50. B. F. Levine, S. D. Gunapala, J. M. Kuo, S. S. Pei, and S. Hui, Appl. Phys. Lett. **59**, 1864 (1991).
51. B. F. Levine, C. G. Bethea, G. Hasnain, J. Walker, and R. J. Malik, Appl. Phys. Lett. **53**, 296 (1988).
52. Yimin Huang and Chenhsin Lien, J. Appl. Phys. **78**, 2700 (1995).
53. Yimin Huang, Chenhsin Lien, and Tan-Fu Lei, J. Appl. Phys. **74**, 2598 (1993).

54. J. C. Chiang, Sheng S. Li, and A. Singh, *Appl. Phys. Lett.*, **71**, 3546 (1997).
55. Jung-Chi Chiang, Sheng S. Li, M. Z. Tidrow, P. Ho, M. Tsai, and C. P. Lee, *Appl. Phys. Lett.*, **69**, 2412 (1996).
56. Y. H. Wang, Sheng S. Li, and Pin Ho, *Appl. Phys. Lett.*, **62**, 621 (1993).
57. L. C. Lenchyshyn, H. C. Liu, M. Buchanan, and Z. R. Wasilewski, *J. Appl. Phys.*, **79**, 3307 (1996).
58. J. Chu, Sheng S. Li, and A. Singh, *IEEE J. Quantum Electronics*, **35**, 312 (1999).
59. Y. H. Wang, S. S. Li, J. Chu, and Pin Ho, *Appl. Phys. Lett.*, **64**, 727 (1991).
60. B. F. Levine, A. Y. Cho, J. Walker, R. J. Malik, D. A. Kleinman, and D. L. Sivco, *Appl. Phys. Lett.*, **52**, 1481 (1988).
61. Y. H. Wang, Jung-chi Chiang, Sheng S. Li, and Pin Ho, *J. Appl. Phys.*, **76**, 2538 (1994).
62. Yaohui Zhang, D. S. Jiang, J. B. Xia, L.Q. Cui, C. Y. Song, Z. Q. Zhou, and W. K. Ge, *Appl. Phys. Lett.*, **68**, 2114 (1996).
63. Harald Schneider, Frank Fuchs, Bernhard Dischler, John D. Ralston, and Peter Koidl, *Appl. Phys. Lett.*, **58**, 2234 (1991).
64. Yuzo Hirayama, Jurgen H. Smet, Lung-Han Peng, Clifton G. Fonstad, and Erich P. Ippen, *Jpn. J. Appl. Phys.*, **33**, 890 (1994).
65. Takashi Asano, Susumu Noda, Tomoki Abe, and Akio Sasaki, *Jpn. J. Appl. Phys.*, **35**, 1285 (1996).
66. Takashi Asano, Susumu Noda, Tomoki Abe, and Akio Sasaki, *J. Appl. Phys.*, **82**, 3385 (1997).
67. J. H. Smet, L. H. Peng, Y. Hirayama, and C. G. Fonstad, *Appl. Phys. Lett.*, **64**, 986 (1994).
68. M. Z. Tidrow and K. Bacher, *Appl. Phys. Lett.*, **69**, 3396 (1996).
69. Y. H. Wang and Sheng S. Li, *Appl. Phys. Lett.*, **62**, 93 (1993).
70. C. Schönbein, H. Schneider, G. Bihlmann, K. Schwarz, and P. Koidl, *Appl. Phys. Lett.*, **68**, 973 (1996).
71. H. Schneider, C. Schönbein, M. Walther, K. Schwarz, J. Fleissner, and P. Koidl, *Appl. Phys. Lett.*, **71**, 246 (1997).

72. J. C. Chiang and S. S. Li, Electron. Lett. **34**, 1794 (1998).
73. J. C. Chiang, Sheng S. Li, and A. Singh, Appl. Phys. Lett., **71**, 3546 (1997).
74. M. Z. Tidrow, Xudong Jiang, Sheng S. Li, and K. Bacher, Appl. Phys. Lett., **74**, 1335 (1999).
75. H. Schneider, K. Kheng, M. Ramsteiner, J. D. Ralston, F. Fuchs, and P. Koidl, Appl. Phys. Lett. **60**, 1471 (1992).
76. Sheng S. Li, J. Chu, J. C. Chiang, J. H. Lee, and A. Singh, *Proc. of SPIE*, **3629**, 138 (1999).
77. J. Chu, Sheng S. Li, and A Singh, Appl. Phys. Lett. **73**, 3414 (1998).
78. S. V. Bandara, S. D. Gunapala, J. K. Liu, E. M. Luong, J. M. Mumolo, W. Hong, D. K. Sengupta, and M. J. McKelvey, Appl. Phys. Lett. **72**, 2427 (1998).
79. L. C. Lenchyshyn, H. C. Liu, M. Buchanan, and Z. R. Wasilewski, J. Appl. Phys. **79**, 3307 (1996).
80. B. F. Levine, G. Hasnain, C. G. Bethea, and Naresh Chand, Appl. Phys. Lett. **54**, 2704 (1989).
81. Y. Zhang, N. Baruch and W. I. Wang, Eletronics Letters, **29**, 213 (1993).
82. B. F. Levine, C. G. Bethea, V. O. Shen, and R. J. Malik, Appl. Phys. Lett. **57**, 383 (1990).
83. J. Y. Duboz, L. Saminadayar, and J. M. Gerard, J. Appl. Phys. **78**, 2803 (1995).
84. Wei Gao, Paul R. Berger, George J. Zydzik, Henry M. O'Bryan, Deborah L. Sivco, and Alfred Y. Cho, IEEE Transaction of Electronic Devices **44**, 2174 (1997).
85. D. H. Lee, Sheng S. Li, N. J. Sauer, and T. Y. Chang, Appl. Phys. Lett. **54**, 1863 (1989).
86. L. S. Yu and S. S. Li, Appl. Phys. Lett. **59**, 1332 (1991).
87. S. D. Gunapala and K. M. S. V. Bandara, Thin Films **21**, 113 (1995).
88. B. F. Levine, K. K. Choi, C. G. Bethea, J. Walker, and R. J. Malik, Appl. Phys. Lett. **50**, 1092 (1987).
89. S. D. Gunapala, K. M. S. V. Bandara, B. F. Levine, G. Sarusi, D. L. Sivco, and A. Y. Cho, Appl. Phys. Lett. **64**, 2288 (1994).

90. L. B. Allard, H. C. Liu, M. Buchanan, Z. R. Wasilewski, *Appl. Phys. Lett.* **70**, 2784 (1997).
91. G. U. Perera, W. Z. Shen, S. G. Matsik, H. C. Liu, M. Buchanan, and W. J. Schaff, *Appl. Phys. Lett.* **72**, 1596 (1998).
92. S. Y. Wang and C. P. Lee, *J. Appl. Phys.* **82**, 2680 (1997).
93. C. J. Chen, K. K. Choi, W. H. Chang, and D. C. Tsui, *Appl. Phys. Lett.* **73**, 1272 (1998).
94. C. J. Chen, K. K. Choi, M. Z. Tidrow, and D. C. Tsui, *Appl. Phys. Lett.* **68**, 1446 (1996).
95. M. Z. Tidrow, K. Bacher, *Appl. Phys. Lett.* **69**, 3396 (1996).
96. J. Y. Anderson, L. Lundqvist, and Z. F. Paska, *Appl. Phys. Lett.*, **58**, 2264 (1991).
97. Kyoung-Youm Kim, Byoungho Lee, and Chanho Lee, *IEEE J. of Quantum Electronics*, **35**, 1491 (1999).
98. Jun-Jie Shi and Ewa M. Goldys, *IEEE Trans. Electron Devices*, **46**, 83 (1999).
99. M. Ershov, *J. Appl. Phys.*, **86**, 7059 (1999).
100. Janet L. Pan and Clifton G. Fonstad, Jr., *IEEE J. of Quantum Electronics*, **35**, 1673 (1999).
101. C. J. Chen, K. K. Choi, W. H. Chang, and D. C. Tsui, *Appl. Phys. Lett.*, **73**, 1272 (1998).
102. L. P. Rokhinson, C. J. Chen, K. K. Choi, D. C. Tsui, G. A. Vawter, L. Yan, M. Jiang, and T. Tamir, *Appl. Phys. Lett.*, **75**, 3701 (1999).
103. Walter R. Dyer, *Electrochemical Society Proceedings* **99-22**, 425 (1999).
104. Paul L. McCarley, Mark A. Massie, Christopher R. Baxter, and Buu L. Huynh, *Proc. of SPIE* **3360**, 13 (1998).
105. M. Sundaram, T. Faska, M. Taylor, R. Williams, A. Reisinger, and S. Wang, *Electrochemical Society Proceedings* **99-22**, 429 (1999).

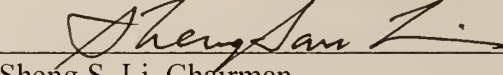
106. Sarath D. Gunapala, Sumith V. Bandara, John K. Liu, E. M. Luong, N. Stetson, Craig A. Shott, J. J. Bock, S. B. Rafol, Jason M. Mumolo, and Mark J. McKelvey, *IEEE Trans. Electron Devices*, **47**, 326 (2000).
107. Sarath D. Gunapala, Sumith V. Bandara, A. Singh, John K. Liu, Sir B. Rafol, E. M. Luong, Jason M. Mumolo, Nhan Q. Tran, David Z.-Y. Ting, J. D. Vincent, Craig A. Shott, J. Long, and Paul D. LeVan, *IEEE Trans. Electron Devices*, **47**, 963 (2000).

## BIOGRAPHICAL SKETCH

Jung Hee Lee was born in Seoul, Korea, on August 29, 1965. He received a Bachelor of Science degree in computer engineering from KwangWoon University, Seoul, Korea, in February, 1992. He completed 27 months of military service in the Ranger Corps of the Korean Army in the middle of his undergraduate study. From February 1992 to November 1993, he was with Samsung Electronics, Co., Ltd., Korea, where he worked on computer hardware design for specific purpose.

He received a Master of Science degree in electrical and computer engineering from the University of Florida in May 1996. Since August 1996 he has been pursuing his Ph.D. degree in the Department of Electrical and Computer Engineering at the University of Florida, Gainesville, Florida, working on the development of a multicolor quantum well infrared photodetector and 4 x 4 three-color focal plane array.

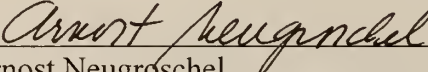
I certify that I have read this study and that in my opinion it conforms to acceptable standards of scholarly presentation and is fully adequate, in scope and quality, as a dissertation for the degree of Doctor of Philosophy.

  
\_\_\_\_\_  
Sheng S. Li, Chairman  
Professor of Electrical and Computer Engineering

I certify that I have read this study and that in my opinion it conforms to acceptable standards of scholarly presentation and is fully adequate, in scope and quality, as a dissertation for the degree of Doctor of Philosophy.

  
\_\_\_\_\_  
Gijs Bosman  
Professor of Electrical and Computer Engineering

I certify that I have read this study and that in my opinion it conforms to acceptable standards of scholarly presentation and is fully adequate, in scope and quality, as a dissertation for the degree of Doctor of Philosophy.

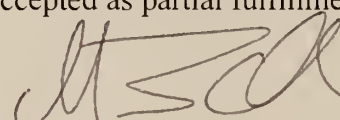
  
\_\_\_\_\_  
Arnost Neugroschel  
Professor of Electrical and Computer Engineering

I certify that I have read this study and that in my opinion it conforms to acceptable standards of scholarly presentation and is fully adequate, in scope and quality, as a dissertation for the degree of Doctor of Philosophy.

  
\_\_\_\_\_  
Timothy J. Anderson  
Professor of Chemical Engineering

This dissertation was submitted to the Graduate Faculty of the College of Engineering and to the Graduate School and was accepted as partial fulfillment of the requirements for the degree of Doctor of Philosophy.

December 2000

  
\_\_\_\_\_  
M. J. Ohanian  
Dean, College of Engineering

\_\_\_\_\_  
Winfred M. Phillips  
Dean, Graduate School